Optical properties of (Mg,Fe)O at high pressure

Lukas Schifferle, MSc BSc

Kumulative Dissertation

zur Erlangung des akademischen Grades

doctor rerum naturalium

(Dr. rer. nat.)

in der Wissenschaftsdisziplin Mineralogie

eingereicht an der

Mathematisch-Naturwissenschaftlichen Fakultät

Institut für Geowissenschaften

der Universität Potsdam

Anfertigung der Arbeit:

Sektion 3.6 Chemie und Physik der Geomaterialien

Deutsches GeoForschungsZentrum, Potsdam

Ort und Tag der Disputation: Potsdam, 15. Dezember 2023

Betreuer
Dr. Sergey S. Lobanov, Deutsches GeoForschungsZentrum & Universität Potsdam
Prof. Dr. Max Wilke, Universität Potsdam

GutachterInnen
Dr. Sergey S. Lobanov, Deutsches GeoForschungsZentrum & Universität Potsdam
Prof. Dr. Monika Koch-Müller, Deutsches GeoForschungsZentrum & Technische Universität Berlin
Prof. Dr. Carmen Sanchez-Valle, Westfälische Wilhelms-Universität Münster

Published online on the
Publication Server of the University of Potsdam:
https://doi.org/10.25932/publishup-62216
https://nbn-resolving.org/urn:nbn:de:kobv:517-opus4-622166

Meinen Eltern

Danke für alles!

Acknowledgements

I would like to express my deepest gratitude to my supervisor, Sergey S. Lobanov, for his exceptional guidance throughout the course of my doctoral studies. His mentorship, encouragement, and continuous support were invaluable to my development as a researcher.

I extend my sincere gratitude to my second supervisor, Max Wilke, for the many fruitful discussions and suggestions that have greatly benefitted this thesis and, ultimately, my academic growth.

I want to thank all the members of Section 3.6 for their continuous help and encouragement during my doctoral journey. Specifically, I want to thank Monika Koch-Müller, Sergio Speziale, Christian Schmidt, and Hans-Josef Reichmann for assisting me with analytical and experimental setups, providing guidance and suggestions, and thereby contributing greatly to the success of my studies.

I would also like to thank the technical staff at Section 3.6 and 3.5 for their help and expertise, for always being available for last-minute sample analysis, troubleshooting IT issues, or machining experimental equipment precisely to my needs.

I am deeply thankful to my fellow doctoral students and the postdocs at GFZ, namely Lea, Nicole, Jakob, Naira, Nada, Yongchao, Artem, Zihao, Melanie, and Enrico, who have accompanied me during my time in Potsdam. I want to thank them for their friendship, which has always been a limitless source of motivation.

Throughout all these years, from the mountains to the lowlands and back, I owe my deepest gratitude to my girlfriend, Willemijn. Thank you so much!

Liebe Mami, liebe Michi, danke, dass Ihr immer für mich da wart und mich jederzeit unterstützt habt auch wenn die Zeiten und Umstände mitunter kaum schwieriger hätten sein können. Für unseren Zusammenhalt bin ich unendlich dankbar! Lieber Papi, auch wenn diese Zeilen für dich zu spät kommen und du den Abschluss nicht mehr miterleben konntest, möchte ich dir trotzdem nochmal aus tiefstem Herzen danken! Danke für alles, was du Zeit meines Lebens für mich getan hast. Danke, dass ich immer auf deinen Rat zurückgreifen konnte. Einfach danke dafür, dass du der beste Vater warst, den ich mir vorstellen konnte!

Ultimately, I would like to acknowledge the financial support provided by the Helmholtz Young Investigators Group CLEAR (VH-NG-1325) that made this research possible.

Abstract

Large parts of the Earth's interior are inaccessible to direct observation, yet global geodynamic processes are governed by the physical material properties under extreme pressure and temperature conditions. It is therefore essential to investigate the deep Earth's physical properties through in-situ laboratory experiments. With this goal in mind, the optical properties of mantle minerals at high pressure offer a unique way to determine a variety of physical properties, in a straight-forward, reproducible, and time-effective manner, thus providing valuable insights into the physical processes of the deep Earth. This thesis focusses on the system Mg-Fe-O, specifically on the optical properties of periclase (MgO) and its iron-bearing variant ferropericlase ((Mg,Fe)O), forming a major planetary building block. The primary objective is to establish links between physical material properties and optical properties. In particular the spin transition in ferropericlase, the second-most abundant phase of the lower mantle, is known to change the physical material properties. Although the spin transition region likely extends down to the core-mantle boundary, the effects of the mixed-spin state, where both high- and low-spin state are present, remains poorly constrained.

In the studies presented herein, we show how optical properties are linked to physical properties such as electrical conductivity, radiative thermal conductivity and viscosity. We also show how the optical properties reveal changes in the chemical bonding. Furthermore, we unveil how the chemical bonding, the optical and other physical properties are affected by the iron spin transition. We find opposing trends in the pressure dependence of the refractive index of MgO and (Mg,Fe)O. From 1 atm to ~140 GPa, the refractive index of MgO decreases by ~2.4% from 1.737 to 1.696 (±0.017). In contrast, the refractive index of $(Mg_{0.87}Fe_{0.13})O$ (Fp13) and $(Mg_{0.76}Fe_{0.24})O$ (Fp24) ferropericlase increases with pressure, likely because Fe-Fe interactions between adjacent iron sites hinder a strong decrease of polarizability, as it is observed with increasing density in the case of pure MgO. An analysis of the index dispersion in MgO (decreasing by ~23% from 1 atm to ~103 GPa) reflects a widening of the band gap from ~7.4 eV at 1 atm to ~8.5 (±0.6) eV at ~103 GPa. The index dispersion (between 550 and 870 nm) of Fp13 reveals a decrease by a factor of ~3 over the spin transition range (~44–100 GPa). We show that the electrical band gap of ferropericlase significantly widens up to ~4.7 eV in the mixed spin region, equivalent to an increase by a factor of ~1.7. We propose that this is due to a lower electron mobility between adjacent Fe^{2+} sites of opposite spin, explaining the previously observed low electrical conductivity in the mixed spin region. From the study of absorbance spectra in Fp13, we show an increasing covalency of the Fe-O bond with pressure for high-spin ferropericlase, whereas in the low-spin state a trend to a more ionic nature of the Fe-O bond is observed, indicating a bond weakening effect of the spin transition. We found that the spin transition is ultimately caused by both an increase of the ligand field-splitting energy and a decreasing spin-pairing energy of high-spin Fe^{2+}.

Zusammenfassung

Geodynamische Prozesse werden von den physikalischen Materialeigenschaften unter den extremen Druck- und Temperaturbedingungen des Erdinneren gesteuert, gerade diese Areale sind aber faktisch nicht für direkte Beobachtungen zugänglich. Umso wichtiger ist es, die physikalischen Eigenschaften unter Bedingungen des Erdinneren zu untersuchen. Mit diesem Ziel vor Augen erlaubt das Studium der optischen Eigenschaften von Mineralen des Erdmantels, eine große Bandbreite an physikalischen Materialeigenschaften, in einer einfachen, reproduzierbaren und effizienten Art und Weise zu bestimmen. Dadurch bieten sich wichtige Einblicke in die physikalischen Prozessen des Erdinneren. Die vorliegende Arbeit konzentriert sich auf das System Mg-Fe-O, im Speziellen auf Periklas (MgO) und seine Eisen-haltige Variante Ferroperiklas ((Mg,Fe)O), ein wichtiger Baustein planetarer Körper. Das Hauptziel der Arbeit besteht darin Verbindungen zwischen optischen Eigenschaften und physikalischen Materialeigenschaften zu finden. Gerade der Spin-Übergang in Ferroperiklas, der zweithäufigsten Phase des unteren Erdmantels, ist dabei von Bedeutung, da damit Veränderungen in den physikalischen Materialeigenschaften einhergehen. Obwohl sich der Spinübergangsbereich vermutlich bis zur Kern-Mantel-Grenze erstreckt, sind die Auswirkungen des gemischten Spin-Zustandes, bei dem sowohl Hoch- als auch Tief-Spin präsent sind, nur unzureichend untersucht.

Die hier vorgestellten Studien zeigen, wie optische Eigenschaften mit anderen wichtigen physikalischen Eigenschaften wie elektrischer und thermischer Leitfähigkeit, Viskosität oder auch mit der chemischen Bindung verbunden sind. Daraus lässt sich auch ableiten wie der Spin-Übergang in Ferroperiklas diese Eigenschaften beeinflusst. Von Raumbedingungen bis zu ~140 GPa sinkt der Brechungsindex von MgO um ~2.4 % von 1.737 auf 1.696 (±0.017). Im Gegensatz dazu steigt der Brechungsindex von $(Mg_{0.87}Fe_{0.13})O$ (Fp13) und $(Mg_{0.76}Fe_{0.24})O$ (Fp24) Ferroperiklas mit dem Druck an. Dies ist auf Fe-Fe Wechselwirkungen zwischen benachbarten Eisenpositionen zurückzuführen, die eine starke Verringerung der Polarisierbarkeit, wie im Falle von reinem MgO mit zunehmender Dichte, behindern. Eine Analyse der Dispersion des Brechungsindexes von MgO (Abnahme um ~23 % von 1 Atm zu ~103 GPa) offenbart eine Verbreiterung der Bandlücke von ~7.4 eV bei 1 Atm zu ~8.5 (±0.6) eV bei ~103 GPa. Die Messung der Dispersion (zwischen 550 und 870 nm) in Fp13 zeigt eine starke Abnahme über den Bereich des Spin-Überganges (~44–100 GPa) bis zu einem Faktor von ~3. Die Bandlücke nimmt in der Region des gemischten Spin-Zustandes signifikant auf bis zu ~4.7 eV zu (entspricht einer Zunahme um den Faktor ~1.7). Dies deutet auf eine Verringerung der Elektronen-Mobilität zwischen benachbarten Fe^{2+}-Positionen mit unterschiedlichem Spin-Zustand hin, was die bereits in früheren Arbeiten beobachtete Abnahme der elektrischen Leitfähigkeit im Bereich des gemischten Spin-Zustandes erklärt. Absorptionsspektren an Fp13 zeigen eine Druck-bedingte Zunahme der Kovalenz der Fe-O Bindung für Ferroperiklas im Hoch-Spin Zustand, wohingegen Tief-Spin Ferroperiklas einen Trend zu einer mehr ionischen Fe-O Bindung aufweist, was auf einen Bindungs-schwächenden Effekt des Spin-Wechsels hinweist. Der Übergang von Hoch- zu Tiefspin ist letztlich auf eine Zunahme der Ligandenfeldaufspaltungsenergie sowie eine abnehmende Spinpaarungsenergie von Hoch-Spin Fe^{2+} zurückzuführen.

Allgemeinverständliche Zusammenfassung

Große Teile des Erdinneren sind für direkte Untersuchungen nicht zugänglich; dabei spielen aber die extremen Druck- und Temperaturbedingungen, wie sie in den Tiefen der Erde herrschen eine wichtige Rolle für die physikalischen Materialeigenschaften, die Geschichte und Entwicklung unseres Planeten beeinflussen. Durch das Studium der optischen Eigenschaften von Mineralen lassen sich in einer einfachen und effizienten Art und Weise physikalische Prozesse des Erdinneren nachvollziehen. Die vorliegende Arbeit konzentriert sich dabei auf das System Magnesium-Eisen-Sauerstoff (Mg-Fe-O), das von grundlegender Bedeutung für die Zusammensetzung des Erdinneren ist. Ziel ist es, Verbindungen zwischen optischen und physikalischen Materialeigenschaften zu finden. Die Untersuchung konzentriert sich dabei vor allem auf Periklas (MgO) sowie dessen eisenhaltige Variante Ferroperiklas ((Mg,Fe)O), die einen wichtigen Baustein für den Aufbau von Planeten bildet. Bei Ferroperiklas, der zweithäufigsten Phase des unteren Erdmantels, führt der extreme Druck im Inneren der Erde zu einer Umordnung der Elektronenhülle und einem Übergang vom Hoch-Spin Zustand zum Tief-Spin Zustand, was dessen physikalische Eigenschaften verändert. Obwohl sich dieser Prozess über große Teile des unteren Erdmantels, vermutlich auch bis zur Kern-Mantel-Grenze, erstreckt, ist der Übergangsbereich zwischen Hoch-Spin und Tief-Spin nur unzureichend untersucht. Mittels Optischer Spektroskopie lassen sich jedoch Eigenschaften thermische und elektrische Leitfähigkeit sowie die chemische Bindung untersuchen, und dabei auch die Einflüsse des Spin-Überganges feststellen. Der Brechungsindex von MgO nimmt von Raumdruck bis zu ~140 GPa um ~2.4 % ab. Im Gegensatz dazu zeigt (Mg,Fe)O eine Zunahme des Brechungsindexes mit dem Druck. Dies dürfte auf die Wechselwirkungen zwischen benachbarten Eisen-Positionen zurückzuführen sein. Während bei MgO die Druckzunahme zu einer starken Verringerung der Polarisierbarkeit führt, behindern dies die Eisen-Eisen Wechselwirkungen in (Mg,Fe)O. Die Dispersion von MgO, also die Wellenlängenabhängigkeit des Brechungsindexes, zeigt außerdem eine Abnahme der Dispersion um ~23% mit dem Druck an (von Raumdruck zu ~103 GPa), was auf eine Verbreiterung der Bandlücke hinweist. Bei Ferroperiklas lässt sich eine starke Abnahme der Dispersion (ca. um den Faktor 3) und eine deutliche Zunahme der Bandlücke (um den Faktor ~1.7) feststellen. Wir vermuten, dass dies durch eine Verringerung der Mobilität von Elektronen zwischen benachbarten Eisenatomen verursacht wird, wenn diese unterschiedliche Elektronenstrukturen aufweisen. Dies passt auch zur bereits früher beobachteten Abnahme der elektrischen Leitfähigkeit im Spin-Übergangs-Bereich. Wir haben auch untersucht, wie Licht in Ferroperiklas absorbiert wird und konnten daraus Trends im Bindungscharakter zwischen Eisen und Sauerstoff feststellen. Im Hoch-Spin Zustand, wie er vor der Umordnung herrscht, verstärkt Druckzunahme die Kovalenz der Eisen-Sauerstoffbindung. Im Tief-Spin Zustand ist jedoch mit zunehmendem Druck ein Trend zu einer eher ionischen Bindung zu verzeichnen, was auf einen bindungsschwächenden Effekt des Spin-Überganges hinweist. Außerdem konnte festgestellt werden, dass der Spin-Übergang sowohl auf Zunahme der Unterschiede zwischen den Energieniveaus der äußeren Elektronenhülle als auch auf eine Abnahme der Paarungsenergie der Elektronen zurückzuführen ist.

Table of contents

Chapter 1 Introduction

In the Earth's interior, minerals are exposed to extreme pressure (*P*) and temperature (*T*) conditions. In this high *P* and *T* environment, the physical properties of geomaterials govern large-scale geodynamic processes such as, subduction of oceanic slabs, rise of mantle plumes, and location and distribution of earthquakes. However, the physical material properties, such as bulk modulus, viscosity, electrical and thermal conductivity, are sensitive to changes in temperature and pressure (e.g., Higo et al., 2006; Justo et al., 2015; Hsieh et al., 2018). Our direct access to the Earth's interior is limited, as the deepest wells reach just shallow crustal levels (Clarke et al., 1986) and even superdeep diamonds only contain inclusions from as far down as ~1,000 km (Alvaro et al., 2022). This still leaves thousands of kilometres of inaccessible territory in the Earth's interior. A broad variety of information on Earth's internal structure and composition can be obtained from mantle xenoliths, diamond inclusions, extra-terrestrial materials, geophysical surveys and numerical modelling. Nevertheless, a full comprehension of global scale geodynamics requires in-situ observations of deep Earth materials to assess the effects of extreme *P* and *T* conditions on the physical material properties.

Present-day Earth is divided into distinct layers, each with a specific mineralogical composition (**Figure 1-1**). This is a result of *P* and *T* distribution, phase-stability fields and chemical exchange processes. The Earth's mantle itself is subdivided in the upper mantle (down to 410 km) and the lower mantle (660–2,900 km), which are separated by the transition zone (410–660 km). The upper mantle is mainly composed of olivine, pyroxene and garnet. The phase transition of olivine (α-$(Mg,Fe)_2SiO_4$) to wadsleyite (β-$(Mg,Fe)_2SiO_4$) marks the beginning of the mantle transition zone (also indicated by the 410 km discontinuity in seismic signals). The upper part of the transition zone is characterized by the assemblage of mostly wadsleyite and majoritic garnet, while its lower part is defined by the transition from β- to γ-$(Mg,Fe)_2SiO_4$ (ringwoodite). The crossover to the lower mantle is then characterized by the decomposition of ringwoodite to magnesium silicate perovskite-structured bridgmanite ($(Mg,Fe,Al)(Si,Al)O_3$) and *B*1-structured (ferro)periclase ((Mg,Fe)O). Together with calcium silicate perovskite ($CaSiO_3$), these three phases are the major constituents of the lower mantle (**Figure 1-1**).

The chemical composition of the individual phases of the Earth's interior (**Figure 1-1**) governs its thermodynamic and physical properties (e.g., stability, structure, density, compressibility, viscosity, thermal and electrical conductivity), and is therefore of primary geological importance (Higo et al., 2006; Yoshino et al., 2011; Mrosko et al., 2015; Otsuka and Karato, 2015; Cerantola et al., 2017; Deng and Lee, 2017; Hsieh et al., 2018; Nakatsuka et al., 2021). Iron is the fourth most abundant element of the Earth's mantle (~6 wt.-%; McDonough and Sun, 1995). The effect of iron on the physical properties is immense. For instance, the electrical conductivity of (Mg,Fe)O increases by one order of magnitude up the ~50 to 60 GPa range (X_{Fe} = 0.25 (Lin et al., 2007b) resp. 0.19 (Ohta et al., 2007)), whereas the iron-free MgO is considered a wide-bandgap insulator (e.g., Zhu et al., 2013).

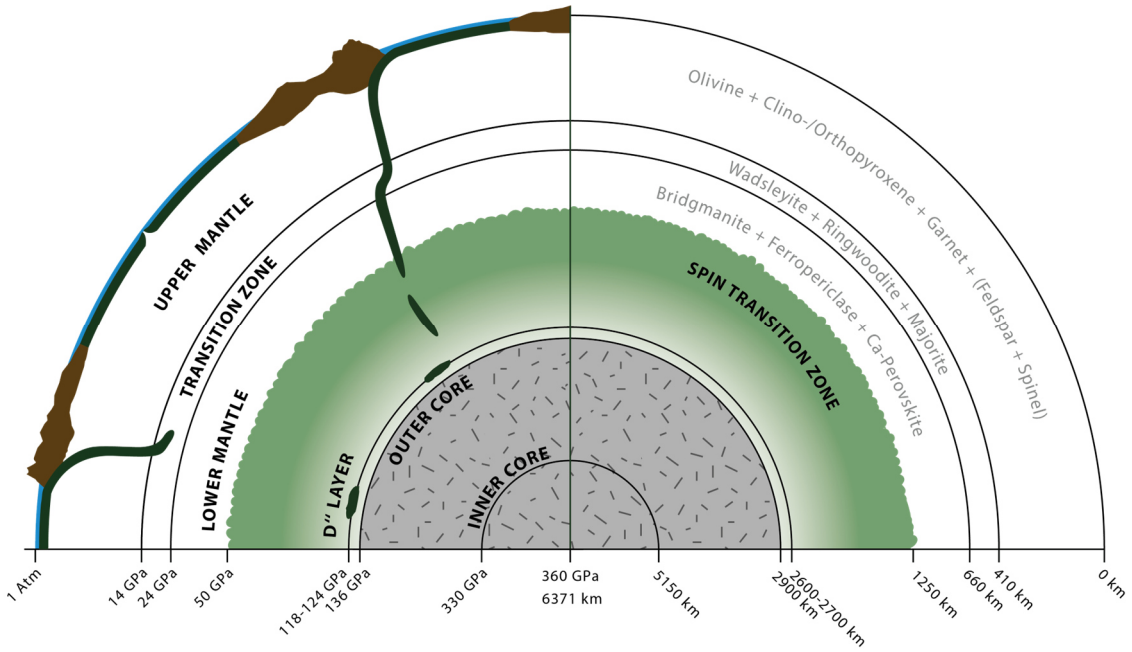

Figure 1-1 Structure, pressure, and phase-composition of the Earth's interior. Green area shows the approximate depth of the spin transition zone where iron changes its spin state from a high-spin to a low-spin configuration (Lin et al., 2007a; Holmström and Stixrude, 2015).

With the electronic configuration [Ar] $3d^6\ 4s^2$, iron is per definition considered a transition metal element due to the presence of incompletely filled *d* shells. Typical oxidation states incorporated by mantle minerals are either Fe^{2+} ([Ar] $3d^6$) or Fe^{3+} ([Ar] $3d^5$). Analysis of natural diamond inclusions and laboratory experiments suggest only minor presence of Fe^{3+} in ferropericlase, but a high Fe^{3+} content is possible in bridgmanite (McCammon et al., 1997; McCammon et al., 1998). Fe^{2+} possesses six 3*d* electrons, which populate the respective electron orbitals. For a field-free Fe^{2+} ion (i.e., not incorporated in any structure), all five 3*d* orbitals are degenerate. However, if a Fe^{2+} ion is positioned on an octahedral site like in the rock-salt structure of ferropericlase, the 3*d* orbitals are split into three low energy t_{2g} and two high-energy e_g orbital energy levels (**Figure 1-2**). The cause of the splitting of the *d*-level are the electron-electron repulsion forces between the *d*-orbitals of Fe and the *p*-orbitals of O. The electrons occupying the e_g-orbitals are experiencing stronger repulsion due to their head-on overlap with the *p*-orbitals. The orbital population follows Hund's first rule: first the t_{2g} orbitals are filled with single electrons of parallel spin, then the e_g-orbitals. The double occupation on the t_{2g}-level happens last because the sharing of an orbital requires a certain energy (termed spin-pairing energy). Under ambient conditions, Fe^{2+} is found in the high-spin (HS) state (**Figure 1-2**, **A**). More than 60 years ago, Fyfe (1960) proposed that high pressure in the Earth's mantle might lead to a spin pairing of iron's *d* electrons, causing a transition from the high-spin state to the low-spin (LS) state, where all electrons are paired on the t_{2g} level (**Figure 1-2**, **B**). Indeed, more than 40 years later an experiment of Badro et al. (2003) confirmed such a spin transition for ferropericlase in the 40 to 70 GPa range. Since Fyfe's hypothesis, many studies have analysed the effects of a spin transition on the transport properties of ferropericlase (e.g., Hazen, 1976; Goto et al., 1980; Badro et al., 2003; Goncharov et al., 2006; Keppler et al., 2007; Lin et al., 2007b; Goncharov et al., 2009; Wentzcovitch et al., 2009; Lin et al., 2010; Ammann et al., 2011; Lyubutin et al., 2013; Goncharov et al., 2015; Vilella et al., 2015; Solomatova et al., 2016; Deng and

Lee, 2017; Ohta et al., 2017; Reali et al., 2019; Song et al., 2019). Recently, the spin transition in ferropericlase was also discovered in geophysical datasets (Shephard et al., 2021).

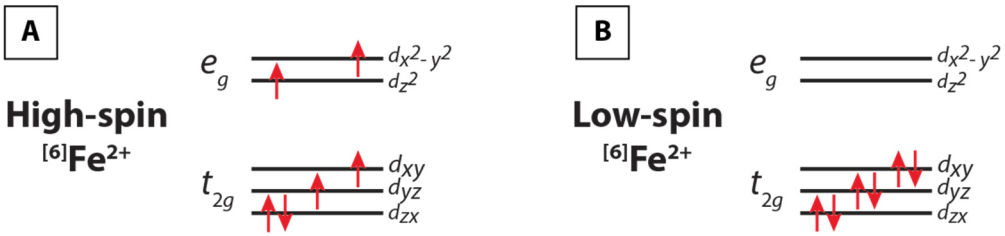

Figure 1-2 Electronic configuration of high-spin (A) and low-spin (B) Fe^{2+} in an octahedral configuration (modified after Burns, 1993).

The spin transition in ferropericlase occurs at pressures between 40 to 80 GPa and features a pronounced mixed-spin (MS) zone, where both HS and LS state are present (Badro et al., 2003; Lin et al., 2005; Speziale et al., 2005; Goncharov et al., 2006; Keppler et al., 2007; Lin and Tsuchiya, 2008; Glazyrin et al., 2016; Hamada et al., 2021). The spin transition is dependent on the iron content, where higher amounts of Fe stabilize the HS state (Lin et al., 2006; Kantor et al., 2009; Glazyrin et al., 2016). The spin transition has direct geophysical consequences, as the electron pairing on lower-level orbitals reduces the ionic radius of Fe^{2+}, consequently increasing the density of ferropericlase (e.g., Tsuchiya et al., 2006). Additionally, the spin transition causes changes in the absorption spectra, with increased absorbance in the mid- to near-infrared, hence reducing the radiative thermal conductivity for low-spin ferropericlase (Goncharov et al., 2006; Keppler et al., 2007; Goncharov et al., 2009). Due to the altered electronic configuration, the electrical conductivity of ferropericlase is significantly reduced across the spin transition by a factor of 3 to 4 (Lin et al., 2007b; Ohta et al., 2007). Furthermore, the iron partitioning coefficient between ferropericlase and the surrounding mantle minerals is affected by the spin transition (Badro et al., 2003; Saha et al., 2013; Muir and Brodholt, 2016; Xu et al., 2017). In addition, a softening of the elastic constants (primarily C_{11}, C_{12}) (Crowhurst et al., 2008; Marquardt et al., 2009; Wu et al., 2013; Yang et al., 2015) and a reduction of the viscosity was found for the spin transition range (Wentzcovitch et al., 2009; Saha et al., 2013; Marquardt et al., 2018).

In contrast to the well-documented spin transition in ferropericlase, the occurrence and mechanism of the spin transition(s) (for Fe^{2+} and Fe^{3+}) in bridgmanite is controversial (McCammon et al., 2008; Hsu et al., 2011b; Ballaran et al., 2012; Lin et al., 2013; Prescher et al., 2014; Kupenko et al., 2015; Okuda et al., 2020b). In part, this might be because of the complex crystallographic setting and the presence of both Fe^{2+} and Fe^{3+} (e.g., McCammon et al., 2008; Hsu et al., 2011a; Lobanov et al., 2017b). Iron in bridgmanite is distributed over two sites, the large pseudo-dodecahedral *A*-site (hosting Fe^{2+} and Fe^{3+}) and the small octahedral *B*-site (hosting Fe^{3+}, but limited by Al^{3+} content) (McCammon, 1997; Lauterbach et al., 2000; Catalli et al., 2010; Lin et al., 2013; Potapkin et al., 2013; Lobanov et al., 2017b). Experimental and theoretical evidence indicates a HS-to-LS transition of Fe^{3+} occurring between ~15 and 50 GPa on the *B*-site, whilst iron on the *A*-site always stays in HS state (Bengtson et al., 2008; Lin et al., 2013; Dorfman et al., 2015; Mao et al., 2015;

Lobanov et al., 2017b; Okuda et al., 2020b). Possible effects of the Fe^{3+} spin transition in bridgmanite are bulk modulus softening (Catalli et al., 2011; Hsu et al., 2011a; Okuda et al., 2020b), a (small) reduction of the unit cell volume (Catalli et al., 2010; Mao et al., 2015; Okuda et al., 2020b) and a change in bulk sound velocity. The latter potentially causes positive anomalies before the spin transition and negative anomalies below (Catalli et al., 2011). However, the induced changes to density and bulk sound velocity by the Fe^{3+} spin transition are relatively small (Lin et al., 2016; Liu et al., 2018; Zhu et al., 2020). Combined with the low amount of Fe^{3+} on the *B*-site (*A*-site is preferred; e.g., Lin et al., 2016; Mohn and Trønnes, 2016) and the gradual transition to the LS state, it is unlikely that the spin transition in bridgmanite creates observable seismic anomalies in the lower mantle (Lin et al., 2016; Liu et al., 2018; Zhu et al., 2020).

To recreate the deep Earth's *P*-*T*-conditions, specialized high-pressure devices and procedures such as piston-cylinder-apparatus, multi-anvil-press, diamond anvil cell (DAC) and shock wave experiments have been developed. These techniques are applicable to an almost unlimited variability of materials and are able to create *P*-*T*-conditions far beyond from what is found on Earth (e.g., Benedetti and Loubeyre, 2004; Dubrovinsky et al., 2015), enabling both the study of the deep Earth as well as other planetary bodies with even more extreme *P*-*T*-conditions. By directly simulating deep Earth's *P* and *T*, state-of-the-art high-pressure techniques allow to study e.g., phase transitions, chemical reactions, melting processes, deep Earth rheology and nearly all physical properties of deep Earth minerals.

Studying the effects of pressure (e.g., Williams and Knittle, 1990; Badro et al., 2003; Lin et al., 2007b; Goncharov et al., 2009; Goncharov et al., 2015; Muir and Brodholt, 2015; Cerantola et al., 2017; Buchen et al., 2018; Pamato et al., 2019; Liu et al., 2022) can be extremely challenging, requiring sophisticated experimental setups and time-consuming measurements, which are often associated with high uncertainties. Here, the combination of optical spectroscopy with DAC experiments provides the opportunity to gain insights or even quantify a variety of physical properties, in a straight-forward, reproducible, and time-effective manner. The determination of optical properties from DAC experiments is a well-established technique, first introduced in the 1950s (Weir et al., 1959). Its applicability to high pressure research has been refined over the decades and is applied to a broad variety of fields such as (but not limited to) geosciences, materials sciences, chemistry, etc. The DAC is a high-pressure apparatus, in which a sample is squeezed between the tips of two diamonds (**Figure 1-3**). The diamonds are mounted on *x*-*y* adjustable seats (typically tungsten carbide or cubic boron nitride) to allow for a perfect alignment of the two opposing culet faces. Force resp. pressure is generated by tightening the pressure-driving screws, which forces the diamonds towards each other and creates high-pressure conditions at their tips. The seats act as stiff backing plates with an aperture that allows to access the sample with a variety of electromagnetic probes. To prevent the lateral extrusion of the sample, it is contained by a gasket (usually metallic; e.g., rhenium, tungsten, or stainless steel) and can optionally be surrounded by a relatively soft pressure-transmitting medium (salts, gasses, or oil mixtures). The pressure medium helps to reduce deviatoric stresses across the sample chamber. The possibility to achieve pressures in the megabar range, its high temperature stability and accessibility to a broad variety of measurement techniques make the DAC the optimal device to study samples at conditions similar to planetary interiors.

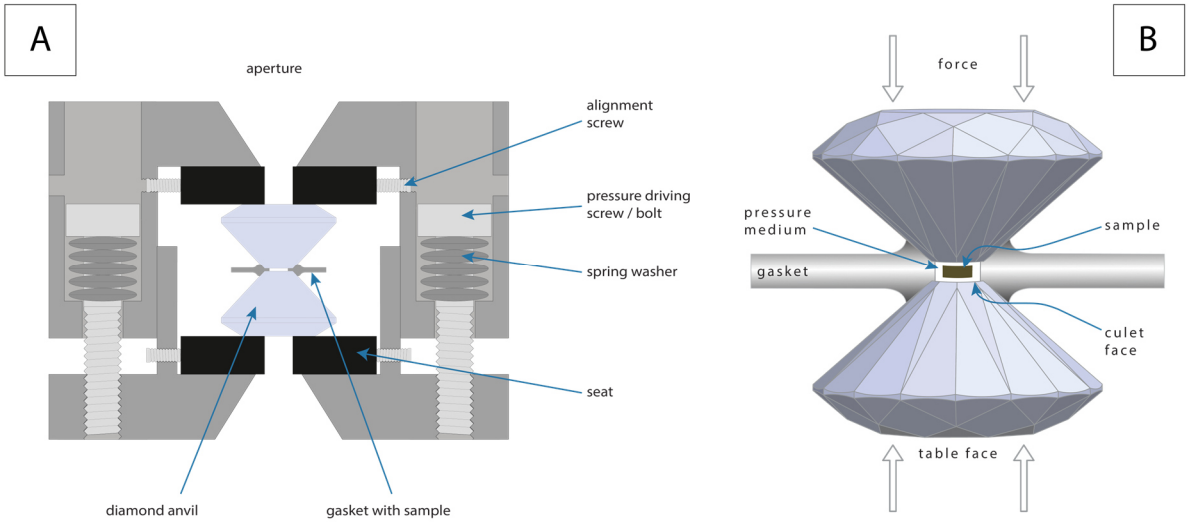

Figure 1-3 (A) A symmetrical diamond anvil cell generates high pressure by applying force onto the gasket resp. sample chamber via tightening of the screws. The diamond anvil cell houses two diamond anvils which are mounted with their table faces to a seat. Alignment screws are used to adjust the positions of the diamond culet faces with respect to each other. (B) The sample itself is located between the flattened tips (culets) of the diamonds, contained by a typically metallic gasket. The sample chamber can either be filled by a sample and a pressure transmitting medium (as depicted), or with just the sample.

The diamond anvils provide a direct line of sight to the sample in its high-pressure container. Because diamonds are essentially transparent to light, from UV to the far infrared (e.g., Mildren, 2013), they allow for measurements of a broad spectral range. In the studies presented in this thesis we performed both reflectance and transmission measurements, where reflectance is measured as the amount of light being reflected from the diamond-sample interface (in experiments without pressure-transmitting medium), whereas transmission measurements are conducted through the entire diamond anvil cell assembly (details on the exact measurement procedures are explained in the respective chapters of this thesis). Transmission measurements allow to obtain wavelength-resolved spectra and quantify the absorption coefficient (α) of the sample (i.e., a property that describes light attenuation per sample unit length). Reflectance measurements can be related to the refractive index of the sample (n). The refractive index is a fundamental, material-specific property that reflects how electromagnetic waves propagating through the material interact with the electric charges of the material. The refractive index and its wavelength-dependence (dispersion) are of major importance, because they provide information on the electronic band structure, which can be sensitive to changes in the (crystal) structure and chemical bonding (Wemple and DiDomenico, 1971; Lobanov et al., 2022). Because the refractive index is a main contributor to the radiative conductivity (approx. formula: $k_{rad} \propto \frac{n^2 \cdot T^3}{\alpha}$, where T is temperature; Clark, 1957; Lobanov et al., 2020), it is essential for our understanding of heat distribution in the deep Earth (e.g., Goncharov et al., 2006; Keppler et al., 2007; Lobanov et al., 2016). For high-pressure experiments the refractive index is also of practical use, as it allows in-situ thickness measurements. In their absence, the unknown sample thickness is considered one of the biggest sources of error in thermal and electrical conductivity DAC experiments (Lobanov and Geballe, 2022). For example, possible errors in sample thickness might be responsible for the large discrepancy in thermal conductivity estimations for the Earth's mantle and core (Keppler et al., 2008; Goncharov et al., 2015; Konôpková et al.,

2016; Ohta et al., 2016; Lobanov et al., 2017a; Geballe et al., 2020; Lobanov et al., 2020; Okuda et al., 2020a; Lobanov and Geballe, 2022; Murakami et al., 2022).

In addition to the refractive index it is also essential to quantify how light is being transmitted and (eventually) absorbed when passing through a material. The wavelength-dependent absorbance of light is an important optical property and defines how the colour of a material is formed. As an electromagnetic wave, light in the near-infrared (NIR), visible (VIS) and ultra-violet (UV) range interacts with the material. Specifically for the VIS range, electron excitations are triggered in the atom's outermost electron shells. The energies of these transitions, which are expressed in the position of absorption bands, are element-, oxidation state- and structure-dependent. Therefore, the study of absorbance spectra reveals information about the chemical composition of a sample and allows to characterise the electronic structure of individual elements on specific sites in the crystal structure (Burns, 1993).

Amongst the minerals of the deep Earth, the chemical system Mg-Fe-O is of prime importance, as these three elements are present in nearly all minerals of the lower mantle. Composed solely from elements of this simple system, periclase (MgO), resp. its iron-bearing variant ferropericlase ((Mg,Fe)O) forms one of the most important building blocks of planetary bodies. On the one hand, periclase, due to its high-temperature stability (Hynes, 2016) and chemical inertness, is of high demand in the refractory industry (Wilson, 1981; Shand, 2010) and is an indispensable component in planetary modelling (McWilliams et al., 2012; Musella et al., 2019). With its *B*1 rock-salt structure, it is stable up to at least 400 GPa (for $T < 3000$ K) (Belonoshko et al., 2010; McWilliams et al., 2012; Soubiran and Militzer, 2020; Coppari et al., 2021). On the other hand, ferropericlase, is the second-most abundant mineral of the lower mantle (e.g., Irifune and Tsuchiya, 2015; Marquardt and Miyagi, 2015), a major contributor to mantle rheology (Yamazaki and Karato, 2001; Yamazaki et al., 2009; Marquardt and Miyagi, 2015) and an important heat sink that blocks radiated heat from the core throughout the mantle (Lobanov et al., 2021). In particular, the changes to the material properties induced by the spin transition are of high geophysical relevance (Badro et al., 2003; Goncharov et al., 2006; Tsuchiya et al., 2006; Keppler et al., 2007; Lin et al., 2007b; Crowhurst et al., 2008; Goncharov et al., 2009; Marquardt et al., 2009; Wentzcovitch et al., 2009; Saha et al., 2013; Wu et al., 2013; Yang et al., 2015; Muir and Brodholt, 2016; Xu et al., 2017; Marquardt et al., 2018).

Because of the geological importance of the system Mg-Fe-O to the deep Earth, we were especially interested how the optical properties of (Mg,Fe)O change under high-pressure conditions. Thus, we chose to focus our studies on periclase and ferropericlase. By using several optical techniques in combination with the DAC method, we investigated how the refractive index and absorption coefficient of (Mg,Fe)O change as a function of pressure and across the spin transition. The goal of the following studies was to establish links between the optical properties and physical material properties.

Chapter 2

High-pressure evolution of the refractive index of MgO up to 140 GPa

Published in:

Journal of Applied Physics, 132(12), 125903, 2022.

High-pressure evolution of the refractive index of MgO up to 140 GPa

Lukas Schifferle[1,2], Sergio Speziale[1]; Sergey S. Lobanov[1,2]

[1] *GFZ German Research Center for Geosciences, Telegrafenberg, 14473 Potsdam, Germany*

[2] *Institute of Geosciences, University of Potsdam, Karl-Liebknecht-Straße 24-25, 14476 Potsdam, Germany*

(Received 29th June 2022; revised manuscript received 23rd August 2022; accepted 31st August 2022; published 28th September 2022)

Refractive index provides fundamental insights into the electronic structure of materials. At high pressure, however, the determination of refractive index and its wavelength dispersion is challenging, which limits our understanding of how physical properties of even simple materials, such as MgO, evolve with pressure. Here we report on the measurement of room-temperature refractive index of MgO up to ~140 GPa. The refractive index of MgO at 600 nm decreases by ~2.4% from ~1.737 at 1 atm to ~1.696 (±0.017) at ~140 GPa. Despite the index at 600 nm is essentially pressure-independent, the absolute wavelength-dispersion of the refractive index at 550-870 nm decreases by ~28% from ~0.015 at 1 atm to ~0.011 ($\pm 8.04 \times 10^{-4}$) at ~103 GPa. Single-effective oscillator analysis of our refractive index data suggests that the band gap of MgO increases by ~1.1 eV from 7.4 eV at 1 atm to ~8.5 (±0.6) eV at ~103 GPa.

Author contributions: Lobanov developed the conceptualization of the study. High-pressure experiments were performed by **Schifferle** and Lobanov. The authors contributed to the data analysis and interpretation in the following order: **Schifferle**, Lobanov, Speziale. The original draft was written by **Schifferle**. All authors contributed to the reviewing and editing of the manuscript.

DOI: 10.1063/5.0106626

2.1 Introduction

Refractive index is a fundamental material property that reflects the response of electric charges in the material to the oscillating electromagnetic field. The pressure dependence of the refractive index (n) and its wavelength-dispersion in the near-infrared (near-IR), visible (VIS), and ultraviolet (UV) regions are of great interest as they give insights into the effects of pressure on the electronic band structure of materials upon compression [1]. For example, refractive index and its dispersion allow correlations with structural properties such as coordination number and chemical bond character [2; 3]. The change of refractive index with pressure is also of direct importance to geophysics because radiative thermal conductivity, which is believed to increase with depth in the Earth, is proportional to n^2 [4; 5]. Furthermore, refractive index of materials at high pressure allows the determination of diamond-diamond separation in diamond anvil cell (DAC) experiments, which in turn is a key parameter needed to determine thermal/electrical conductivities of materials in DAC experiments. The existent large discrepancy in the thermal conductivities of the Earth's mantle and core [6–15] , based on DAC experiments, may be rooted in the inadequate assessment of samples' thickness at high pressure. Finally, the density dependence of the refractive index is also needed in shockwave experiments where n of the interferometer window is essential for velocity corrections, needed to determine the properties of the sample [16].

MgO, a simple oxide crystallizing in the rock salt structure (B1), has attracted a high number of experimental and theoretical studies because it is a prototypical ionic oxide of technological importance [17] and relevance as a planetary building block [18; 19]. The stability of MgO at high temperature (T) (melting point 3098 K[20]) and its chemical inertness make it suitable for industrial applications as a refractory material [17; 21]. At T < 3000 K, B1 MgO is also stable to very high pressures (P) (up to > ~400 GPa [18; 22–24]). The abundance of Mg and O in planetary-forming environments and the P-T stability of MgO render it a material of special interest to geo- and planetary scientists. In particular, the physical properties of MgO at high P-T conditions are needed to model planetary dynamics [18; 19]. MgO is also frequently used in high-pressure experiments [25–27] as a chemical/thermal insulator and as a pressure calibrant [28], due to its physical stability and a well-established equation of state (EOS) [22; 29; 30]. Although the physical properties of MgO at high pressure have been the subject of many studies, its optical properties, which are of both practical and fundamental importance, remain poorly constrained.

Information on the refractive index of MgO at high pressure (P > 30 GPa) is limited to (a) a single density-functional theory (DFT) computation [29] of the high-frequency dielectric constant (ϵ_∞), where $n = \sqrt{\epsilon_\infty}$ and (b) shockwave experiments which inferred the index of MgO in the near-IR range [31]. Both studies are broadly consistent with each other and show that the electronic contribution to the index of MgO decreases upon compression to 100 GPa by ~ 2-4%. Direct measurements of the refractive index of MgO at constant temperature [32–34] are limited to pressures below 23 GPa [34]. The wavelength-dispersion of the refractive index of MgO at high pressure is also unknown. Here we report on the room-temperature refractive index of MgO in the VIS and near-IR to ~140 GPa and its wavelength-dispersion to ~103 GPa. These data provide the first experimental constrain on the evolution of the band gap of MgO at high pressures. Furthermore,

we show that the refractive index of MgO reported here allows quantitative optical measurements of sample thickness and volume, which can be used in experiments to determine the density of non-crystalline solids at high pressure.

2.2 Experimental methods

2.2.1 Sample and preparations

High-pressure experiments were performed using symmetric DACs equipped with pairs of matching diamonds with culet sizes of 300/100 μm (beveled) and 400 μm (flat). Rhenium gaskets indented between the diamond anvils to a thickness of 10-25 μm were laser-drilled to create cylindrical holes with diameters of ~45 μm (for 300/100 μm anvils) and ~190 μm (for 400 μm anvils) to serve as sample chambers. For each loading we used a freshly cleaved piece of MgO with dimensions to fully fill the sample chamber. After placing the MgO sample without any pressure transmitting medium we immediately closed the DAC to minimize sample contamination by atmospheric moisture. Increasing the pressure to ~20 GPa was sufficient to obtain an optically homogenous sample, which is necessary for the refractive index measurements [35; 36]. Pressure was determined by measuring the shift of the high-frequency edge of the first-order Raman band of diamond with a relative uncertainty in pressure of ~5% [37].

2.2.2 Refractive index measurements at 600 nm

To measure the refractive index at high pressure we use the optical reflectivity method [35; 36; 38]. For a perpendicularly-incident light probe, the reflectivity of the diamond-sample interface ($R_{dia\text{-}smp}$) is related to the refractive indices of diamond (n_{dia}) and sample (n_{smp}):

$$R_{dia-smp} = \left|\frac{n_{smp}-n_{dia}}{n_{smp}+n_{dia}}\right|^2 \quad \text{(Eq. 2.1)}$$

The probe is a broadband laser (2 W Leukos New Wave supercontinuum, 400-2400 nm) inserted into the optical path of our DAC microscope [39] by a non-polarizing beam splitter cube after passing through a shortpass (~950 nm cutoff) and a variable neutral density filter. The use of a narrow, collimated laser beam (diameter of 1.2 mm at λ = 440 nm and 2.2 mm at λ = 800 nm) and a 20X apochromatic objective allowed for a near-normal incidence of the probe and a small probe diameter in the focal plane (~5 μm). The reflected beam was passed through a spatial filter (2 x 50 mm achromatic doublets and a 75 μm confocal pinhole) and recorded on a Pixis-256E CCD, installed on a Princeton Instruments SpectraPro HRS-300-SS spectrometer (grating 300 g/mm, blaze 500 nm, wavelength calibration accuracy ~0.5 nm).

In the case of a thin (~10-25 μm) transparent sample (such as MgO) in the DAC, the reflectivity of the diamond-sample interface can be expressed as [3]:

$$\frac{I_1+I_2}{I_0} = {R_{dia-smp}}^3 - 2{R_{dia-smp}}^2 + 2R_{dia-smp} \quad \text{(Eq. 2.2)},$$

where I_0 is the probe intensity striking the upstream diamond-sample interface. I_1, and I_2 are individual reflections from the upstream and downstream diamond-sample interfaces (**Figure 2-1 A**). The supplementary material of Lobanov et al. [3] presents derivations of Eq. 2.2. I_0 is obtained by measuring the amount of light reflected from a reference mirror (I_{mirror}) in the 500-800 nm range (where the reflectivity of the reference mirror is ~99%) and accounting for the light reflected from the upstream diamond-air interface. Because samples in DACs are thin, the reflected signal measured at the diamond-sample interface is a combination of I_1 and I_2 contributions. Accounting for back reflections at the diamond-sample and diamond-air interfaces we obtain the intensity ratio spectrum ($I_{ratio} = \frac{I_1+I_2}{I_0}$). Averaging $\frac{I_1+I_2}{I_0}$ (**Figure 2-1 B**) over the 550-650 nm range (where the reflectivity of the reference mirror is nearly flat) allows solving Eq. 2.2 for $R_{dia\text{-}smp}$. Please note that averaging the I_{ratio} spectrum at 550-650 nm (i.e., over a set of 370 individual intensity data due to the wavelength resolution of our system) provides a statistically more significant average than only averaging I_{ratio} at the interference pattern extrema observed at ~550-650 nm (typically, less than 20). Using $R_{dia\text{-}smp}$, we solve Eq. 2.1 for n_{smp} of MgO at 600 nm under the assumption of a pressure-independent refractive index of diamond (n_{dia} = 2.418 [20]). This is a reasonable assumption as discussed by Zha et al. [36] and Lobanov et al. [3] based on the high-pressure reflectivity of a reference material and small dispersion of diamond. The refractive index of MgO reported here provides further evidence for the adequacy of this assumption, as discussed in Sec. 3. Solutions to Eq. 2.1 and 2.2 were found using NumPy [40] and SymPy [41] Python libraries.

We also measured the refractive index of MgO at 1 atm by probing the reflectivity of the MgO-air interface of a large (~1 mm) free-standing freshly-cleaved sample. Eq. 2.1 was then modified (n_{air} = 1) and solved for the refractive index of MgO. We empirically estimate the apparently random error in all refractive indices of MgO reported in this work at ~±1% [3]. This estimate is based on the reproducibility of refractive indices measured at the same DAC load and sample position. Improvements on the reproducibility of sample positioning and a high-resolution tilting DAC stage as well as accurate characterization of the variation in probe intensity over the typical measurement time (~10 min) may help to reduce random variations in the measured refractive index.

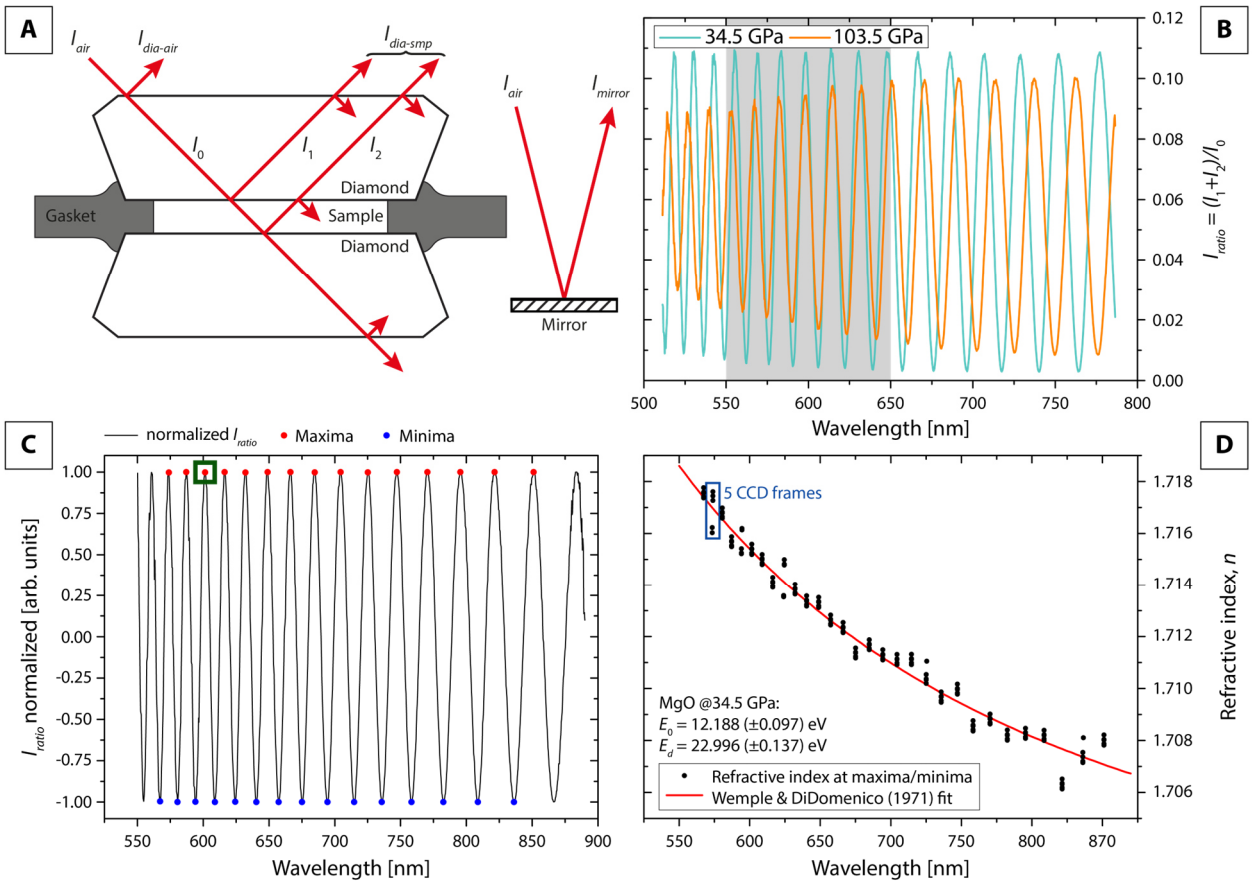

Figure 2-1 A: Reflectivity measurement in diamond anvil cell. Perpendicularly-incident probe laser is partially reflected at diamond-air and diamond-sample interfaces. Oblique probe incidence is depicted for clarity. **B**: Measured intensity ratio spectra (MgO run 4 at 34.5 and 103.5 GPa) is averaged over 550-650 nm (grey area) to solve Eq. 2.2 for $R_{dia\text{-}smp}$. The different contrast of the patterns at 34.5 and 103.5 GPa is due to diamond cupping, which has been shown to have no apparent effect on the inferred refractive index [35]. **C**: Normalized intensity ratio spectrum from reflectivity measurements in a DAC (MgO run 4 at 34.5 GPa). The blue and red dots are local extrema. The green square highlights the extremum closest to 600 nm. **D**: The wavelength-dispersion of the MgO refractive index at 34.5 GPa and its Wemple & DiDomenico [2] single-effective-oscillator fit.

2.2.3 Dispersion of the refractive index

The intensity ratio spectrum is an interference pattern because the DAC sample cavity is a Fabry-Perot interferometer. The interference condition for each of the observed minima and maxima is

$$\lambda k(\lambda) = 2dn_{smp}(\lambda) \qquad \text{(Eq. 2.3)}$$

where $k(\lambda)$ is the interference order number of the extremum (in half-integer step sizes) observed at wavelength λ, d is sample thickness, and $n_{smp}(\lambda)$ is the refractive index of the sample at the extremum. The refractive index of the sample measured at 600 nm allows analyzing the interference pattern for index dispersion. This requires, however, that chromatic aberrations due the use of refractive optics are minimized and that the determination of extrema wavelengths is as accurate as possible. Towards this end, the reflectance spectra were also collected with a 10X apochromatic objective whose reduced numerical aperture (0.26 for 10X vs 0.4 for 20X) allows minimizing chromatic aberrations. The reflected signal was recorded

by a Princeton Instruments Acton SP-2150i spectrometer (300 g/mm, blaze 750 nm) with a with Pixis-100B eXcelon CCD detector, which enabled for a wavelength resolution of ~0.4 nm/pixel.

Writing Eq. 2.3 for any pair of extrema (e.g., at k and k+1) and using the index measured at 600 nm we can estimate the sample thickness. Here, however, we obtain a more precise estimate of sample thickness by iterating through all the extrema while assuming n_{smp} is wavelength-independent. The latter assumption is reasonable to first-order and contributes only a small systematic error to the thickness estimate (< ~1% of the value) because the index dispersion of MgO over the 550-870 nm range is only ~0.85% (1 atm) [42]. Using the sample thickness in Eq. 2.3 we can now find the interference order number of the extremum closest to 600 nm (**Figure 2-1**, **C**) and then use it to assign the interference order to all the other observed extrema. Finally, we use Eq. 2.3 to obtain the refractive index at all the extrema using their respective interference order numbers. A repeated collection of five CCD frames at the same sample position allowed minimizing random errors in the measured index dispersion due to CCD noise (**Figure 2-1, D**). To further account for small variations in the measurement position, we collected additional spectra ~2-5 μm off the central sample position. This allowed evaluating the combined random and systematic relative errors in the measured index dispersion, which are ~1.2% at 18.8 GPa and ~7.5% at 103.5 GPa. We attribute the increase in error with pressure to the expected diamond cupping at high pressure [43; 44], which introduces slight (~20-40 nm) wavelength-dependent differences in the optical path length ($n_{smp}d$) of the probe in the DAC sample due to the wavelength-dependent beam diameter of the light probe (due to the light source characteristics and unavoidable chromatic aberration).

2.2.4 Measurements of sample thickness, area, and volume

Sample thickness at the center of the sample chamber was determined using the refractive index of MgO at 600 nm. Due to diamond cupping, expected at high pressure, we also measured the sample thickness at the periphery of the sample at four distinct locations ~5 μm from the gasket edge (**Figure 2-3 A**, inset). The averaged sample thickness at the periphery (d_{edge}) and at sample center (d_{center}) were then used to evaluate the mean sample thickness (d_{mean}). To measure the area (A) of the sample we analyzed images of both sides of the DAC recorded by a FLIR Blackfly BFS-U3-50S5C-C camera (1 px ≈ 0.013 μm²) and calculated the average. All images were taken at fixed back-illumination conditions and analyzed using ImageJ [45] by converting the image into an 8-bit grayscale and finding all the pixels with brightness higher than a threshold (value: 61). These measurements allowed us to derive the absolute volume ($V = A \cdot d_{mean}$) of MgO samples as a function of pressure. As was shown by Lobanov et al. [3] this approach is sufficient to achieve relative errors of ~1.5% for A that propagate together with the error in d_{mean} to a ~3% error in V.

2.3 Results

The refractive index of MgO at 600 nm decreases with pressure by ~2.4% from ~1.737 at 1 atm to ~1.696 (±0.017) at ~140 GPa (**Figure 2-2**). The index at 600 nm measured here is ~1% higher than that determined

in shockwave experiments of Fratanduono et al. [31] at 1550 nm. This difference is consistent with the decrease of the refractive index of MgO by ~1.2% from 600 to 1500 nm at 1 atm [42]. Our results are also in agreement with the local-density approximation (LDA) DFT calculations of Oganov et al. [29] but the computed index is systematically higher than that measured in experiments, likely due to the tendency of LDA-DFT to underestimate the band gap [46].

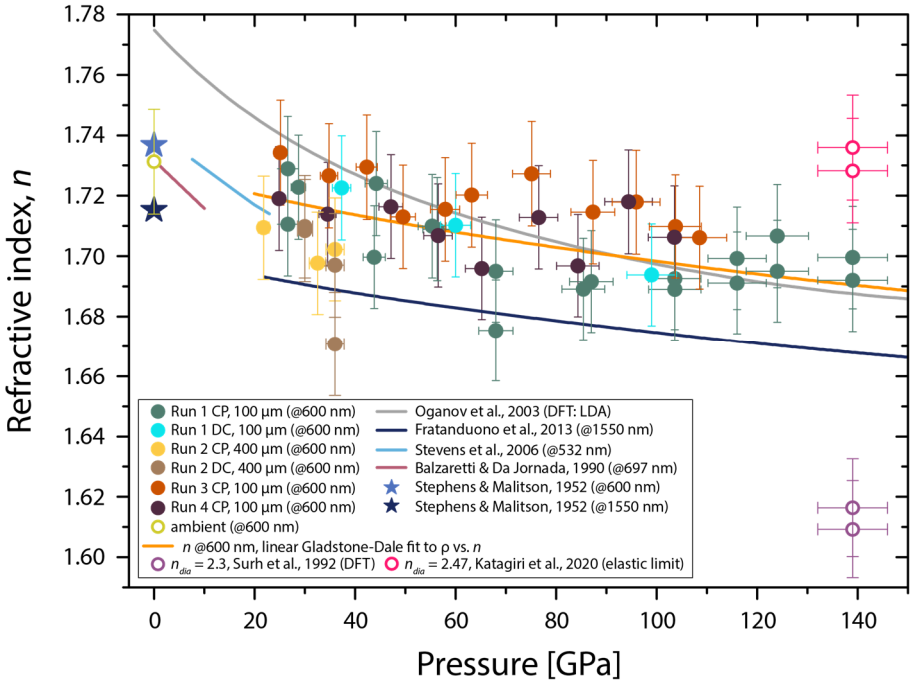

Figure 2-2 The refractive index of MgO at 600 nm measured in this work (circles, where CP = compression, DC = decompression) compared to shock wave data at 1550 nm [31] (dark blue curve, with uncertainties as large as 1% of the measurements) and at 532 nm (light blue curve), interferometry measurements (rose curve) [33] and computations by Oganov et al. [29] (grey curve). Orange line is n(P) based on linear Gladstone-Dale fit using experimental n and ϱ from Tange et al. [30]. The refractive index at 1 atm is after Stephens & Malitson [42] and is shown by light blue (at 600 nm) and dark blue (1550 nm) stars. Violet and pink open circle are MgO refractive indices obtained by assuming n_{dia} = 2.3 [47] and n_{dia} = 2.47 [48].

Both sample thickness and area decrease with increasing pressure (**Figure 2-3**). Diamond cupping is evident as the sample thickness near the gasket edge is systematically smaller than the thickness at sample center at P > 30-40 GPa, consistent with previous measurements of diamond-diamond separation in DAC experiments [3; 43; 44]. We observe a maximum relative difference of ~2% between center and periphery as well as an overall thinning of the sample by ~14% from ~19 to ~103 GPa. The evolution of the absolute volume of the MgO sample at high pressure allows quantifying its density if the MgO density at a reference pressure is known. The density of MgO at high pressure calculated from our P-V data (**Figure 2-4**, **A**) is in agreement with the EOS of Tange et al. [30] within ~1%, better than the ~3% error in density estimated by Lobanov et al. [3]. Overall, our density data confirms that optical measurements of sample area and thickness are able to constrain the evolution of the density of transparent samples upon compression up to ~140 GPa [3]. We note, that the here used threshold value for A measurements is different than the one in the supplementary of Lobanov et al. [3], because of different illumination settings and opposite definition (0 or 255) of black/white in the used software.

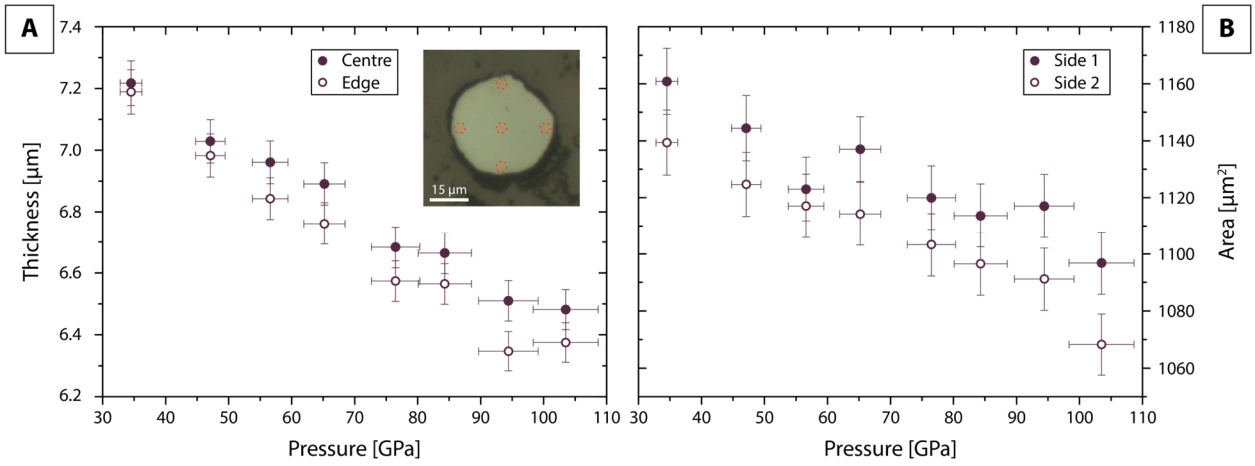

Figure 2-3 Measured MgO geometry upon compression in run 4 (300/100 µm culet). **A**: Sample thickness at the center and periphery of the DAC cavity (the average of four measurements ~5 µm away from the gasket edge). Inset: optical image of the MgO sample at 24.9 GPa with approximate positions of thickness measurements). **B**: Sample area measured from two sides of the DAC.

We derive the Gladstone-Dale relation [49], fitted to the refractive index data above 20 GPa, using the following parameters: $n = -0.0234 \times \rho + 1.8137$ (uncertainty in $n \sim 1.5\%$), where ϱ is the pressure-dependent density in g/cm³. Based on our refractive index data and the EOS of MgO [30], we calculated the Lorenz-Lorentz polarizability, α_{LL}, as

$$\alpha_{LL} = \frac{3M(n^2-1)}{\rho 4\pi(n^2+2)} \quad \text{(Eq. 2.4)},$$

where we inserted the molar weight of MgO (M) (40.3044 g/mol), the pressure-dependent density (ϱ) calculated from MgO EOS [30] and refractive index (n). Propagating the uncertainties for ϱ [50] (1%) and for n (1%) the relative error on α_{LL} is 2%. The non-linear behavior of α_{LL} as a function of pressure is due to its inverse-proportional relationship with density in Lorenz-Lorentz formula, and on the intrinsic non-linear behavior of the refractive index as a function of pressure. The model value of α_{LL} obtained from the density (and pressure) dependence of n using the Gladstone-Dale relation well reproduces the full set of calculated α_{LL} (see **Figure 2-4 B**).

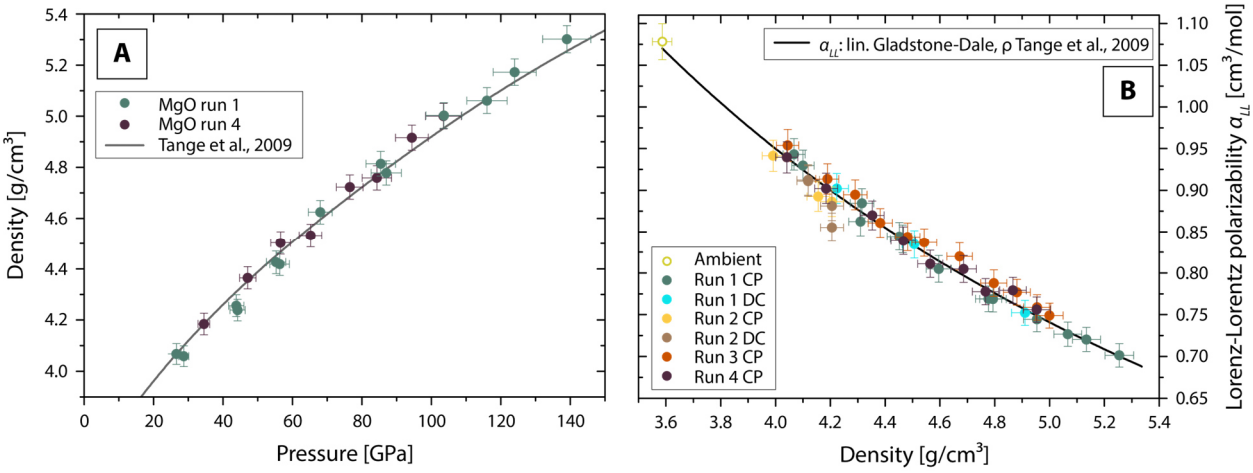

Figure 2-4 A: MgO density measured in this work (circles) compared to data from Tange et al. [30]. Reference pressures/densities are 26.6 GPa (run 1) and 34.5 GPa (run 4). **B**: Experimentally constrained Lorenz-Lorentz polarizability (α_{LL}, Eq. 2.4) evaluated using experimental n and ϱ from Tange et al. [30], black line is α_{LL} calculated from the linear Gladstone-Dale relationship of ϱ [30] and n to $P \geq 20$ GPa (i.e., $\varrho \geq 3.96$ g/cm³).

In one of the runs (run 4) we measured the dispersion of the refractive index of MgO, which decreases upon compression by ~28% (**Figure 2-5**, **A)**, with $\Delta n_{550\text{-}870\text{nm}}$ being reduced by ~0.004 from ~0.015 at 1 atm to ~0.011 ($\pm 8.04 \times 10^{-4}$) at ~103 GPa (**Figure 2-5**, **B**). Qualitatively, the nearly pressure-independent index at 600 nm and the decrease in index dispersion suggest that the valence-to-conduction band energy separation (band gap) is increasing with pressure. One way to quantify the band gap is to analyze the index dispersion by the single-effective-oscillator model of Wemple & DiDomenico [2]. In this model, the wavelength dependence of the refractive index is related to two fitting parameters E_0 and E_d which describe the single oscillator energy and dispersion energy (in eV):

$$n(\lambda) = \sqrt{\frac{E_d E_0}{E_0^2 - \left(\frac{hc}{\lambda}\right)^2} + 1} \qquad \text{(Eq. 2.5)}$$

Here, h is the Planck's constant in eV·s and c the speed of light in m/s and λ the wavelength in m. Empirically, E_d is related to the chemical bonding environment (e.g. cation coordination number) and the distribution of charge around the anion (i.e., bonding character), while E_0 is related to the average valence-to-conduction band energy separation [2; 51].

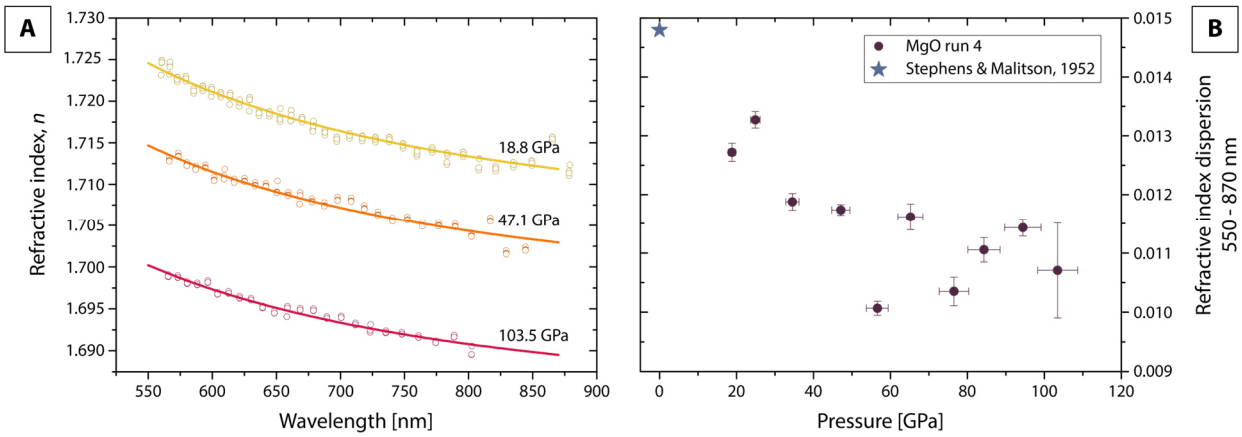

Figure 2-5 Wemple-DiDomenico best fits to the experimental dispersion of the refractive index of MgO run 4 at selected pressures (**A**) and plotted as the difference between measured refractive indices at 550 and 870 nm (**B**).

Fitting the single-effective-oscillator model of Wemple & DiDomenico [2] (Eq. 2.5) to our wavelength-dispersion data we find E_0 and E_d for the studied pressure range (**Figure 2-1, D**). E_d increases from ~21.6 eV (1 atm) to ~23.2 (±0.9) eV at ~103.5 GPa. The slight increase in E_d with pressure may indicate modest charge redistribution around oxygen. Using the empirical relationship that the oscillator energy E_0 is approximately 1.5 times greater than the optical gap [2] we experimentally constrain the band gap of MgO. $E_0/1.5$ increases by ~1 eV from 7.4 eV at 1 atm [42] to 8.5 (±0.6) at 103 GPa (**Figure 2-6**). A pressure-induced increase of the band gap in MgO is consistent with most DFT calculations in the literature [52–55]. However, DFT studies generally show a lower gap energy and a stronger effect of pressure on the increasing band gap energy.

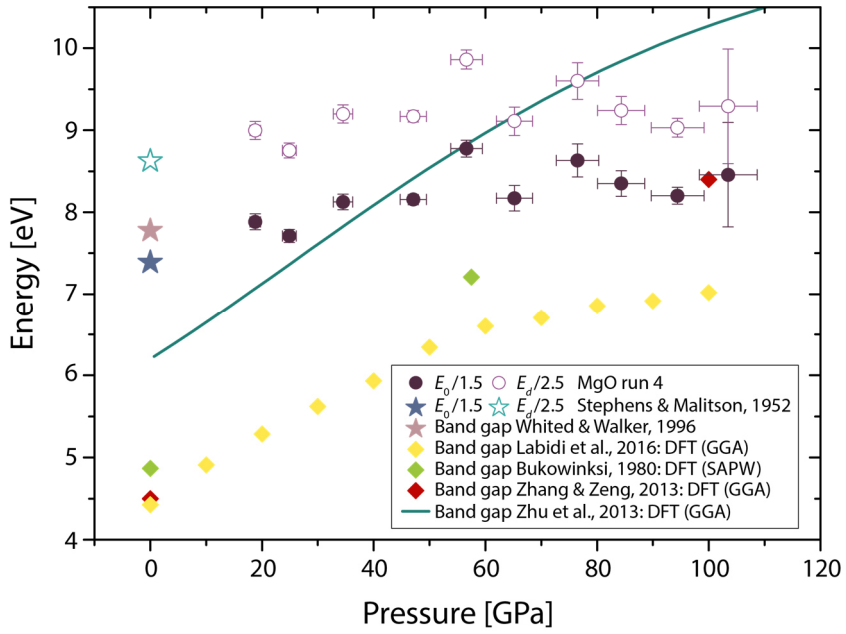

Figure 2-6 Results of the Wemple & DiDomenico [2] fit (here $E_0/1.5$) to the dispersion of the measured index of MgO (circles). The (experimental) data at 1 atm are from Stephens & Malitson [42] (blue star) and Whited & Walker [56] (pink star). In addition, we show calculations from literature for the band gap in MgO (green line and diamonds) [52–55]. Legend abbreviations: generalized gradient approximation (GGA), symmetrized augmented plane wave (SAPW).

2.4 Discussion

At ambient pressure, our refractive index measurement (without using a DAC) is in agreement with existing experimental data (e.g., Stephens & Malitson [42]). The overall decrease of the refractive index with pressure is consistent with DFT computations [29] and shockwave experiments [31]. Even though diamond cupping produces non-parallelism of the culet faces, we note that a small beam diameter as used here, still allows reliable refractive index measurements at the center of the culet, consistent with the results of Van Straaten & Silvera [35] who found that the cupping only affects the fringes contrast and not the total reflected signal. However, earlier experimental reports at P <23 GPa show a steeper decrease with P. Vedam & Schmidt [32] found that the index of MgO at 589.3 nm decreases with P by -1.58x10^{-3}/GPa up to 0.7 GPa. Similarly, Balzaretti & Da Jornada [33] found n at 697 nm to decrease by -1.21x10^{-3}/GPa at a maximum P of 10 GPa. In their shockwave experiments Stevens et al. [34] used the density dependence of n and (indirectly) derived a decrease of n by -1.19x10^{-3}/GPa at 532 nm up to ~23 GPa. It is likely that the ~1% relative uncertainty in the refractive index at 600 nm reported here does not allow resolving the stronger dependence of the index on P at P <30 GPa. The general trend of n decreasing on compression is due to a decreasing electronic polarizability, counterbalancing the increase of density with pressure (**Figure 2-4**).

In our refractive index measurements, we assumed a constant refractive index for diamond. According to Katagiri et al. [48], however, uniaxial shock-compression of diamond to 140 GPa (4.2 g/cm³) increases its refractive index at 532 nm by ~2% (elastic limit). Assuming n_{dia} = 2.47 at 140 GPa (elastic limit), we derive n_{MgO} = 1.736 (±0.017), that is 2% higher than n_{MgO} = 1.699 obtained assuming a stress-independent index of diamond (n_{dia} = 2.418). We note, however, that within their propagated 1σ uncertainty, Katagiri et al. [48] cannot exclude that n_{dia} is constant up to 129 GPa. In addition, such an upward revision in the index of MgO is not justified because it would imply that the refractive index of MgO is constant at P = 0-140 GPa, inconsistent with earlier shockwave measurements and theoretical computations that show that the index of MgO decreases with pressure (**Figure 2-2**). Other reports [47; 57] on the high-pressure behavior of diamond refractive index suggested, that it decreases by up to 5% upon compression to 140 GPa : n_{dia} = 2.3. Using this value to analyze the diamond-MgO interface we obtain n_{MgO} = 1.617 (±0.016), again inconsistent with the shockwave [31] and DFT data [29] (**Figure 2-2**). Katagiri et al. [48] discussed that the response of diamond refractive index to pressure is a function of deformation conditions which are likely different in diamond anvil cells ($\frac{dn_{dia}}{dP} < 0$ [57]) and shockwave experiments ($\frac{dn_{dia}}{dP} > 0$ [48]). This interpretation is supported by the DFT computations of Surh et al. [47] who found that $\frac{dn_{dia}}{dP}$ is negative upon hydrostatic compression but may be both positive and negative upon uniaxial compression (depending on the principal strain direction). Because the complex deformation regime of the diamond anvil tip results in its non-isotropic optical behavior (birefringence) at high pressure, it is possible that the net effect is that n_{dia} is essentially pressure independent. However, we cannot rule out that the assumption of n_{dia} = *constant* in our work contributes a systematic error that at 140 GPa exceeds the empirically estimated error of ±1%, despite this assumption providing optimal agreement with independent shockwave data on n_{MgO}, theoretical computations, as well as its pressure-density data. Therefore, we provide tabulated reflectivity data for the diamond-MgO interface in the

Supplementary Information, which can be easily reanalyzed using the Fresnel equation (Eq. 2.1). We maintain, however, that the cases of H_2O and SiO_2 glass constitute indirect justification that the assumption $n_{dia} = constant$ is reasonable because the pressure-density data for these materials is reproduced [3; 36]. A change in n_{dia} by ±2-5% percent (as discussed above) would result in the proportional under/over estimation of sample thickness and thus pay a ±2-5% systematic error in the sample density, which is not the case in H_2O [36] and SiO_2 glass [3], nor it is the case in the present study on MgO.

The continuous decrease in index dispersion of MgO at 550-870 nm ($\Delta n_{550\text{-}870nm}$) is noteworthy, as it indicates an ongoing change in the electronic structure near the valence band maximum and conduction band minimum. The band gap of MgO at 1 atm is ~7.8 eV based on the reflectance measurements in the UV and VIS ranges [56; 58]. These band gap estimates are also consistent with independent determinations from reflection electron energy loss spectroscopy that yielded ~7.8 eV [59]. The Wemple & DiDomenico [2] fit to the refractive index spectrum at 1 atm [42] yields $E_0/1.5$ = 7.4 eV, broadly consistent with the MgO band gap reported in the literature. This lends support to the $E_0/1.5$ empirical relation, although this ratio is certainly not universal [60–62]. In the absences of direct measurements of the band gap of MgO at high pressure, $E_0/1.5$ provides a convenient and semi-quantitative mean of constraining the band gap of MgO.

To our knowledge, the here shown results (**Figure 2-6**) represent the first experimental high-pressure constraint on the optical band gap of MgO. Specifically, we observe an opening of the band gap in MgO from 7.8 eV [56] at 1 atm by ~1 eV upon compression to 103 GPa. The opening is related to a shift of the conduction band towards higher energies, whereas the valence bands are almost insensitive to pressure [53]. The band gap of MgO at high pressure inferred in this work is higher by ~3 eV than the results of most DFT calculations, likely due to the underestimation of the band gap by DFT [46; 63].

We constrain how the geometry of a MgO DAC sample (100 μm) evolves on compression up to >100 GPa (**Figure 2-3**). Generally, a cupping of the diamonds is expected in almost all DAC experiments, resulting in a thinner sample away from its center. Li et al. [44] reports cupping at pressures as low as 10 GPa, which is consistent with our measurements that readily resolve cupping at P ~30 GPa. Future DAC experiments can use the pressure dependence of the refractive index to quantify sample thicknesses by white light interferometric measurements. This is directly relevant for radiative and lattice thermal conductivity measurements where sample thickness is crucial for getting accurate results. The pressure dependence of the refractive index found here can be used to calculate the radiative conductivity [4] of (Mg,Fe)O samples at high pressure under the assumption that the addition of moderate amounts of iron in substitution of Mg does not change the pressure dependence of the refractive index. The extension of the 600 nm refractive index of MgO up to 140 GPa can also be beneficial for shockwave experiments using MgO as an interferometer window material, since previous studies in the VIS range are only limited to <23 GPa [34].

Because of the uniaxial stress conditions present in the DAC sample chamber, radial strain and radial pressure gradients could be strong. However, we were not able to reliably resolve pressure gradients across the studied sample within the accuracy of the pressure determination method (5% [37]). Also, given the slight changes in n with P, small pressure gradients will have no measurable effect on the derived sample thickness

and density. We are able to reproduce the pressure-dependent density within 1% with respect to the published EOS of MgO (300 K) by Tange et al. [30]. Overall, the agreement between the pressure-volume data measured here and that expected from the MgO EOS within ~1% confirms the applicability of the optical determination of sample density [3; 35; 36], which could be beneficial for high-pressure studies of non-crystalline materials.

2.5 Conclusions

We presented the evolution of the refractive index of MgO at 600 nm up to ~140 GPa. With the pressure dependence of the refractive index, we demonstrate a reliable way to accurately determine thicknesses by the analysis of interference fringe distances which can be applied to any DAC experiment using MgO as a sample or pressure transmitting medium. We show that simple and straightforward in-house DAC experiments can help to derive sample densities at pressures >1 Mbar. Even though the error of this kind of measurements is certainly larger compared to synchrotron-based techniques (<0.1% [64], for crystalline materials), it provides reliable estimations of the densification trend if the density at one reference pressure is known. We also experimentally constrained the pressure dependence of the band gap for MgO and show that it opens by ~1 eV over a 100 GPa range, considerably less than what is expected from DFT calculations. This implies that over the whole pressure range of the Earth's lower mantle, pressure has only minor effects on the electrical conductivity of MgO.

2.6 References

[1] Hervé, P. & Vandamme, L. (1994): General relation between refractive index and energy gap in semiconductors. *Infrared Phys. Technol., 35 (4)*, 609–615, doi: 10.1016/1350-4495(94)90026-4.

[2] Wemple, S.H. & DiDomenico, M. (1971): Behavior of the electronic dielectric constant in covalent and ionic materials. *Phys. Rev. B, 3 (4)*, 1338–1351, doi: 10.1103/PhysRevB.3.1338.

[3] Lobanov, S.S.; Speziale, S.; Winkler, B.; Milman, V. *et al.* (2022): Electronic, structural, and mechanical properties of SiO_2 glass at high pressure inferred from its refractive index. *Phys. Rev. Lett., 128 (7)*, 77403, doi: 10.1103/PhysRevLett.128.077403.

[4] Clark, S.P. (1957): Radiative transfer in the Earth's mantle. *Trans. AGU, 38 (6)*, 931, doi: 10.1029/TR038i006p00931.

[5] Grose, C.J. & Afonso, J.C. (2019): New constraints on the thermal conductivity of the upper mantle from numerical models of radiation transport. *Geochem. Geophys. Geosyst., 20 (5)*, 2378–2394, doi: 10.1029/2019GC008187.

[6] Keppler, H.; Dubrovinsky, L.S.; Narygina, O.; Kantor, I. (2008): Optical absorption and radiative thermal conductivity of silicate perovskite to 125 gigapascals. *Science, 322 (5907)*, 1529–1532, doi: 10.1126/science.1164609.

[7] Goncharov, A.F.; Lobanov, S.S.; Tan, X.; Hohensee, G.T. *et al.* (2015): Experimental study of thermal conductivity at high pressures. *Phys. Earth Planet. Inter., 247*, 11–16, doi: 10.1016/j.pepi.2015.02.004.

[8] Konôpková, Z.; McWilliams, R.S.; Gómez-Pérez, N.; Goncharov, A.F. (2016): Direct measurement of thermal conductivity in solid iron at planetary core conditions. *Nature, 534 (7605)*, 99–101, doi: 10.1038/nature18009.

[9] Ohta, K.; Kuwayama, Y.; Hirose, K.; Shimizu, K.; Ohishi, Y. (2016): Experimental determination of the electrical resistivity of iron at Earth's core conditions. *Nature, 534 (7605)*, 95–98, doi: 10.1038/nature17957.

[10] Lobanov, S.S.; Holtgrewe, N.; Lin, J.-F.; Goncharov, A.F. (2017): Radiative conductivity and abundance of post-perovskite in the lowermost mantle. *Earth Planet. Sci. Lett., 479*, 43–49, doi: 10.1016/j.epsl.2017.09.016.

[11] Geballe, Z.M.; Sime, N.; Badro, J.; Van Keken, P.E.; Goncharov, A.F. (2020): Thermal conductivity near the bottom of the Earth's lower mantle: Measurements of pyrolite up to 120 GPa and 2500 K. *Earth Planet. Sci. Lett., 536*, 116161, doi: 10.1016/j.epsl.2020.116161.

[12] Lobanov, S.S.; Holtgrewe, N.; Ito, G.; Badro, J. *et al.* (2020): Blocked radiative heat transport in the hot pyrolitic lower mantle. *Earth Planet. Sci. Lett., 537*, 116176, doi: 10.1016/j.epsl.2020.116176.

[13] Okuda, Y.; Ohta, K.; Hasegawa, A.; Yagi, T. *et al.* (2020): Thermal conductivity of Fe-bearing post-perovskite in the Earth's lowermost mantle. *Earth Planet. Sci. Lett., 547*, 116466, doi: 10.1016/j.epsl.2020.116466.

[14] Lobanov, S.S.; Soubiran, F.; Holtgrewe, N.; Badro, J. *et al.* (2021): Contrasting opacity of bridgmanite and ferropericlase in the lowermost mantle: Implications to radiative and electrical conductivity. *Earth Planet. Sci. Lett., 562*, 116871, doi: 10.1016/j.epsl.2021.116871.

[15] Murakami, M.; Goncharov, A.F.; Miyajima, N.; Yamazaki, D.; Holtgrewe, N. (2022): Radiative thermal conductivity of single-crystal bridgmanite at the core-mantle boundary with implications for thermal evolution of the Earth. *Earth Planet. Sci. Lett., 578*, 117329, doi: 10.1016/j.epsl.2021.117329.

[16] Setchell, R.E. (1979): Index of refraction of shock-compressed fused silica and sapphire. *J. Appl. Phys., 50 (12)*, 8186–8192, doi: 10.1063/1.325959.

[17] Shand (2010): The chemistry and technology of magnesia. Hoboken, N.J: Wiley-Interscience.

[18] McWilliams, R.S.; Spaulding, D.K.; Eggert, J.H.; Celliers, P.M. *et al.* (2012): Phase transformations and metallization of magnesium oxide at high pressure and temperature. *Science, 338 (6112)*, 1330–1333, doi: 10.1126/science.1229450.

[19] Musella, R.; Mazevet, S.; Guyot, F. (2019): Physical properties of MgO at deep planetary conditions. *Phys. Rev. B, 99 (6)*, doi: 10.1103/PhysRevB.99.064110.

[20] Hynes (2016): CRC Handbook of Chemistry and Physics. 97th ed. Boca Raton, London, New York: CRC Press.

[21] Wilson, I.O. (1981): Magnesium oxide as a high-temperature insulant. *IEE Proc. A Phys. Sci. Meas. Instrum. Manage. Educ. Rev. UK, 128 (3)*, 159, doi: 10.1049/ip-a-1.1981.0026.

[22] Belonoshko, A.B.; Arapan, S.; Martonak, R.; Rosengren, A. (2010): MgO phase diagram from first principles in a wide pressure-temperature range. *Phys. Rev. B, 81 (5)*, doi: 10.1103/physrevb.81.054110.

[23] Soubiran, F. & Militzer, B. (2020): Anharmonicity and Phase Diagram of Magnesium Oxide in the Megabar Regime. *Phys. Rev. Lett., 125 (17)*, 175701, doi: 10.1103/PhysRevLett.125.175701.

[24] Coppari, F.; Smith, R.F.; Wang, J.; Millot, M. *et al.* (2021): Implications of the iron oxide phase transition on the interiors of rocky exoplanets. *Nat. Geosci., 14 (3)*, 121–126, doi: 10.1038/s41561-020-00684-y.

[25] Onodera, A.; Suito, K.; Kawai, N. (1980): Semisintered oxides for pressure-transmitting media. *J. Appl. Phys., 51 (1)*, 315–318, doi: 10.1063/1.327374.

[26] Panero, W.R. & Jeanloz, R. (2001): The effect of sample thickness and insulation layers on the temperature distribution in the laser-heated diamond cell. *Rev. Sci. Instrum., 72 (2)*, 1306, doi: 10.1063/1.1343863.

[27] Pigott, J.S.; Reaman, D.M.; Panero, W.R. (2011): Microfabrication of controlled-geometry samples for the laser-heated diamond-anvil cell using focused ion beam technology. *Rev. Sci. Instrum., 82 (11)*, 115106, doi: 10.1063/1.3658482.

[28] Dorfman, S.M.; Prakapenka, V.B.; Meng, Y.; Duffy, T.S. (2012): Intercomparison of pressure standards (Au, Pt, Mo, MgO, NaCl and Ne) to 2.5 Mbar. *J. Geophys. Res., 117 (B8)*, B08210, doi: 10.1029/2012JB009292.

[29] Oganov, A.R.; Gillan, M.J.; Price, G.D. (2003): Ab initio lattice dynamics and structural stability of MgO. *J. Chem. Phys., 118 (22)*, 10174–10182, doi: 10.1063/1.1570394.

[30] Tange, Y.; Nishihara, Y.; Tsuchiya, T. (2009): Unified analyses for *P-V-T* equation of state of MgO. *J. Geophys. Res., 114 (B3)*, B03208, doi: 10.1029/2008JB005813.

[31] Fratanduono, D.E.; Eggert, J.H.; Akin, M.C.; Chau, R.; Holmes, N.C. (2013): A novel approach to Hugoniot measurements utilizing transparent crystals. *J. Appl. Phys., 114 (4)*, 43518, doi: 10.1063/1.4813871.

[32] Vedam, K. & Schmidt, E.D. D. (1966): Variation of refractive index of MgO with pressure to 7 kbar. *Phys. Rev., 146 (2)*, 548–554, doi: 10.1103/PhysRev.146.548.

[33] Balzaretti, N.M. & Da Jornada, J.A. H. (1990): Volume dependence of the electronic polarizability of magnesium oxide. *High Pressure Res., 2 (3)*, 183–191, doi: 10.1080/08957959008201037.

[34] Stevens, G.D.; Veeser, L.R.; Rigg, P.A.; Hixson, R.S. (2006): Suitability of magnesium oxide as a VISAR window. In: Furnish, Elert, Russel & White (Eds.) AIP conference proceedings 2272 A, 845, 1353–1356.

[35] Van Straaten, J. & Silvera, I.F. (1988): Equation of state of solid molecular H_2 and D_2 at 5 K. *Phys. Rev. B Condens. Matter, 37 (4)*, 1989–2000, doi: 10.1103/PhysRevB.37.1989.

[36] Zha, C.-S.; Hemley, R.J.; Gramsch, S.A.; Mao, H.-K.; Bassett, W.A. (2007): Optical study of H_2O ice to 120 GPa. *J. Chem. Phys., 126 (7)*, 74506, doi: 10.1063/1.2463773.

[37] Akahama, Y. & Kawamura, H. (2006): Pressure calibration of diamond anvil Raman gauge to 310 GPa. *J. Appl. Phys., 100 (4)*, 43516, doi: 10.1063/1.2335683.

[38] Kim, Y.-J.; Celliers, P.M.; Eggert, J.H.; Lazicki, A.; Millot, M. (2021): Interferometric measurements of refractive index and dispersion at high pressure. *Sci. Rep., 11 (1)*, 5610, doi: 10.1038/s41598-021-84883-6.

[39] Lobanov, S.S.; Schifferle, L.; Schulz, R. (2020): Gated detection of supercontinuum pulses enables optical probing of solid and molten silicates at extreme pressure-temperature conditions. *Rev. Sci. Instrum., 91 (5)*, 53103, doi: 10.1063/5.0004590.

[40] Van der Walt, S.; Colbert, S.C.; Varoquaux, G. (2011): The NumPy array: a structure for efficient numerical computation. *Comput. Sci. Eng., 13 (2)*, 22–30, doi: 10.48550/arXiv.1102.1523.

[41] Meurer, A.; Smith, C.P.; Paprocki, M.; Čertík, O. *et al.* (2017): SymPy: symbolic computing in Python. *PeerJ Comput. Sci., 3*, e103, doi: 10.7717/peerj-cs.103.

[42] Stephens, R.E. & Malitson, I.H. (1952): Index of refraction of magnesium oxide. *J. Res. Natl. Bur. Stand., 49 (4)*, 249–252, doi: 10.6028/jres.049.025.

[43] Hemley, R.J.; Mao, H.-K.; Shen, G.; Badro, J. *et al.* (1997): X-ray Imaging of Stress and Strain of Diamond, Iron, and Tungsten at Megabar Pressures. *Science, 276 (5316)*, 1242–1245, doi: 10.1126/science.276.5316.1242.

[44] Li, B.; Ji, C.; Yang, W.; Wang, J. *et al.* (2018): Diamond anvil cell behavior up to 4 Mbar. *Proc. Natl. Acad. Sci. U.S.A., 115 (8)*, 1713–1717, doi: 10.1073/pnas.1721425115.

[45] Abramoff, M.D.; Magalhaes, P.J.; Ram, S.J. (2004): Image Processing with ImageJ. *Biophotonics Int., 11 (7)*, 36–42.

[46] Morales-García, Á.; Valero, R.; Illas, F. (2017): An empirical, yet practical way to predict the band gap in solids by using density functional and structure calculations. *J. Phys. Chem. C, 121 (34)*, 18862–18866, doi: 10.1021/acs.jpcc.7b07421.

[47] Surh, M.P.; Louie, S.G.; Cohen, M.L. (1992): Band gaps of diamond under anisotropic stress. *Phys. Rev. B Condens. Matter, 45 (15)*, 8239–8247, doi: 10.1103/PhysRevB.45.8239.

[48] Katagiri, K.; Ozaki, N.; Miyanishi, K.; Kamimura, N. *et al.* (2020): Optical properties of shock-compressed diamond up to 550 GPa. *Phys. Rev. B, 101 (18)*, doi: 10.1103/PhysRevB.101.184106.

[49] Gladstone, J.H. & Dale, T.P. (1863): XIV. Researches on the refraction, dispersion, and sensitiveness of liquids. *Phil. Trans. R. Soc., 153*, 317–343, doi: 10.1098/rstl.1863.0014.

[50] Liu, L. & Bi, Y. (2016): How far away are accurate equations of state determinations? Some issues on pressure scales and non-hydrostaticity in diamond anvil cells. *MRE, 1 (4)*, 224–236, doi: 10.1016/j.mre.2016.06.002.

[51] Wemple, S.H. & DiDomenico, M. (1969): Optical dispersion and the structure of solids. *Phys. Rev. Lett., 23 (20)*, 1156–1160, doi: 10.1103/PhysRevLett.23.1156.

[52] Bukowinski, M.S. T. (1980): Effect of pressure on bonding in MgO. *J. Geophys. Res., 85 (B1)*, 285–292, doi: 10.1029/JB085IB01P00285.

[53] Zhang, J. & Zeng, Z. (2013): Electronic and optical properties of perfect MgO and MgO with *F* center under high pressure. *Int. J. Mod. Phys. C, 24 (08)*, 1350052, doi: 10.1142/S0129183113500526.

[54] Zhu, Q.; Oganov, A.R.; Lyakhov, A.O. (2013): Novel stable compounds in the Mg-O system under high pressure. *PCCP, 15 (20)*, 7696–7700, doi: 10.1039/C3CP50678A.

[55] Labidi, S.; Zeroual, J.; Labidi, M.; Klaa, K.; Bensalem, R. (2016): Structural Electronic and Optical Properties of MgO, CaO and SrO Binary Compounds: Comparison Study. *SSP, 257*, 123–126, doi: 10.4028/www.scientific.net/SSP.257.123.

[56] Whited, R.C. & Walker, W.C. (1969): Exciton Spectra of CaO and MgO. *Phys. Rev. Lett., 22 (26)*, 1428–1430, doi: 10.1103/PhysRevLett.22.1428.

[57] Eremets, M.I.; Struzhkin, V.V.; Timofeev, J.A.; Trojan, I.A. *et al.* (1992): Refractive index of diamond under pressure. *High Pressure Res., 9 (1-6)*, 347–350, doi: 10.1080/08957959208245659.

[58] Roessler, D.M. & Walker, W.C. (1967): Electronic spectrum and ultraviolet optical properties of crystalline MgO. *Phys. Rev., 159 (3)*, 733–738, doi: 10.1103/PhysRev.159.733.

[59] Heo, S.; Cho, E.; Lee, H.-I.; Park, G.S. *et al.* (2015): Band gap and defect states of MgO thin films investigated using reflection electron energy loss spectroscopy. *AIP Adv., 5 (7)*, 77167, doi: 10.1063/1.4927547.

[60] Tanaka, K. (1980): Optical properties and photoinduced changes in amorphous As-S films. *Thin Solid Films, 66 (3)*, 271–279, doi: 10.1016/0040-6090(80)90381-8.

[61] Alsaad, A.M.; Al-Bataineh, Q.M.; Ahmad, A.A.; Albataineh, Z.; Telfah, A. (2020): Optical band gap and refractive index dispersion parameters of boron-doped ZnO thin films: A novel derived mathematical model from the experimental transmission spectra. *Optik, 211*, 164641, doi: 10.1016/j.ijleo.2020.164641.

[62] Studenyak, I.P.; Bereznyuk, S.M.; Pop, M.M.; Studenyak, V.I. *et al.* (2020): Influence of cation substitution on optical constants of $(Cu_{1-x}Ag_x)_7SiS5I$ mixed crystals. *SPQEO, 23 (2)*, 186–192, doi: 10.15407/spqeo23.02.186.

[63] Winkler, B. & Milman, V. (2014): Density functional theory based calculations for high pressure research. *Z. Kristallogr. - Cryst. Mater., 229 (2)*, doi: 10.1515/zkri-2013-1650.

[64] Hirose, K.; Sata, N.; Komabayashi, T.; Ohishi, Y. (2008): Simultaneous volume measurements of Au and MgO to 140GPa and thermal equation of state of Au based on the MgO pressure scale. *Phys. Earth Planet. Inter., 167 (3-4)*, 149–154, doi: 10.1016/j.pepi.2008.03.002.

Chapter 3

Reduced charge transfer in mixed-spin ferropericlase inferred from its high-pressure refractive index

Submitted to:

American Mineralogist on 16th June 2023

Reduced charge transfer in mixed-spin ferropericlase inferred from its high-pressure refractive index

Lukas Schifferle[1,2], Sergio Speziale[1]; Björn Winkler[3], Victor Milman[4], Sergey S. Lobanov[1,2*]

[1] *GFZ German Research Center for Geosciences, Telegrafenberg, 14473 Potsdam, Germany*

[2] *Institute of Geosciences, University of Potsdam, Karl-Liebknecht-Straße 24-25, 14476 Potsdam, Germany*

[3] *Institute for Geosciences, Goethe-University Frankfurt, Altenhöferallee 1, 60438 Frankfurt am Main, Germany*

[4] *Dassault Systèmes BIOVIA, 334 Science Park, Cambridge CB4 0WN, United Kingdom*

(Original version submitted on: 16th June 2023)

Physical properties of mantle minerals are essential for comprehensive geodynamic modelling. High-pressure experiments allow measurements of physical properties but fundamental insights into their evolution with pressure are often experimentally inaccessible. Here we report the first in-situ experimental determination of the optical refractive index, its wavelength-dispersion, and optical absorption coefficient of ferropericlase up to ~140 GPa at room temperature. All these properties change gradually in dominantly high-spin (below ~50 GPa) and low-spin (above ~80 GPa) ferropericlase. In the mixed-spin state, however, the index dispersion and the absorption coefficient decrease by a factor of three and ~30%, respectively. These anomalies suggest that charge transport by small polaron is reduced in ferropericlase containing both high- and low-spin iron, providing fundamental insights into the factor-of-three lower electrical conductivity of ferropericlase at ~50-70 GPa.

Author contributions: Main conceptualization of the study by Lobanov, supported by Speziale. High-pressure experiments were performed by **Schifferle** and Lobanov. Density functional theory calculations were provided by Winkler and Milman. Data analysis and interpretation was done by **Schifferle** and Lobanov with assistance of Speziale. **Schifferle** wrote the original draft. All authors contributed to the reviewing and editing of the manuscript.

3.1 Introduction

Physical properties of the Earth's mantle and core are at the center of our understanding of planetary evolution. For example, if the electrical conductivity of the lowermost mantle is sufficiently high, the conducting core and the mantle may exchange angular momentum producing detectable intradecadal signals in the length of day [1; 2] or imposing preferred paths of geomagnetic reversals [3; 4]. Furthermore, the mantle acts as a filter on the magnetic field of the core; thus, knowledge of the electrical conductivity of the mantle is needed to decipher the dynamo history from the geomagnetic record [5–7]. Ferropericlase (Fp), being the second most abundant mineral in the lower mantle and the dominant host of iron [8; 9], likely governs the bulk electrical conductivity of that region. Accordingly, the electrical conductivity of Fp has been the subject of many experimental and theoretical investigations.

Earlier experimental measurements of electrical conductivity at pressures below ~30 GPa have established that the conductivity of Fp is very sensitive to its overall iron content [10; 11]. Perhaps even more importantly, pressure (*P*), temperature (*T*), and oxygen fugacity, all of which vary in the mantle with depth, affect the conductivity of Fp [12; 13]. Two different charge transfer mechanisms have been identified in Fp. At $T <$ ~1000 K, the activation energies and the dependence of electrical conductivity on the Fe^{3+}/Fe_{total} ratio indicate that the dominant conduction mechanism is the electron hopping between Fe^{2+} and Fe^{3+} (small polaron) [10; 14]. At mantle temperatures ($T >$ ~1000 K), however, the extant experimental data are consistent with the mechanism that involves Fe-O charge transfer (large polaron) [10]. Subsequent measurements to ~100 GPa found that the room-temperature conductivity of Fp increases by a factor of ~10 upon compression to 50 GPa, drops by a factor ~3 at 50-70 GPa, and then either increases upon further compression [15] or is almost insensitive to pressure [16]. The factor-of-three drop in room-temperature electrical conductivity at 50-70 GPa is concomitant with the iron high-to-low spin transition in Fp [15; 17] and has been attributed to the decreased mobility and/or density of charge carriers (small polaron) in low-spin Fp [15; 16]. Optical studies indirectly support this conclusion as the overall absorbance in the visible range, which is a measure of high-frequency electronic conductivity, decreases with pressure in low-spin Fp [18–20]. This decrease in absorbance, however, is somewhat questionable because of the unknown sample thickness at high pressure, which is also expected to decrease with pressure in a strongly non-isotropic fashion [21]. Reliable in-situ measurements of sample thickness are thus needed to quantify the absorption coefficient of Fp at high pressure and to resolve whether the electrical conductivity of Fp is linked to its optical properties.

The thickness of (semi)transparent samples in diamond anvil cell (DAC) experiments can be accurately measured if the refractive index of the sample is known. The refractive index and its wavelength-dispersion also provide information on the electronic structure of materials. Pressure-induced changes in the electronic conductivity (e.g., due to small polarons) may thus be accompanied by changes in the refractive index. To the best of our knowledge, the refractive index of ferropericlase at elevated pressures has never been characterized. Recently, we developed a method to measure the refractive index and its wavelength-dependence of fully transparent solids compressed in a DAC to pressures greater than 100 GPa [22; 23]. In the present work, we build up on that method to make it applicable for semitransparent samples and report the

refractive index of high spin (HS), mixed spin (MS), and low spin (LS) ferropericlase. Our results show that the refractive index of Fp in the visible spectral range is largely independent of pressure or iron spin state. The wavelength-dispersion of the refractive index is also nearly invariant in the HS and LS Fp but is reduced abruptly by a factor of three in the MS state. The absorption coefficient also decreases by ~35% at the onset of the spin transition. Our observations allow an alternative interpretation of the previous high-pressure electrical conductivity data. We suggest that the mobility and/or density of small polarons is reduced only in the MS regime, unlike previous studies that proposed reduced small polaron transport in LS Fp.

3.2 Experimental methods

3.2.1 Samples and diamond anvil cell loading

All high-pressure experiments were performed using symmetrical DACs equipped with diamond pairs featuring beveled 300/100 μm or flat 300 μm culets. A rhenium gasket indented to a thickness of 15-20 μm was laser-drilled to create cylindrical holes with diameters of ~45 μm (when 300/100 μm culets were used) or ~140 μm (when 300 μm culets were used), which served as sample chambers. For each loading we selected fragments of the samples with appropriate dimensions to fill the DAC sample chamber, placed the samples without any pressure-transmitting medium, immediately sealed the DAC assembly and increased the pressure to ~20-30 GPa producing optically homogenous samples, which is required for refractive index measurements described below. We used synthetic ferropericlase samples of two different compositions: $(Mg_{0.87}Fe_{0.13})O$ and $(Mg_{0.76}Fe_{0.24})O$, further referred to as Fp13 and Fp24 to indicate their iron content. Fp13 was produced by Fe diffusion into an MgO crystal in a gas-mixing furnace at ambient pressure [24]. Fp24 was synthesized by Caterina Melai [25] in a 10/5 multi-anvil assembly at 15 GPa and 1800 °C using starting material from Longo et al. [26]. Electron energy loss spectroscopy yielded an $Fe^{3+}/\sum Fe_{total}$ ratio of ~0.1 for Fp13 [24], however, its Fe^{3+} content might be considerably lower as discussed in Schifferle & Lobanov [20]. The $Fe^{3+}/\sum Fe_{total}$ ratio of Fp24 is ~0.02, based on Mössbauer spectroscopy measurements [25].

3.2.2 Refractive index measurements

Because of significant light attenuation in Fp13 and Fp24 over thicknesses characteristic of samples in DAC, we needed to extend the reflectivity method used previously to study transparent samples [22; 23; 27; 28] to semi-transparent (absorbing) samples. The approach is based on the Fresnel equation for normal incidence, where the measured reflectivity of the diamond-sample interface ($R_{dia\text{-}smp}$) is related to the refractive index n of the sample (n_{smp}) and diamond (n_{dia}), and the imaginary part of the refractive index of the sample ($\varkappa_{smp}$):

$$R_{dia-smp} = \frac{(n_{smp}-n_{dia})^2+\kappa_{smp}{}^2}{(n_{smp}+n_{dia})^2+\kappa_{smp}{}^2} \quad \text{(Eq. 3.1)}$$

Previous reports on the absorption coefficient of ferropericlase indicate that for Fp13 and Fp24 $\varkappa_{smp}$ is small (~0.01 for the studied pressure range, see **Appendix B** for further details) and can thus be considered zero.

Nonetheless, quantifying light attenuation in ferropericlase due to absorption is necessary for the determination of $R_{dia\text{-}smp}$:

$$\frac{I_1+I_2}{I_0} = R_{dia-smp} + T^2(R_{dia-smp}{}^3 - 2R_{dia-smp}{}^2 + R_{dia-smp}) \quad \text{(Eq. 3.2)},$$

where I_0, I_1, and I_2 are individual reflections defined graphically in **Figure 2-1 A**. T is sample transmission ($T = 0$ for opaque and $T = 1$ for transparent samples). We independently express T through I_T/I_{noDAC}:

$$\frac{I_T}{I_{noDAC}} = T(R_{dia-smp}{}^2 - 2R_{dia-smp} + 1)(1 - R_{dia-air})^2 \quad \text{(Eq. 3.3)}$$

where I_T and I_{noDAC} are the signals measured through the sample and without the DAC and $R_{dia\text{-}air}$ is the reflectivity of the diamond-air interface. The derivations of Eq. 3.2 and 3.3 are provided in the supplementary materials (**Appendix B**). All measured signals were averaged over the 550-650 nm spectral range, where the reflectivity of the reference mirror is well-characterized (~0.985-0.995), allowing for precise measurements of the probe intensity impinging on the upstream diamond-air interface. Eq. 3.2 and 3.) contain only two unknowns ($R_{dia\text{-}smp}$ and T) and are solved simultaneously. Two of the three sets of roots included imaginary $R_{dia\text{-}smp}$ and T and were discarded. Using $R_{dia\text{-}smp}$ from the real set of roots, we solve Eq. 3.1 for n_{smp}, the refractive index of ferropericlase at 600 nm (because of the averaging of $\frac{I_1+I_2}{I_0}$ and T over 550-650 nm). In solving Eq. 3.1, we assume a pressure-independent refractive index of diamond (n_{dia} = 2.418 [29]). The validity of this assumption and possible effects of a pressure dependence of n_{dia} have been discussed in detail by Schifferle et al. [23]. Their results on MgO support the hypothesis n_{dia} = *constant*. However, we provide all necessary data for the evaluation of n_{smp} in **Appendix Table B 1** which can be reanalyzed when more detailed information on the pressure dependence of n_{dia} is available. The solutions to Eq. 3.1-3.3 have been found with Python SciPy and SymPy libraries [30; 31]. We independently tested the reflectivity method for semitransparent samples developed in this work by reproducing the high-pressure evolution of the refractive index of an Fe-bearing basaltic glass (i.e., absorbing in the visible) reported by Kuryaeva & Kirkinskii [32].

We also measured the refractive index of Fp13 decompressed to 1 atm after one of the DAC runs. To this end, we removed the upper diamond anvil to ensure no pressure was applied to the sample and measured the reflectivity of the air-sample interface where $I_{air-smp}$ is composed of I_1* and I_2*, which are individual reflections from the air-sample and sample-diamond interfaces (**Figure 2-1 B**). The normalized reflectance spectrum was analyzed for the average spectral separation of the interference fringes to obtain the optical path ($OP = n_{1atm}d_{1atm}$) (**Figure 2-1 C**). A radial cross-section through the retrieved sample (**Figure 2-1, D**) created by a focused ion beam allowed to directly measure the thickness of decompressed ferropericlase at the center of the DAC sample cavity (d_{1atm}) and to obtain the refractive index of Fp13 as $n_{1\,atm} = \frac{OP}{d_{1atm}}$.

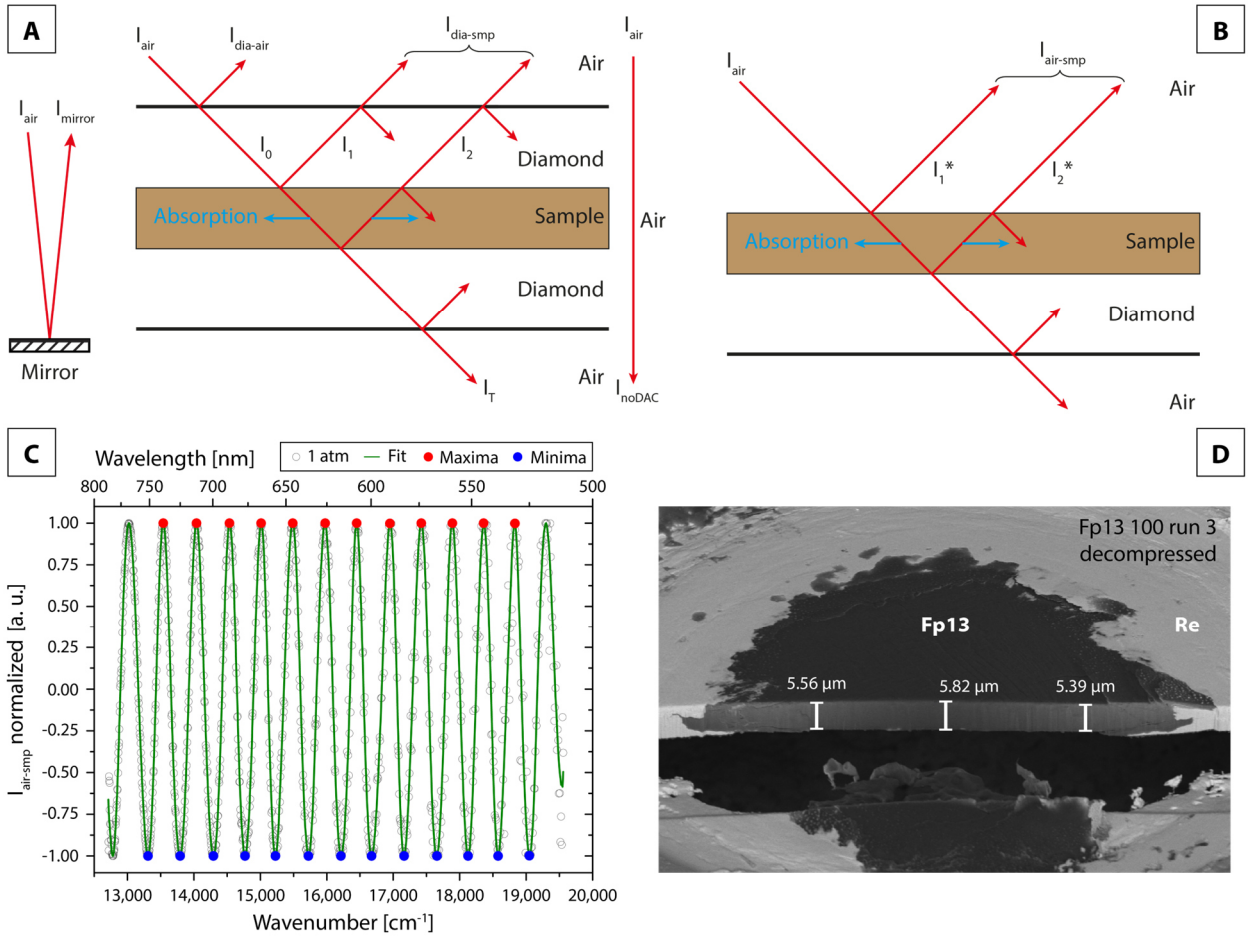

Figure 3-1 A: Reflectivity measurements in a partially absorbing sample at high-pressure conditions. The perpendicularly-incident probe laser is partially reflected at the air-mirror, diamond-air and diamond-sample interfaces. Oblique probe incidence is depicted for clarity. **B**: Reflectivity measurements for the decompressed sample in an opened diamond anvil cell. **C**: A normalized intensity spectrum of Fp13 (run 3) decompressed to 1 atm. The local extrema (blue and red circles) served to find the optical path ($n_{1atm}d_{1atm}$), where d_{1atm} is sample thickness. **D**: A secondary electron microscope image of a focused ion beam cross-section of the of Fp13 (run 3) decompressed to 1 atm used to directly image the sample thickness. The light grey part is the Re gasket and dark grey is Fp13.

3.2.3 Dispersion analysis

The interference fringe spectra can be analyzed for the wavelength-dispersion of the refractive index following Schifferle et al. [23] (for more details, see their section 2.3). Briefly, for each extremum the interference condition is:

$$\lambda k(\lambda) = 2dn_{smp}(\lambda) \quad \text{(Eq. 3.4)},$$

where $k(\lambda)$, is the interference order number of the minimum/maximum (half-integer step size) observed at the wavelength λ, d is sample thickness at high pressure, and $n_{smp}(\lambda)$ is the refractive index at the extremum. Using Eq. 3.4 for each pair of extrema we estimated sample thickness assuming n_{smp} is wavelength independent, which is accurate within ~1% for Fe-poor Fp because the index dispersion of MgO across the studied spectral range is small (~1%) [33]. We will provide evidence below that the index dispersion of Fp13 is indeed comparable to MgO. The sample thickness averaged over all used extrema pairs is then used to assign the interference order number to the extremum closest to 600 nm (e.g., k_{600nm} = 70 at 16.9 GPa,

k_{600nm} = 41.5 at 109.1 GPa) and subsequently to all the other observed extrema. Finally, the refractive index at each λ is calculated using Eq. 3.4 for all the observed extrema. The propagation of random and systematic relative errors in the measured index dispersion yields overall errors of ~0.9% at ~23 GPa and ~2.6% at ~109 GPa. The increase in this error is likely due to diamond cupping at high pressure [23].

3.2.4 Computation of refractive index and index dispersion for MgO and ferropericlase

Atomistic model calculations were carried out within the framework of DFT [34] and the pseudopotential method using the CASTEP simulation package [35]. Ultrasoft pseudopotentials were generated "on the fly" using the parameters provided with the CASTEP distribution. These pseudopotentials have been extensively tested for accuracy and transferability [36]. The pseudopotentials were employed in conjunction with plane waves up to a kinetic energy cutoff of 630 eV [37]. The spin-polarized calculations were carried out with the PBE exchange-correlation functional and a Hubbard U of 2.5 eV for the Fe-*d*-states. Monkhorst-Pack grids [38] were used for Brillouin zone integrations with a distance of < 0.025 $Å^{-1}$ between grid points. Convergence criteria included an energy change of < 5×10^{-6} eV/atom, a maximal force of < 0.01 eV/Å, and a maximal deviation of the stress tensor < 0.02 GPa from the imposed stress tensor. It should be stressed that all calculations were carried out in the athermal limit, i.e., the influence of temperature and zero-point motion were not taken into account.

3.3 Results and discussion

The refractive indices of Fp13 and Fp24 measured in this work are shown in **Figure 3-2**. At all pressures, the index of Fp24 at 600 nm is ~1-2% higher than that of Fp13, consistent with the results of Henning et al. [39] who measured the optical properties of $Fe_xMg_{1-x}O$ (x = 0.4-1) at 1 atm. The indices of both Fp13 and Fp24 increase with pressure with no sharp discontinuity over the expected spin transition range of 40-80 GPa [17; 40; 41]. In one of the runs (Fp13, run3), the index measured at 600 nm appears ~1% too low than what may be expected from its value independently measured at 1 atm as well as expected from the results of Henning et al. [39]. It is plausible that submicron impurities are present in that loading which contributed an up-shift to the measured $\frac{I_1+I_2}{I_0}$ through light back scattering, increasing the apparent $R_{dia\text{-}smp}$ and thus decreasing n_{smp}. This is indirectly supported by our data on Fp24, which remained fully opaque upon compression, in which case the evaluation of $R_{dia\text{-}smp}$ is more accurate because only the upstream diamond-sample reflection (I_1) contributes to $\frac{I_1+I_2}{I_0}$ at T = 0 (see Eq. 3.2). At P > 60 GPa, the increase in refractive indices of Fp13 (+0.0014 ($\pm1.31\times10^{-3}$) per 10 GPa) and Fp24 (+0.0021 ($\pm7.75\times10^{-4}$) per 10 GPa) is small, but resolvable within the uncertainty of our determination; the refractive index of mantle-like Fp is not independent of pressure (dashed lines in **Figure 3-2**). The extrapolation of the high-pressure index of Fp24 at 600 nm to 1 atm is in excellent agreement with the expectation from the literature [39].

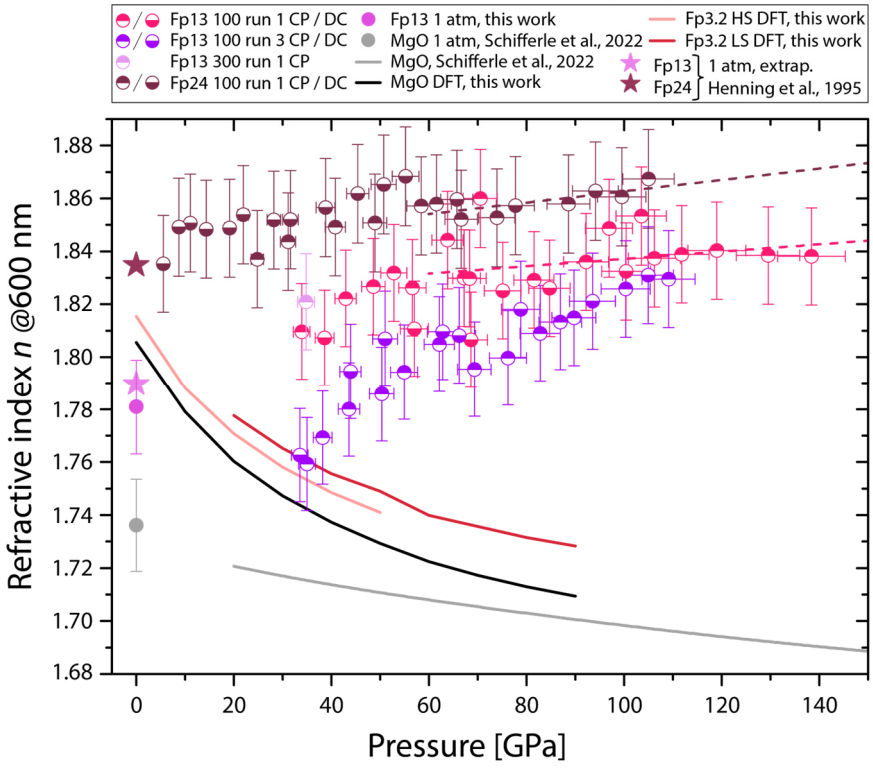

Figure 3-2 The refractive index of Fp13 and Fp24 at 600 nm measured in this work, compared to DFT calculations of Fp3.2 (high- and low-spin) and MgO, as well as experimental data on MgO from Schifferle et al. [23]. Stars represent extrapolations based on the indices.

The refractive index of ferropericlase is considerably higher than that of MgO (**Figure 3-2**) because of the higher polarizability of Fe^{2+} compared to Mg^{2+} at 1 atm ($^{[6]}Fe^{2+}$ 2.040 Å^3, $^{[6]}Mg^{2+}$ 0.651 Å^3 [42]). This results in a compositional dependence of the refractive index of ferropericlase (higher Fe content leads to higher index, **Appendix Figure B 1**). Interestingly, while the pressure-derivatives of the indices of Fp13 and Fp24 are positive, that of MgO is negative [23; 43–45]. The increase in refractive index with pressure entails that the Lorenz-Lorentz factor ($\frac{n^2-1}{n^2+2} \propto \frac{\rho}{\alpha_{LL}}$) also increases with pressure (ρ is density, α_{LL} is Lorenz-Lorentz polarizability). Accordingly, we attribute the positive pressure dependence of the refractive index of ferropericlase to its anomalous polarizability because the compressibility of MgO, Fp13, and Fp24 are similar. However, our DFT computations indicate that at low Fe^{2+} concentrations (Fp3.2) the pressure-derivative of the refractive index is similar to that of MgO (see black and grey lines in **Figure 3-2**). We note that Fe-Fe interactions, which are very weak or absent in our DFT computations as the Fe-Fe-distances are large (1 Fe, 31 Mg atoms in the supercell), are likely present in Fp13 and Fp24 because their Fe content exceeds the percolation limit (12%, Lorenz & Ziff [46]). Above the percolation limit, an interconnected network of overlapping t_{2g} orbitals between adjacent edge-sharing FeO_6 octahedra is present. We propose that pressure-induced electron delocalization along the interatomic t_{2g}-t_{2g} joints [47] maintains higher polarizability in Fp and is thus the reason for the anomalous positive pressure dependence of the refractive indices of HS Fp13 and Fp24. Such electron delocalization is complete in the LS state; hence, the refractive index of LS Fp is almost pressure independent (i.e., MgO-like).

We used the high-pressure refractive index and the interferometric data to obtain d, the thickness of ferropericlase at high pressure. To avoid fluctuations in d due to the apparently random error in the index, n is derived from a linear P vs. n fit (see Appendix B). Next, we quantify the absorption coefficient of ferropericlase as: $\alpha(600\ nm) = A \cdot \ln(10)/d$, where $A = -log_{10}T$ is the measured optical absorbance of the sample. Please note that even at low pressure (< 30 GPa) transmission data and the interference fringe pattern quality were sufficient to obtain accurate thicknesses (the variation in optical path inferred for different fringes is less than 1%) and absorption coefficients (3% error). Due to the high absorption coefficient of Fp24, transmission could only be detected in very thin samples (< 6 μm), achieved only on decompression as samples in DACs continue to thin upon pressure release [21]. Here we extended this seemingly general behavior to ferropericlase (**Appendix Figure B 2**), and show that thickness estimations based on the assumption of isotropic compression severely overestimate the real sample thickness by up to ~50%, similar to the conclusion of Lobanov & Geballe [21].

For Fp13 we find α (600 nm) to increase from 20 GPa up to ~57 GPa by a factor of ~3, where the maximum is reached at ~2000 cm^{-1} (**Figure 3-3**). For the pressure range > 57 to ~85 GPa we find a sharp decrease in α(600 nm) by ~30%. At P > 85 GPa, the absorption coefficient reaches a plateau at ~1300 cm^{-1}. The pressure range of the negative $d\alpha/dP$ suggests that the decrease of α is related to the spin transition in Fp13 [20]. In HS Fp, the transition energy of the single multiplicity allowed crystal field (*d-d*) band ($^5T_{2g} \rightarrow {}^5E_g$) is almost pressure independent [19; 20]; thus, this band does not contribute to the increase in the absorption coefficient up to 60 GPa. One of the *d-d* bands of LS Fp appears close to 600 nm (16,667 cm^{-1}) at ~60 GPa [20] and would only increase the absorption coefficient, in contrast to what is observed. At the same time, the absorption edge shows a qualitative red-shift (in HS) and blue-shift (in LS) with pressure [18–20]. We conclude, therefore, that the trend in α(600 nm) is mostly related to the intensity of the UV-absorption edge in ferropericlase with a minor contribution of the crystal field bands.

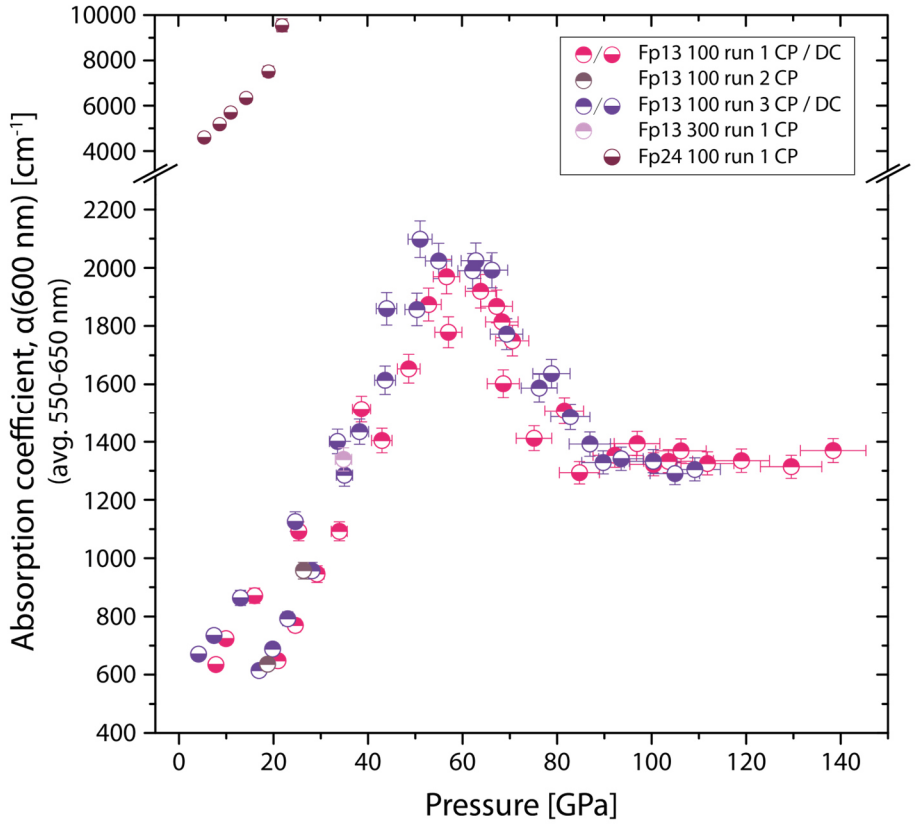

Figure 3-3 Absorption coefficients of Fp13 and Fp24 at 600 nm based on direct measurements of the optical path ($n_{smp}d$). Thicknesses used for the calculation of the absorption coefficient are obtained by dividing the optical path by n_{smp} at 600 nm and neglecting the index dispersion in the analyzed spectral range (~500-800 nm) which is ~1% or less (see discussion in the main text). The uncertainty in d is that of refractive index and is ~1%. Please note the break in y-axis. Abbreviations: CP = compression, DC = decompression.

The variation of α(600 nm) with pressure is reversible upon decompression down to ~40 GPa. Our α(600 nm) allows to derive the wavelength-dependent absorption coefficients (and thus the imaginary part of the refractive index) from previously published absorbance data for the same Fp13 sample [20] (**Appendix Figure B 4**). Compared to previous reports on the absorption coefficient of ferropericlase where the sample thickness at high pressure was estimated using its equation of state [48], we show that a is lower by up to ~50%. This is because Lobanov et al. [48] measured the thickness of their Fp13 sample after decompression and assumed the sample was thinner at high pressure. As shown by Lobanov & Geballe [21] samples in DACs continue to thin upon decompression; and their data can be used to revise the Fp13 absorption coefficients reported in Lobanov et al. [48]. An approximate correction suggests that the radiative thermal conductivity of ferropericlase at the base of the mantle has been underestimated by roughly a factor of two in that previous study.

Concomitantly to the directly measured decrease in the absorption coefficient by ~30% at 57-85 GPa, we observe a sharp decrease in the absolute wavelength dispersion of the refractive index of Fp13 (**Figure 3-4**). Below ~40 GPa, the wavelength-dispersion of the refractive index of Fp13 is essentially pressure independent. At P = 43.6-69.3 GPa, however, the index dispersion is dramatically decreased by a factor of ~3 from ~0.0174 (± ~1%) to 0.006 (± ~2%) (orange line, **Figure 3-4, A**). Yet, at P > 69.3 GPa, the absolute index

dispersion is almost restored at ~0.016 (± 1%) (**Figure 3-4, B**). The index dispersion is ~50% stronger in HS and LS Fp13 than in MgO, which is qualitatively consistent with our DFT computations that produced ~20% higher dispersion in the case of Fp3.2 than in the case of pure MgO. Likewise, our computations support the notion that the index dispersion in HS and LS Fp3.2 are similar. In contrast to pure HS and LS ferropericlase probed in experiments and computations, the measured index dispersion of MS Fp13 is anomalously low: ~50% lower than that of MgO at 60-80 GPa. We note, that the dispersion data is analyzed assuming a constant refractive index at 600 nm of 1.79 (based on the expectation for Fp13 at 1 atm [39] to better account for deviations due to random errors in the refractive index. This, however, does not significantly affect the inferred index dispersion, because possible differences in refractive index at 600 nm of 2-3% result mostly in a vertical shift of the index spectra and not its slope (**Figure 3-4 A**).

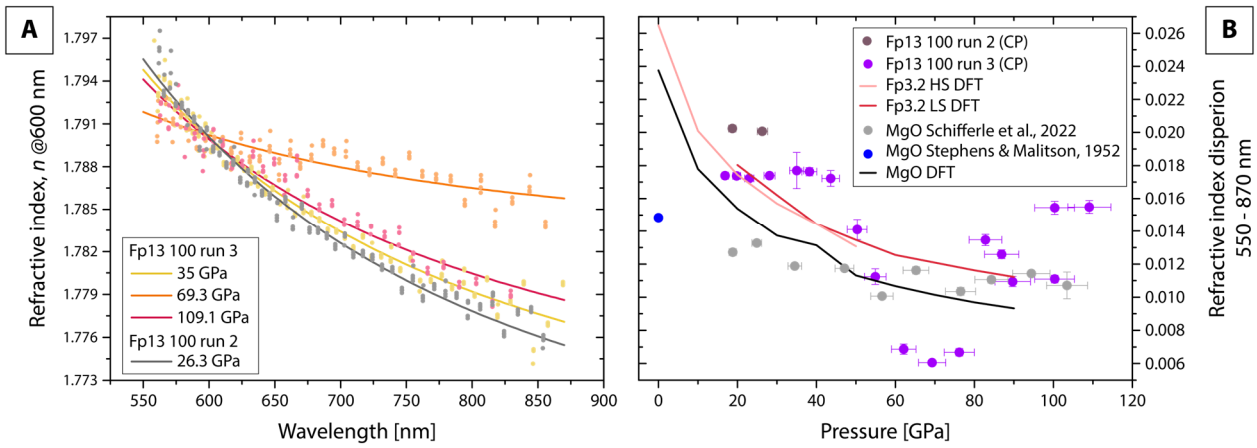

Figure 3-4 (**A**) Dispersion of the refractive index of Fp13 (compression) at selected pressures (assuming a pressure-independent refractive index *n*(600 nm) of 1.79) and (**B**) as the difference between refractive indices at 550 and 870 nm compared to DFT calculations for Fp3.2 and MgO as well as previously published experimental data [23; 33].

We analyzed the dispersion by the single-effective-oscillator model of Wemple & DiDomenico [49]. In this model, the wavelength dependence of the refractive index is related to two fitting parameters E_0 and E_d, which describe the single oscillator energy and dispersion energy (in eV), respectively. These quantities are related to the band gap width and bonding environment:

$$n(\lambda) = \sqrt{\frac{E_d \cdot E_0}{E_0^2 - \left(\frac{h \cdot c}{\lambda}\right)^2} + 1} \qquad \text{(Eq. 3.5)}$$

Here, h is the Planck's constant in eV·s and c the speed of light in m/s and λ the wavelength in m. By fitting Eq. 3.5 to the measured index dispersion at 550-870 nm, we find E_d and E_0. An in-detail description of the procedure and instrumental setup can be found in Schifferle et al. [23].

Wemple & DiDomenico [49] proposed that E_0 is related to the average optical band gap, and that the ratio $E_0/1.5$ approximates independently measured band gaps. The denominator in this ratio, however, is material dependent. To estimate it for Fp13 we performed a Tauc plot analysis of the low-pressure optical absorption data of Fp13 reported in Schifferle & Lobanov [20], which yields the minimum band gap energy of 2.75 eV. We thus divide all fitted E_0 by 3.8 to match 2.75 eV at low pressure (i.e. at $P <$ ~40 GPa, where the

wavelength-dispersion is essentially pressure-independent). Although the values of $E_0/3.8$ at $P < 40$ GPa are broadly consistent with previous DFT calculations [50–54], our results likely underestimate the band gap as broad-range UV spectra are not available. Despite these uncertainties, we can derive semi-quantitative trends in band gap energy.

In **Figure 3-5** we show $E_0/3.8$ and $E_d/7.6$ (for illustration only, i.e., to scale E_d close to $E_0/3.8$) of Fp13 from the Wemple & DiDomenico [49] single-effective oscillator analysis and compare it with existing computations of the optical band gap in ferropericlase. Regardless of the chosen scaling factor for E_0, our experimental data (**Figure 3-5**) suggests a constant band gap energy up to ~40 GPa. In the MS state ($P \approx$ 50-80 GPa), we observe an increase in $E_0/3.8$ with a maximum at ~69.3 GPa of ~4.7 eV. This peak in the band gap probably represents 50% HS and 50% LS, consistent with the LS fraction inferred by Mössbauer spectroscopy [40]. At $P >$ 100 GPa, the band gap energy is comparable to that at $P <$ 40 GPa. These semi-quantitative insights into the band gap energy are consistent with DFT computations [53; 54], which suggest a pressure-independent band gap energy for high- and low-spin states. The possible intermediate spin (IS) state, although energetically disfavored [51], also does not deviate from the general trend of a near-constant band gap in DFT calculations. However, to the best of our knowledge, there are no DFT computations of the MS state available, which we probed optically here for the first time. E_d shows a trend qualitatively similar to that of E_0. Because E_d represents the distribution of charge around the anion [49], its increase and decrease over the spin transition might reflect the decrease/increase in *p-d* orbital overlap. For example, charge donation from oxygen to the empty e_g orbitals in the LS state has been inferred from the decrease in the Fe-O bond covalency [20]. A similar ligand-to-Fe donation has been proposed as a consequence of the Fe^{2+} HS to LS transition in S- and Sn-thiospinels [55].

The increase in $E_0/3.8$ by ~1.95 eV and the reduction of the absorption coefficient by ~35% over the spin transition range offers a qualitative understanding of the previously reported drop of electrical conductivity by a factor of up to three in ferropericlase at ~50-70 GPa [15; 16]. In contrast to these previous studies, where a lower small polaron mobility and/or density in LS ferropericlase was proposed as an explanation [15; 16], our data suggests that lower electron mobility is characteristic of the MS state while that in HS and LS is similar. We propose that qualitatively this can be understood in terms of small polaron transport through the crystal lattice, which requires electron exchange between adjacent Fe sites: $Fe^{2+} \xrightarrow{e^-} Fe^{2+} = Fe^{3+} + Fe^{+}$. In particular, the absorption coefficient of Fp may be strongly enhanced due to magnetic coupling between adjacent iron sites, which offers an efficient means of relaxing the spectroscopic selection rules, as has been shown for Fe^{3+}-O_6 octahedra [57]. Considering that magnetic collapse is a defining characteristic of LS Fe^{2+} [58], the magnetic relaxation of spectroscopic selection rules is only possible in HS-HS pairs. The collapse of magnetic moments of individual Fe atoms in the MS and LS states is thus a viable explanation for the ~30% decrease of the absorption coefficients at $P >$ 57 GPa. This mechanism, however, does not offer an explanation for the relatively high refractive index dispersion of the LS Fp.

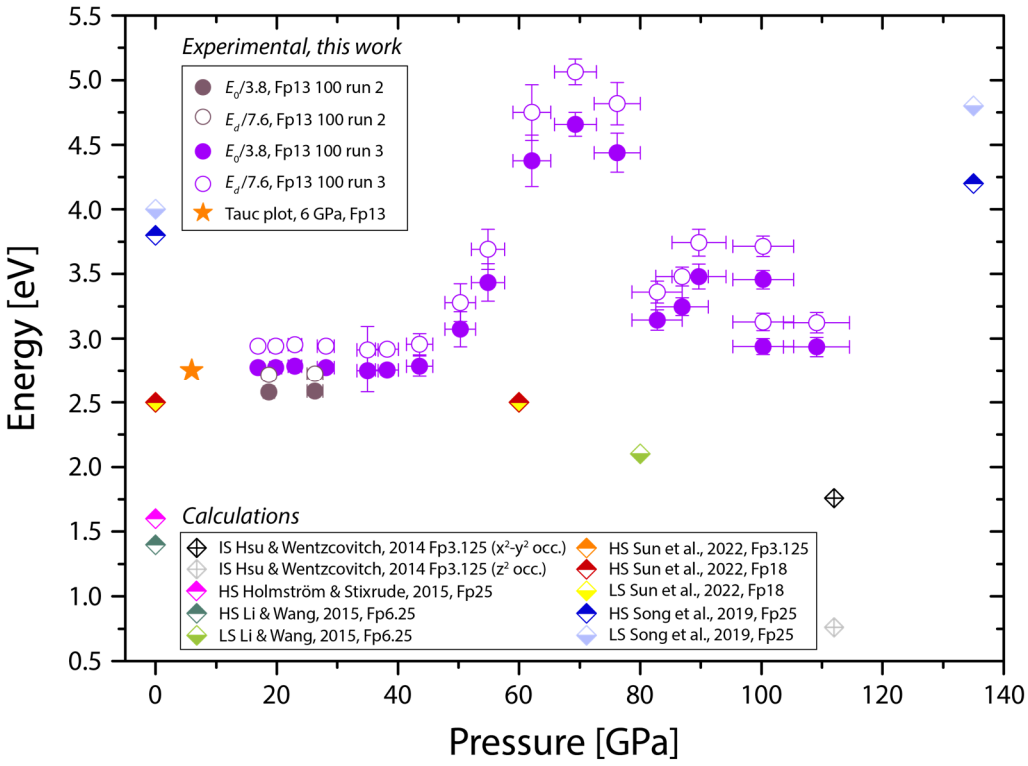

Figure 3-5 Results of the Wemple & DiDomenico [49] fit (E_0/3.8 and E_d/7.6) to the measured index dispersion of Fp13 (circles). Orange star represents the band gap estimation based on Tauc plot analysis [56] of data from [20]. In addition, we show calculations from literature for the band gap in different ferropericlase compositions and spin configurations (diamonds). Abbreviations: high-spin (HS), intermediate-spin (IS) and low-spin (LS). Please note, datapoints from Sun et al. [54] are directly overlapping at 0 GPa and 2.5 eV (HS Fp 3.125, HS Fp18 and LS Fp18) as well as at 60 GPa and 2.5 eV (HS Fp18, LS Fp18).

3.4 Implications

A strong reduction of the electrical conductivity of MS ferropericlase opens a new scenario for the overall conductivity of the lowermost mantle. Ab initio computations indicate that ferropericlase is predominantly in the mixed spin state at depths greater than ~1900 km and down to the core-mantle boundary at ~2900 km because of the high temperatures of the lower mantle, which broaden the mixed spin pressure range [50]. If the drop in electrical conductivity at ~50-70 GPa is due to the lower small polaron mobility/density in LS Fp as proposed by Lin et al. [15] and Ohta et al. [16], then one expects only a moderate drop in mantle conductivity if any at depths >1900 km, because LS Fp is never dominant even at the base of the mantle. In contrast, if the drop in Fp conductivity is indeed characteristic of the MS state (as inferred in this work), then one expects a significant reduction of mantle electrical conductivity over the lowermost 1000 km of the mantle. The magnetic data recorded by SWARM, which is a low-orbit satellite mission dedicated to the study of Earth's magnetic field, now allows 3D mapping the conductivity of the Earth's mantle down to ~2000 km depth [59; 60]. Deeper conductivity models will be enabled by the continuing geomagnetic observations and may thus be sensitive to the changes in conductivity due to the spin crossover in ferropericlase. Yet another alternative is that small polaron is a relatively unimportant mechanism in the lower mantle

because of the crossover to the large polaron mechanism at $T > \sim 1000$ K, as suggested by earlier studies at $P < \sim 30$ GPa [10; 12]. A transition to a band conduction mechanism in Fp at $T > \sim 2000$ K has been proposed by theoretical computations [61], consistent with the results of optical experiments at high *P-T* that indicate a crossover to opaque Fp at 2500 K [48]. Direct measurements of Fp electrical conductivity at realistic lower mantle *P-T* conditions are thus needed to improve our understanding of lower mantle conductivity.

3.5 References

[1] Duan, P. & Huang, C. (2020): Intradecadal variations in length of day and their correspondence with geomagnetic jerks. *Nat. Commun., 11 (1)*, 2273, doi: 10.1038/s41467-020-16109-8.

[2] Holme, R. & De Viron, O. (2013): Characterization and implications of intradecadal variations in length of day. *Nature, 499 (7457)*, 202–204, doi: 10.1038/nature12282.

[3] Buffett, B.A. (2015): Core–mantle interactions. In: Schubert (Ed.): Treatise on Geophysics, 2nd Ed., 213–224.

[4] Runcorn, S.K. (1992): Polar path in geomagnetic reversals. *Nature, 356 (6371)*, 654–656, doi: 10.1038/356654a0.

[5] Alexandrescu, M.M.; Gibert, D.; Le Mouël, J.-L.; Hulot, G.; Saracco, G. (1999): An estimate of average lower mantle conductivity by wavelet analysis of geomagnetic jerks. *J. Geophys. Res., 104 (B8)*, 17735–17745, doi: 10.1029/1999JB900135.

[6] Bloxham, J. & Jackson, A. (1992): Time-dependent mapping of the magnetic field at the core-mantle boundary. *J. Geophys. Res., 97 (B13)*, 19537, doi: 10.1029/92JB01591.

[7] Constable, S. (2015): Geomagnetic induction studies. In: Schubert (Ed.): Treatise on Geophysics, 2nd Ed., 219–254.

[8] Irifune, T.; Shinmei, T.; McCammon, C.A.; Miyajima, N. *et al.* (2010): Iron partitioning and density changes of pyrolite in Earth's lower mantle. *Science, 327 (5962)*, 193–195, doi: 10.1126/science.1181443.

[9] Piet, H.; Badro, J.; Nabiei, F.; Dennenwaldt, T. *et al.* (2016): Spin and valence dependence of iron partitioning in Earth's deep mantle. *Proc. Natl. Acad. Sci. U.S.A., 113 (40)*, 11127–11130, doi: 10.1073/pnas.1605290113.

[10] Dobson; Richmond; Brodholt (1997): A high-temperature electrical conduction mechanism in the lower mantle phase $(Mg,Fe)_{1-x}O$. *Science, 275 (5307)*, 1779–1781, doi: 10.1126/science.275.5307.1779.

[11] Li, X. & Jeanloz, R. (1990): High pressure-temperature electrical conductivity of magnesiowüstite as a function of iron oxide concentration. *J. Geophys. Res., 95 (B13)*, 21609, doi: 10.1029/JB095iB13p21609.

[12] Dobson, D.P. & Brodholt, J.P. (2000): The electrical conductivity of the lower mantle phase magnesiowüstite at high temperatures and pressures. *J. Geophys. Res., 105 (B1)*, 531–538, doi: 10.1029/1999JB900242.

[13] Wood, B.J. & Nell, J. (1991): High-temperature electrical conductivity of the lower-mantle phase (Mg, Fe)O. *Nature, 351 (6324)*, 309–311, doi: 10.1038/351309a0.

[14] Iyengar, G.N. K. & Alcock, C.B. (1970): A study of semiconduction in dilute magnesio-wüstites. *Philos. Mag. TEAP, 21 (170)*, 293–304, doi: 10.1080/14786437008238418.

[15] Lin, J.-F.; Weir, S.T.; Jackson, D.D.; Evans, W.J. *et al.* (2007): Electrical conductivity of the lower-mantle ferropericlase across the electronic spin transition. *Geophys. Res. Lett., 34 (16)*, doi: 10.1029/2007GL030523.

[16] Ohta, K.; Hirose, K.; Onoda, S.; Shimizu, K. (2007): The effect of iron spin transition on electrical conductivity of (Mg,Fe)O magnesiowüstite. *Proc. Jpn. Acad. Ser. B Phys. Biol. Sci., 83 (3)*, 97–100, doi: 10.2183/pjab.83.97.

[17] Glazyrin, K.; Miyajima, N.; Smith, J.S.; Lee, K.K. M. (2016): Compression of a multiphase mantle assemblage. *J. Geophys. Res.: Solid Earth, 121 (5)*, 3377–3392, doi: 10.1002/2015JB012321.

[18] Goncharov, A.F.; Struzhkin, V.V.; Jacobsen, S.D. (2006): Reduced radiative conductivity of low-spin (Mg,Fe)O in the lower mantle. *Science, 312 (5777)*, 1205–1208, doi: 10.1126/science.1125622.

[19] Keppler, H.; Kantor, I.; Dubrovinsky, L.S. (2007): Optical absorption spectra of ferropericlase to 84 GPa. *Am. Mineral., 92 (2-3)*, 433–436, doi: 10.2138/am.2007.2454.

[20] Schifferle, L. & Lobanov, S.S. (2022): Evolution of chemical bonding and spin-pairing energy in ferropericlase across its spin transition. *ACS Earth Space Chem., 6 (3)*, 788–799, doi: 10.1021/acsearthspacechem.2c00014.

[21] Lobanov, S.S. & Geballe, Z.M. (2022): Non-isotropic contraction and expansion of samples in diamond anvil cells. *Geophys. Res. Lett., 49 (19)*, e2022GL100379, doi: 10.1029/2022GL100379.

[22] Lobanov, S.S.; Speziale, S.; Winkler, B.; Milman, V. *et al.* (2022): Electronic, structural, and mechanical properties of SiO_2 glass at high pressure inferred from its refractive index. *Phys. Rev. Lett., 128 (7)*, 77403, doi: 10.1103/PhysRevLett.128.077403.

[23] Schifferle, L.; Speziale, S.; Lobanov, S.S. (2022): High-pressure evolution of the refractive index of MgO up to 140 GPa. *J. Appl. Phys., 132 (12)*, 125903, doi: 10.1063/5.0106626.

[24] Lobanov, S.S. & Speziale, S. (2019): Radiometric temperature measurements in nongray ferropericlase with pressure- spin- and temperature-dependent optical properties. *J. Geophys. Res.: Solid Earth, 124 (12)*, 12825–12836, doi: 10.1029/2019JB018668.

[25] Aprilis, G.; Pakhomova, A.; Chariton, S.; Khandarkhaeva, S. *et al.* (2020): The effect of pulsed laser heating on the stability of ferropericlase at high pressures. *Minerals, 10 (6)*, 542, doi: 10.3390/min10060542.

[26] Longo, M.; McCammon, C.A.; Jacobsen, S.D. (2011): Microanalysis of the iron oxidation state in (Mg,Fe)O and application to the study of microscale processes. *Contrib. Mineral. Petrol., 162 (6)*, 1249–1257, doi: 10.1007/s00410-011-0649-9.

[27] van Straaten, J. & Silvera, I.F. (1988): Equation of state of solid molecular H_2 and D_2 at 5 K. *Phys. Rev. B Condens. Matter, 37 (4)*, 1989–2000, doi: 10.1103/PhysRevB.37.1989.

[28] Zha, C.-S.; Hemley, R.J.; Gramsch, S.A.; Mao, H.-K.; Bassett, W.A. (2007): Optical study of H_2O ice to 120 GPa. *J. Chem. Phys., 126 (7)*, 74506, doi: 10.1063/1.2463773.

[29] Hynes (2016): CRC Handbook of Chemistry and Physics. 97th ed. Boca Raton, London, New York: CRC Press.

[30] Meurer, A.; Smith, C.P.; Paprocki, M.; Čertík, O. *et al.* (2017): SymPy: symbolic computing in Python. *PeerJ Comput. Sci., 3*, e103, doi: 10.7717/peerj-cs.103.

[31] van der Walt, S.; Colbert, S.C.; Varoquaux, G. (2011): The NumPy array: a structure for efficient numerical computation. *Comput. Sci. Eng., 13 (2)*, 22–30, doi: 10.48550/arXiv.1102.1523.

[32] Kuryaeva, R.G. & Kirkinskii, V.A. (1997): Influence of high pressure on the refractive index and density of tholeiite basalt glass. *Phys. Chem. Minerals., 25*, 48–54.

[33] Stephens, R.E. & Malitson, I.H. (1952): Index of refraction of magnesium oxide. *J. Res. Natl. Bur. Stand., 49 (4)*, 249–252, doi: 10.6028/jres.049.025.

[34] Hohenberg, P. & Kohn, W. (1964): Inhomogeneous electron gas. *Phys. Rev., 136 (3B)*, B864-B871, doi: 10.1103/PhysRev.136.B864.

[35] Clark, S.J.; Segall, M.D.; Pickard, C.J.; Hasnip, P.J. *et al.* (2005): First principles methods using CASTEP. *Z. Kristallogr. - Cryst. Mater., 220 (5-6)*, 567–570, doi: 10.1524/zkri.220.5.567.65075.

[36] Perdew, J.P.; Burke, K.; Ernzerhof, M. (1996): Generalized gradient approximation made simple. *Phys. Rev. Lett., 77 (18)*, 3865–3868, doi: 10.1103/PhysRevLett.77.3865.

[37] Lejaeghere, K.; Bihlmayer, G.; Björkman, T.; Blaha, P. *et al.* (2016): Reproducibility in density functional theory calculations of solids. *Science, 351 (6280)*, aad3000, doi: 10.1126/science.aad3000.

[38] Monkhorst, H.J. & Pack, J.D. (1976): Special points for Brillouin-zone integrations. *Phys. Rev. B, 13 (12)*, 5188–5192, doi: 10.1103/PhysRevB.13.5188.

[39] Henning, T.; Begemann, B.; Mutschke, H.; Dorschner, J. (1995): Optical properties of oxide dust grains. *Astron. Astrophys. Suppl. Ser., 112*, 143–149.

[40] Kantor, I.; Dubrovinsky, L.S.; McCammon, C.A.; Steinle-Neumann, G. *et al.* (2009): Short-range order and Fe clustering in $Mg_{1-x}Fe_xO$ under high pressure. *Phys. Rev. B, 80 (1)*, doi: 10.1103/PhysRevB.80.014204.

[41] Lin, J.-F.; Gavriliuk, A.G.; Struzhkin, V.V.; Jacobsen, S.D. *et al.* (2006): Pressure-induced electronic spin transition of iron in magnesiowustite-(Mg,Fe)O. *Am. Mineral., 73 (11)*, 794, doi: 10.1103/PhysRevB.73.113107.

[42] Shannon, R.D. & Fischer, R.X. (2016): Empirical electronic polarizabilities of ions for the prediction and interpretation of refractive indices: Oxides and oxysalts. *Am. Mineral., 101 (10)*, 2288–2300, doi: 10.2138/am-2016-5730.

[43] Balzaretti, N.M. & Da Jornada, J.A. H. (1990): Volume dependence of the electronic polarizability of magnesium oxide. *High Pressure Res., 2 (3)*, 183–191, doi: 10.1080/08957959008201037.

[44] Fratanduono, D.E.; Eggert, J.H.; Akin, M.C.; Chau, R.; Holmes, N.C. (2013): A novel approach to Hugoniot measurements utilizing transparent crystals. *J. Appl. Phys., 114 (4)*, 43518, doi: 10.1063/1.4813871.

[45] Oganov, A.R.; Gillan, M.J.; Price, G.D. (2003): Ab initio lattice dynamics and structural stability of MgO. *J. Chem. Phys., 118 (22)*, 10174–10182, doi: 10.1063/1.1570394.

[46] Lorenz, C.D. & Ziff, R.M. (1998): Precise determination of the bond percolation thresholds and finite-size scaling corrections for the sc, fcc, and bcc lattices. *Phys. Rev. E, 57 (1)*, 230–236, doi: 10.1103/PhysRevE.57.230.

[47] Diamond, M.R.; Shen, G.; Popov, D.Y.; Park, C. *et al.* (2022): Electron density changes across the pressure-induced iron spin transition. *Phys. Rev. Lett., 129 (2)*, 25701, doi: 10.1103/PhysRevLett.129.025701.

[48] Lobanov, S.S.; Soubiran, F.; Holtgrewe, N.; Badro, J. *et al.* (2021): Contrasting opacity of bridgmanite and ferropericlase in the lowermost mantle: Implications to radiative and electrical conductivity. *Earth Planet. Sci. Lett., 562*, 116871, doi: 10.1016/j.epsl.2021.116871.

[49] Wemple, S.H. & DiDomenico, M. (1971): Behavior of the electronic dielectric constant in covalent and ionic materials. *Phys. Rev. B, 3 (4)*, 1338–1351, doi: 10.1103/PhysRevB.3.1338.

[50] Holmström, E. & Stixrude, L. (2015): Spin crossover in ferropericlase from first-principles molecular dynamics. *Phys. Rev. Lett., 114 (11)*, 117202, doi: 10.1103/PhysRevLett.114.117202.

[51] Hsu, H. & Wentzcovitch, R.M. (2014): First-principles study of intermediate-spin ferrous iron in the Earth's lower mantle. *Phys. Rev. B, 90 (19)*, doi: 10.1103/PhysRevB.90.195205.

[52] Li, H. & Wang, Q. (2015): The electronic properties of ferropericlase under pressure calculated by first principles. In: Ching & Dvorik (Eds.) Proceedings of the First International Conference on Information Sciences, Machinery, Materials and Energy, 126.

[53] Song, Y.; He, K.; Sun, J.; Ma, C. *et al.* (2019): Effects of iron spin transition on the electronic structure, thermal expansivity and lattice thermal conductivity of ferropericlase: a first principles study. *Sci. Rep., 9 (1)*, 4172, doi: 10.1038/s41598-019-40454-4.

[54] Sun, Y.; Zhuang, J.; Wentzcovitch, R.M. (2022): Thermodynamics of spin crossover in ferropericlase: an improved LDA+U_{sc} calculation. *Electron. Struct., 4 (1)*, 14008, doi: 10.48550/arXiv.2110.12637.

[55] Womes, M. & Jumas, J.C. (2013): Effect of Fe(II) spin crossover on charge distribution in and lattice properties of thiospinels. *J. Phys. Chem. Solids., 74 (3)*, 457–465, doi: 10.1016/j.jpcs.2012.11.011.

[56] Tauc, J. (1968): Optical properties and electronic structure of amorphous Ge and Si. *Mater. Res. Bull., 3 (1)*, 37–46, doi: 10.1016/0025-5408(68)90023-8.

[57] Sherman, D.M. & Waite, T.D. (1985): Electronic spectra of Fe^{3+} oxides and oxide hydroxides in the near IR to near UV. *Am. Mineral., 70*, 1262–1269.

[58] Cohen, R.E.; Mazin, I.I.; Isaak, D.G. (1997): Magnetic collapse in transition metal oxides at high pressure: *Science, 275 (5300)*, 654–657, doi: 10.1126/science.275.5300.654.

[59] Kuvshinov, A.; Grayver, A.; Tøffner-Clausen, L.; Olsen, N. (2021): Probing 3-D electrical conductivity of the mantle using 6 years of Swarm, CryoSat-2 and observatory magnetic data and exploiting matrix Q-responses approach. *EPS, 73 (1)*, doi: 10.1186/s40623-020-01341-9.

[60] Velímský, J. & Knopp, O. (2021): Lateral variations of electrical conductivity in the lower mantle constrained by Swarm and CryoSat-2 missions. *EPS, 73 (1)*, doi: 10.1186/s40623-020-01334-8.

[61] Holmström, E.; Stixrude, L.; Scipioni, R.; Foster, A.S. (2018): Electronic conductivity of solid and liquid (Mg, Fe)O computed from first principles. *Earth Planet. Sci. Lett., 490*, 11–19, doi: 10.1016/j.epsl.2018.03.009.

Chapter 4

Evolution of chemical bonding and spin-pairing energy in ferropericlase

Published in:

ACS Earth and Space Chemistry, 6, 788–799, 2022.

Evolution of chemical bonding and spin-pairing energy in ferropericlase

Lukas Schifferle[1,2] and Sergey S. Lobanov[1,2]

[1] *GFZ German Research Center for Geosciences, Telegrafenberg, 14473 Potsdam, Germany*

[2] *Institute of Geosciences, University of Potsdam, Karl-Liebknecht-Straße 24-25, 14476 Potsdam, Germany*

(Original version received: 27th May 2021, declined: 13th July 2021; resubmitted 8th January 2022; revised manuscript received 15th February 2022; accepted 18th February 2022; published 3rd March 2022)

The evolution of chemical bonding in ferropericlase, (Mg,Fe)O, with pressure may affect the physical and chemical properties of the Earth's lower mantle. Here we report high-pressure optical absorption spectra of single-crystalline ferropericlase ($(Mg_{0.87}Fe_{0.13})O$) up to 135 GPa. Combined with a re-evaluation of published partial fluorescence yield x-ray absorption spectroscopy data, we show that the covalency of the Fe-O bond increases with pressure but the iron spin transition at 57-76.5 GPa reverses this trend. The qualitative crossover in chemical bonding suggests that the spin-pairing transition weakens the Fe-O bond in ferropericlase. We find, that the spin transition in ferropericlase is caused by both the increase of the ligand field splitting energy and the decrease in spin-pairing energy of high-spin Fe^{2+}.

Author contributions: Conceptualization and high-pressure measurements by Lobanov. **Schifferle** performed the measurements at ambient condition and the analysis of all the data. **Schifferle** also wrote the original manuscript. Both authors contributed to the reviewing and editing of the manuscript.

DOI: 10.1021/acsearthspacechem.2c00014

4.1 Introduction

Because ferropericlase is the second most abundant phase of the Earth's lower mantle [1], its transport properties (e.g., viscosity, electrical conductivity, thermal conductivity, chemical diffusivity) have been extensively studied [2–21]. These physical properties are governed by the crystal structure, chemical composition and the bonding between the individual atoms of the crystal. At lower mantle pressures of 40-80 GPa [9; 10; 14; 22–26], ferropericlase undergoes a change in the spin state of Fe^{2+} from high-spin (HS) to low-spin (LS), which produces anomalies in the physical properties. The density increases discontinuously across the spin transition because the ionic radius of LS Fe^{2+} is smaller than that of HS Fe^{2+} [4; 20; 27]. Although the electrical conductivity of ferropericlase increases with pressure, it is decreased by a factor of three to four across the spin transition [15; 28]. Upon the spin transition, optical absorption in the mid- to near-infrared increases, thus resulting in reduced radiative thermal conductivity for the LS state [8; 10; 14]. In the pressure range of the spin transition the elastic constants of ferropericlase soften (especially in C_{11}, C_{12}) [29–32], viscosity [3; 33; 34] and P wave velocities are reduced [29; 35]. Furthermore, the iron partitioning between ferropericlase and the other phases of the lower mantle is anomalous [9; 33]. Therefore, information on how the Fe-O bond alters with pressure and ultimately spin-state is critical for our understanding of changes in the macroscopic properties of ferropericlase. Albeit its physical relevance [36–40], measuring the bond strength is difficult at the temperature and pressure conditions of the deep Earth. As a result, constraints on the bond strength of mantle minerals are scarce.

Pure MgO is a typical example of a compound dominated by ionic bonding. Introducing Fe (an element with a higher electronegativity on the Pauling scale) into the structure reduces the overall ionicity of the compound and achieves a higher covalent character of the metal-oxygen bond for the Fe-site. The only qualitative estimation of the covalency in the LS state is delivered by Keppler et al. [10] and Goncharov et al. [14]. However, to our knowledge there is no consistent information available on how the nature of the chemical bonding on the iron site evolves with pressure and changes upon the spin transition from HS to LS. In the present work we investigated the chemical Fe-O bonding in ferropericlase, by performing optical absorption experiments and re-examining partial fluorescence yield x-ray absorption spectroscopy (PFY-XAS) datasets [11], whereby evaluating how the strength of the chemical bond changes with pressure.

4.2 Experimental methods

4.2.1 Sample

The sample studied here is a synthetic single-crystal of ferropericlase ($(Mg_{0.87}Fe_{0.13})O$) produced by Fe diffusion into an MgO crystal in a gas-mixing furnace at ambient pressure. Electron energy loss spectroscopy (EELS) yielded an $Fe^{3+}/\sum Fe_{total}$ ratio of ~ 10% [41]. The ferropericlase single crystal was then ground and double-side polished to a thickness of ~16 μm to achieve a transparent, high-optical quality platelet.

4.2.2 Optical absorption measurements

At 1 atm, the spectra were collected using a Bruker Vertex 80v Fourier-transform infrared (FTIR) spectrometer equipped with a tungsten light source, CaF_2 and KBr beamsplitters, as well as Si-diode (VIS), InSb (NIR) and Hg-Cd-Te (MIR) detectors. The FTIR spectrometer is combined with a Bruker Hyperion 2000 IR microscope, serving for fine focussing on the sample and spatial filtering. The double polished sample was measured lying flat on a glass slide, using the latter as an optical reference.

High-pressure experiments were performed in a symmetrical diamond anvil cell (DAC) using Re as gasket material. Small fragments of the sample were placed between two dried KCl platelets, which served as a pressure-transmitting medium, and loaded into the sample chamber. To avoid any hydration of the dry KCl, the DAC was sealed directly after the loading. The shift of the high-frequency edge of the first-order Raman band of diamond [42] was used to measure the pressure. The uncertainty of the used method is ~5% relative [42]; comparable to pressure gradients expected for using KCl as a pressure transmitting medium [43]. Small ruby fragments served as pressure calibrants [44] to confirm the pressure estimation at $P < 100$ GPa. All high-pressure measurements were performed at room temperature using the instrumentation described in Goncharov et al. [8]. The all-reflective instrumental setup uses a combination of an FTIR and an UV/VIS spectrometer, allowing for measurements in a broad spectral range free of chromatic aberrations (2,500–30,000 cm^{-1}). A fibre coupled halogen-deuterium light source as well as a Xe flash lamp, were used for the measurements. The probe beam was focused to a spot of ~50 μm on the sample of which the central ~20 μm were spatially filtered by a confocal aperture and passed to the spectrometer. UV-VIS signal was recorded by a 300 grooves/mm grating of an Acton Research Corporation Spectra Pro 500-i spectrometer equipped with a thermoelectrically-cooled CCD. In the near-IR range, the spectra were collected by a Varian Resolution Pro 670-IR spectrometer with a quartz beamsplitter.

After stitching the individual spectral segments, the optical absorbance of the sample was evaluated as:

$$A = -\log_{10}\left(\frac{I_{sample} - I_{background}}{I_{reference} - I_{background}}\right) \quad \text{(Eq. 4.1)}$$

where I_{sample} and $I_{reference}$ are intensities measured through the sample and the pressure transmitting medium (or glass slide), which served as an optical reference. A dark measurement ($I_{background}$) with the light path to the spectrometer blocked, was subtracted from the measured spectra (I_{sample}, $I_{reference}$) to remove background light and dark current contributions. High-pressure optical absorption spectra were measured up to 135 GPa in ~10 GPa intervals. The fitting procedure was performed in Fityk v1.3.1 and PeakFit v4.11 using a Gaussian peak profile. All spectra reported in here were measured at room temperature.

4.3 Results and discussion

At ambient conditions six distinct features are observed in the spectrum: three peaks at 2,790 cm^{-1}, 3,334 cm^{-1} and 3,772 cm^{-1}, two broad intense bands at 9,306 cm^{-1} and 12,390 cm^{-1} as well as a weak band at

19,382 cm^{-1} (**Figure 4-1**). We attribute the three bands centred at ~3,300 cm^{-1} to OH-stretching vibrations in the hydrogenated surface of the single crystal, which we do not expect to significantly affect the properties of the bulk sample. Please note that hydrogenation of Mg-rich ferropericlase (as well as MgO) is inevitable because it is hygroscopic and has affinity for chemisorption of atmospheric moisture [45]. The energy of the two high-absorbance bands centred at ~9,300 cm^{-1} and ~12,400 cm^{-1} are typical of spin-allowed ligand field electronic transitions between 3*d* orbitals (*d-d* transitions) of HS Fe^{2+} in an octahedral coordination site [7; 10; 46–48]. Interestingly, their relative intensities are unusual because the high-energy band is typically of higher intensity. For example, the ligand field band of octahedrally-coordinated Fe^{2+} in ringwoodite [49; 50] has stronger absorbance at higher frequencies. The different mechanisms contributing to the absorption edge (Fe-O charge transfer in ringwoodite versus Fe-Fe charge transfer in ferropericlase, as discussed below) might cause a less-efficient intensity stealing from the absorption edge for ferropericlase, which would explain the unusual relative intensities of the ligand field bands in ferropericlase. Upon compression to 30 GPa, the two bands blue-shift with an average $(\partial \upsilon/\partial P)_T$ = 36 cm^{-1}/GPa for the low-frequency peak and $(\partial \upsilon/\partial P)_T$ = 61 cm^{-1}/GPa for the high frequency peak. At P = 41.5-63 GPa, however, the spectral positions of these bands are almost pressure independent (**Figure 2 & 3**). Ferrous iron has a $3d^6$ electronic configuration and in the HS state exhibits only one spin-allowed transition that satisfies the spin-multiplicity selection rule ($^5T_{2g} \rightarrow {}^5E_g$). The presence of two bands has been attributed to the Jahn-Teller effect [51], which allows lifting the energy degeneracy due to a distortion of the coordination site [51]. The Jahn-Teller splitting, characteristic of the spin-allowed bands, could only be resolved at $P \leq$ 30 GPa. Overall, our spectroscopic observations are consistent with those of Keppler et al. [10] who reported relatively stable peak positions between 36.7 and 43.7 GPa and no ligand field band splitting at $P >$ 36.7 GPa.

Despite the apparently high Fe^{3+} content (10% $Fe^{3+}/\sum Fe_{total}$) we do not observe any intervalence charge transfer (IVCT) bands between Fe^{2+} and Fe^{3+}. Intense broad absorption bands ~13,000-18,000 cm^{-1} [46] are characteristic of IVCT. Previous studies of ferropericlase also did not report on IVCT bands [10; 14]. In contrast, in $(Mg_{0.90}Fe_{0.10})_2SiO_4$ ringwoodite with a similar amount of Fe^{3+} (10% $Fe^{3+}/\sum Fe_{total}$), intense IVCT bands were found [49]. This could indicate that the effective Fe^{3+} content in our ferropericlase sample is lower than 10%. We note that the Fe^{3+} content was estimated based on EELS spectra [52], and therefore a substantial absolute error (±2% to ±3%) is to be expected, which might even be higher for samples with relatively low Fe^{3+} content [53]. According to Smith [54], $Fe^{2+} + Fe^{3+} \rightarrow Fe^{3+} + Fe^{2+}$ IVCT bands in Fe bearing MgO are expected to be weak and might overlap with the Jahn-Teller distorted $^5T_{2g} \rightarrow {}^5E_g$ transition of Fe^{2+}. Hence, it is possible that a weak IVCT band contributes to the spectra but of such a small intensity that we are not able to identify its contribution. Therefore, any influence on the observed band positions might only be minor and within the error bar of the fitting procedure (±200 cm^{-1}).

The weak band at ~19,300 cm^{-1} (1 atm) is resolved up to 51 GPa and shows a near-linear, slight negative pressure shift of $(\partial \upsilon/\partial P)_T$ = -18 cm^{-1}/GPa. Very similar features, although not discussed, are also present in the previously published absorption spectra of ferropericlase [10; 14]. Below we discuss possible assignments of this band. First, we rule out the assignment to an IVCT ($Fe^{2+} + Fe^{3+} \rightarrow Fe^{3+} + Fe^{2+}$) as these bands

generally blue-shift with pressure and are much broader [46]. One possibility is that this band represents one of the spin-forbidden bands of Fe^{3+} (ground state: $^6A_{1g}$, excited states: $^4T_{1g}$ or $^4T_{2g}$). Similarly, this weak band may represent one of the spin-forbidden bands of Fe^{2+} (ground state: $^5T_{2g}$ excited states: $^1A_{1g}$, $^3T_{1g}$, $^3T_{2g}$, $^1T_{1g}$, and $^1T_{2g}$). Both these interpretations may be compatible with the slight negative pressure shift of the weak band, but given the much higher concentration of Fe^{2+} than that of Fe^{3+} we suppose the weak band at ~19,300 cm^{-1} is one of the spin-forbidden bands of Fe^{2+}. Below we will return to the assignment of this band after extracting the ligand field strength and interelectronic repulsion parameters.

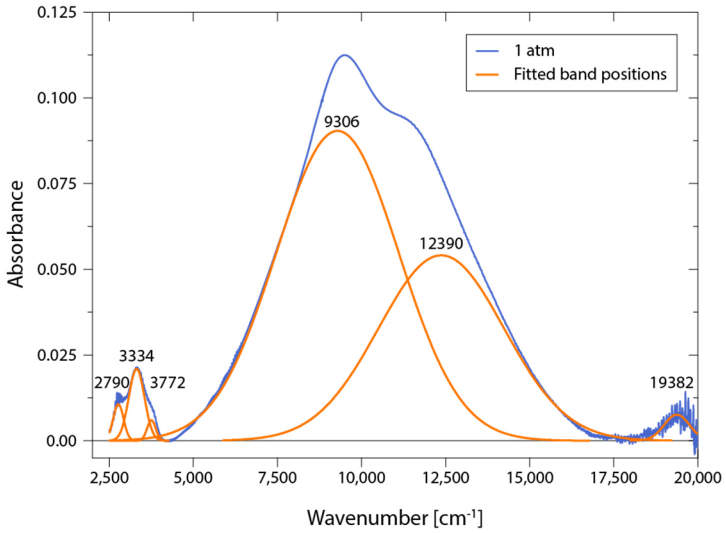

Figure 4-1 FTIR-VIS absorbance spectra of ferropericlase ($(Mg_{0.87}Fe_{0.13})O$) at 1 atm. Intense broad bands at 9,306 cm^{-1} and 12,390 cm^{-1} represent the $^5T_{2g} \rightarrow 5E_g$ transition split by the Jahn-Teller effect. The weak band at 19,382 cm^{-1} is likely a spin-forbidden transition of Fe^{2+} or Fe^{3+}. Low frequency bands (2,790 cm^{-1}, 3,334 cm^{-1}, 3,772 cm^{-1}) are assumed to be related to the inevitable surface hydrogenization of the sample [45]. Interference fringes were removed following Neri et al. [55].

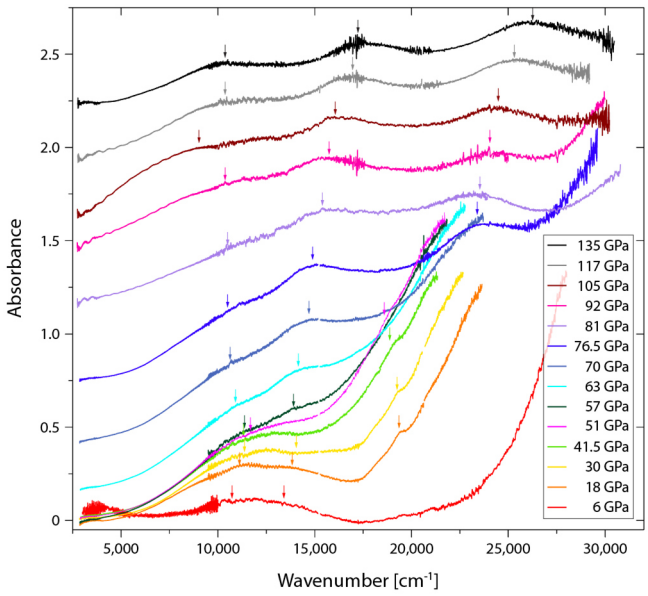

Figure 4-2 Optical absorption spectra of the high-pressure run. The spectra at pressures of ≥ 63 GPa are offset vertically for clarity. Peak positions are indicated by arrows. Spikes resulting from oversaturation on distinct spectral lines from the deuterium light source were removed. Fringes, if present, were eliminated from the dataset following the procedure of Neri et al. [55].

A qualitative change of the absorption spectra is evident at 57 GPa with the appearance of a new peak centred at 13,815 cm^{1} (**Figure 4-2**). The new peak grows in intensity and blue-shifts with pressure ($(\partial \upsilon/\partial P)_T$ = 46 cm^{-1}/GPa). The appearance of the new peak coincides with the disappearance of the weak band at ~19,000 cm^{-1}. Two additional bands centred at 9,324 cm^{-1} and 22,758 cm^{-1} can be resolved in the spectrum recorded at 76.5 GPa. The intensities, positions, and widths of the three new bands indicate that they correspond to spin-allowed ligand field electronic transitions of LS Fe^{2+}. Because a LS d^6 element has multiple spin-allowed transitions, the observation of the new bands provides strong optical evidence for the crossover to LS Fe^{2+}. From the spectroscopic behaviour described above, we may constrain the spin transition pressure range to 57-76.5 GPa, consistent with the compositional dependence of the spin crossover region in the MgO–FeO system [26; 56; 57]. We note that in ferropericlase the pressure range of the spin transition is broad [24; 56; 57], and it is difficult to detect its onset by optical spectroscopy because of the overlapping absorption bands of the HS and LS Fe^{2+}. Therefore, in the here presented dataset, 57 GPa likely represents the upper limit for the onset of the spin transition in our sample. For iron-rich ferropericlase (e.g., $(Mg_{0.6}Fe_{0.4})O$), however, there are indications that the cross-over region extends up to 136 GPa. [25].

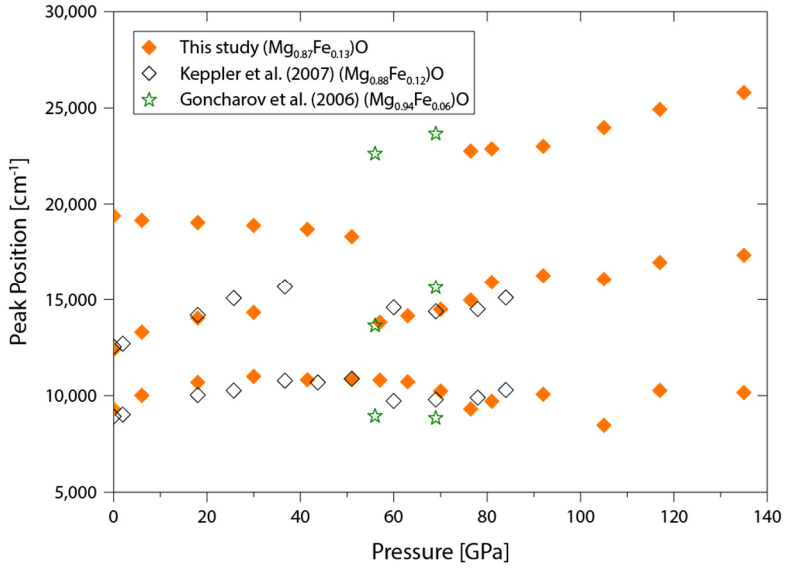

Figure 4-3 Fitted peak positions plotted against pressure. Data from Keppler et al. [10] and Goncharov et al. [14] are shown for comparison. Uncertainty of the position (1σ ≈ 200 cm^{-1}) is not shown as it is smaller than the symbol size.

In the HS state the high frequency absorption edge shows a red-shift with pressure and thus an increasing overall absorbance in the UV-VIS range. With the change in spin state, especially at pressures ≥ 63 GPa the absorption edge blue-shifts continuously (**Figure 4-2**), consistent with earlier experimental studies [10; 14]. Interestingly, siderite ($FeCO_3$) shows a red-shift of the absorption edge across the spin transition, which has been assigned to the Fe-O charge transfer [58]. In their supplementary material, Goncharov et al. [14] proposed, that the absorption edge of ferropericlase is mainly due to the *d-d* charge transfer between adjacent Fe^{2+} sites ($Fe^{2+} + Fe^{2+} \rightarrow Fe^{3+} + Fe^{+}$) and not exclusively due to the *p-d* Fe-O charge transfer ($Fe^{2+} + O^{2-} \rightarrow Fe^{3+} + O^{3-}$) because of the smaller energy required for a *d-d* compared to a *p-d* excitation. In siderite, Fe-Fe transfer is hindered by its crystal structure (corner-shared FeO_6 octahedra) as opposed to ferropericlase (all FeO_6 octahedral sites share 100% of their edges with other octahedra). The blue-shift in

ferropericlase, indicates an opening of the band gap across the HS-to-LS transition, consistent also with the drop in electrical conductivity by a factor of three to four across the spin transition [15; 28]. Our spectroscopic data suggests that the drop in electrical conductivity is likely caused by a strengthening of the Laporte selection rule due to decreasing population (and mixing) of *p* and *d* orbitals, which implies a trend towards a decreasing covalent character of the Fe-O bond. Unlike that in ferropericlase, the electrical conductivity of siderite is increased across the HS-to-LS transition [59]. The contrasting behaviour of the absorption edges (and electrical conductivities) of ferropericlase and siderite across their spin transitions hints that the origins of these spectral features are different.

To assign the three new ligand-field bands to specific excited states we performed a Tanabe-Sugano (T-S) diagram fit [60]. These energy level diagrams plot relative energies of ligand field states for a transition metal with a given electronic configuration and crystallographic coordination. T-S diagrams are constructed based on the empirically obtained interelectronic repulsion parameters Racah *B* and *C* from field-free transition metal ions in gaseous form and ions bound in crystal lattices [46]. The Racah *B* and *C* parameters are two of the three parameters introduced by Racah [61]. They express coulombic and exchange energies from interactions within the electron cloud of a field free atom. Hence, they are dependent on the amount and configuration of present electrons. Specifically, the Racah *B* parameter expresses the repulsion between the electrons of an atom and is used to describe variations in the size of the electron cloud but also the difference in the effective nuclear charge, with respect to a field-free atom, when a transition metal element is incorporated into a crystal structure. The Racah *B* parameter is generally considered a relative measure of the covalency of a bonded cation in a crystal structure [46; 62]. Changes in the Racah *B* parameter can therefore indicate a change in the chemical bond between a cation and its surrounding ligands. Quantitative fitting of the observed band positions of ligand field bands into the T-S diagram allows the assignment of the observed bands as well as estimating the ligand field splitting energy ($10Dq$) and extracting the Racah *B* parameter.

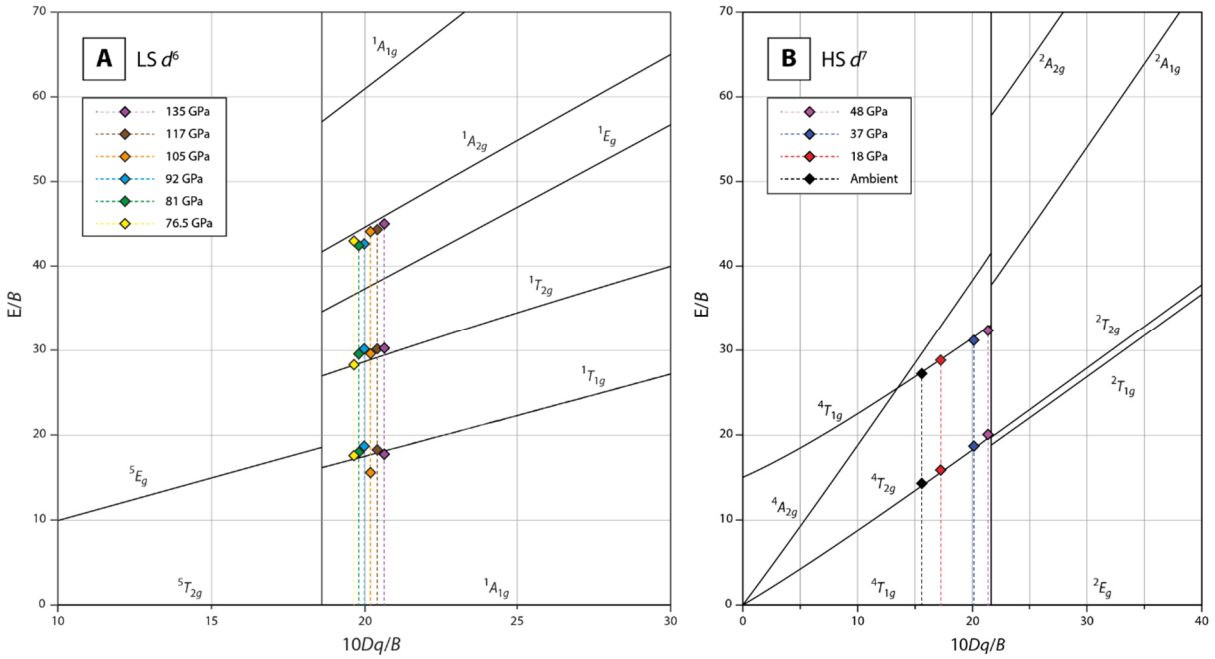

Figure 4-4 Tanabe-Sugano diagrams for octahedral coordination showing (A) d^6 Fe^{2+} with the fitting of the optical spectroscopy datasets for the LS state and (B) the fit of HS PFY-XAS data from Lin et al. [11] for HS d^7 Fe^{2+} (the d^7 configuration for Fe^{2+} is transient and is produced upon the core-valence excitation, please see the text for a more detailed explanation). Fitting was performed by ensuring overall minimum deviation from the assigned transitions.

The ratios of the peak positions from the observed *d-d* transitions at a given pressure can be used in a fitting procedure with respect to the E/B ratio of expected excited states (where E is the energy of an absorption band). To ensure a valid fit of the electronic transitions, the observation of at least two bands is required; more bands further strengthen the assignment. The observation of three distinct bands in the absorption spectra of LS Fe^{2+} (at $P \geq 76.5$ GPa) allowed to find robust $10Dq$ and Racah B in the process of T-S fitting (**Figure 4-4 A**). We assigned the experimentally observed absorption bands to the following spin-allowed ligand field transitions (from low frequency to high frequency): $^1A_{1g} \rightarrow {}^1T_{1g}$, $^1A_{1g} \rightarrow {}^1T_{2g}$ and $^1A_{1g} \rightarrow {}^1A_{2g}$. The obtained ligand field parameters (Racah B and $10Dq$) in LS ferropericlase are plotted in **Figure 4-5**.

.

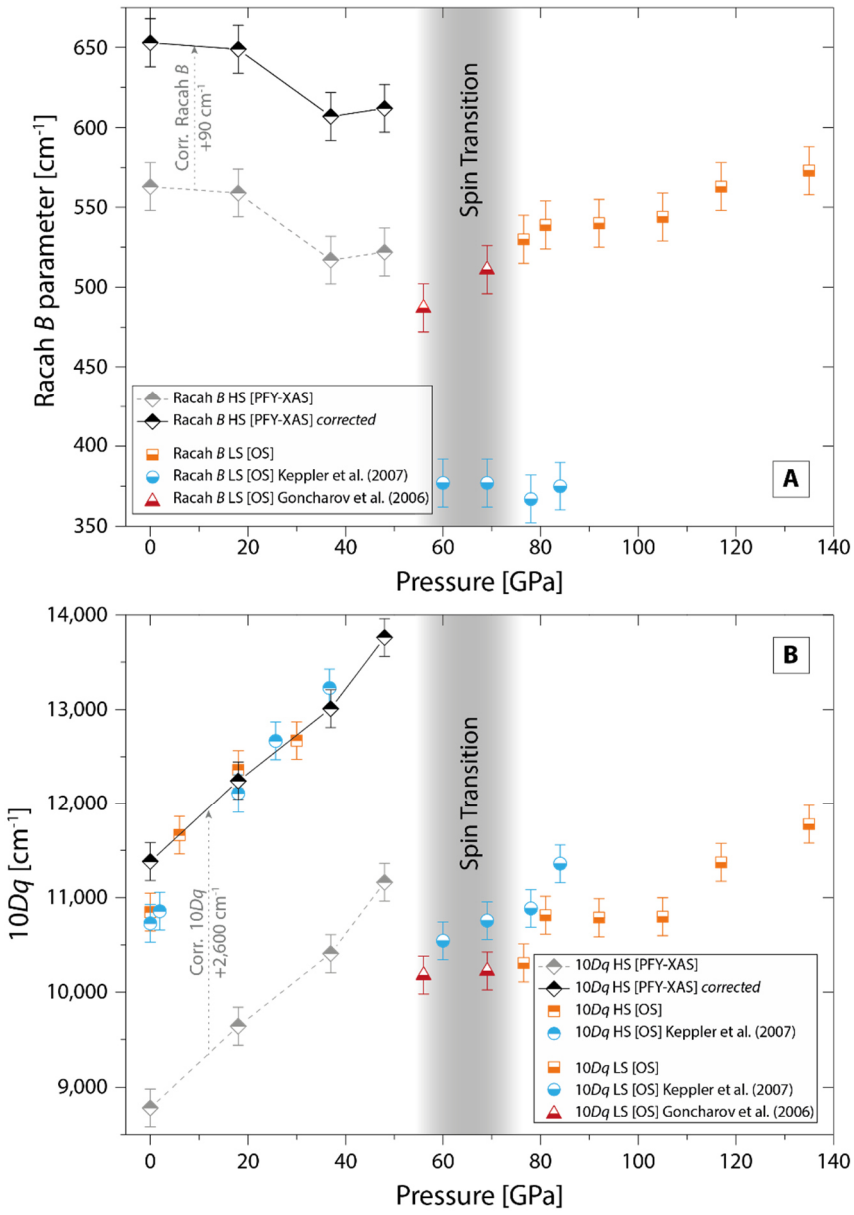

Figure 4-5 Variation of Racah *B* parameter (A) and ligand field splitting (10*Dq*) (B) with pressure (this study: orange squares, OS is for optical spectroscopy). Blue circles represent Racah *B* and 10*Dq* from the Tanabe-Sugano (T-S) fitting of data from Keppler et al. [10]. Red triangles depict 10*Dq* and Racah *B* from Goncharov et al. [14] using a new T-S fit of their reported spectra on $(Mg_{0.94}Fe_{0.06})O$ at 56 and 69 GPa. A: Diamonds show the Racah *B* parameter obtained from the T-S diagram fitting of PFY-XAS spectra [11] for the high-spin state (black and grey) and for the low-spin state. For the PFY-XAS dataset, the corrected Racah *B* parameter is obtained by adding 90 cm^{-1} to the T-S fitted value for d^7 configuration (see text for details on this correction). B: Ligand field splitting (10*Dq*) of high-spin state (black and grey) and low-spin state (orange) is shown. 10*Dq* derived from the transient d^7 configuration (PFY-XAS) is shifted by +2,600 cm^{-1} to account for the extra electron with respect to the d^6 configuration [46] (see text for details on this correction).

Because HS Fe^{2+} in $3d^6$ configuration exhibits only one spin-allowed transition, a T-S diagram fitting is not possible. In order to derive Racah *B* and 10*Dq* also for the HS state, we analysed the previously reported PFY-XAS data from Lin et al. [11] on ferropericlase ($(Mg_{0.75}Fe_{0.25})O$). During the PFY-XAS process an 1*s* electron on the iron atom is excited to form a transient d^7 iron configuration. The 1*s* level is subsequently filled by a 2*p* electron [63]. In the d^7 configuration iron has three spin-allowed electronic transitions, two of which ($^4T_{1g} \rightarrow {}^4T_{2g}$ and $^4T_{1g} \rightarrow {}^4T_{1g}$) are observed in the PFY-XAS data reported on Figure 7 (a) of

Lin et al. [11]. Fitting these two bands into the d^7 T-S diagram (**Figure 4-4:** B) allows the extraction of the ligand field parameters for HS ferropericlase (**Figure 4-5**), just as discussed above for T-S fitting of our own optical data.

The derived Racah *B* at ambient pressure resulting from the T-S diagram fitting of the PFY-XAS datasets is 563 cm^{-1} (±15). However, as this value derives from Fe in a transient d^7 configuration, a correction is needed. To correct for the extra electron and thus enable comparison to our data on LS (d^6) Fe^{2+}, we examine the (near-linear) dependence of Racah *B* on the oxidation state in field free cations [46; 51; 64]. For a field free cation we estimate a difference of 90 cm^{-1} between Racah *B* of d^6 (Fe^{2+}) and transient d^7 (equivalent to Fe^{+}) configuration [51; 65–69]. Accordingly, we add 90 cm^{-1} to the Racah *B* value obtained for the d^7 configuration which yields the corrected value for d^6 (**Figure 4-5**: A).

At ambient pressure we derive a corrected Racah *B* parameter of 653 cm^{-1}, this together with the knowledge of 10*Dq* allows the assignment of the band at 19,300 cm^{-1} using the T-S diagram for d^6 elements. From the $10Dq/B$ (~17) and E/B ratio (~30) we assign the band to the spin-forbidden transition of Fe^{2+}, $^5T_{2g} \rightarrow {}^1T_{2g}$ originating from the ^1I term of Fe^{2+}. This is also consistent with the pressure-induced red-shift of this band. Interestingly, we don't observe the spin-forbidden transition of $^5T_{2g} \rightarrow {}^1A_{1g}$ and $^5T_{2g} \rightarrow {}^1T_{1g}$ (also originating from the ^1I term) at lower energies. Likewise, we do not observe the spin-forbidden transitions originating from the ^3H term of Fe^{2+}, although their expected intensities would be higher as they are less forbidden by the spin-multiplicity selection rule than the ones originating from the ^1I term. We suppose that all these spin-forbidden transitions of Fe^{2+} have intensities too low to be observed and only $^5T_{2g} \rightarrow {}^1T_{2g}$ is present in the spectra due to intensity stealing from the high-energy absorption edge.

The observed behaviour with increasing pressure in the HS state shows a decrease in the Racah *B* parameter, which is in contradiction with molecular orbital calculations of Sherman [69] who argued that there is no significant increase in covalency with pressure. However, it has been experimentally confirmed for several transition metal bearing complexes, that the shortening of interatomic distances at high pressure leads to an increase in covalency [70–73]. Furthermore, the decrease in the Racah *B* parameter from 653 cm^{-1} (corrected for the d^7 configuration) at 1 atm to 612 cm^{-1} at 48 GPa (6.3% with $(\partial B/\partial P)_T$ = -0.85 cm^{-1}/GPa) is broadly consistent with the previous estimations that reported a minor reduction of ~2-6% over a 20 GPa [46; 72; 74].

Across the spin transition, the Racah *B* parameter decreases from 612 (±15) cm^{-1} at 48 GPa to 530 (±15) cm^{-1} at 76.5 GPa, equivalent to a decrease of ~13%. While we are not able to constrain the pressure derivative of Racah *B* in the spin transition range (due to the presence of HS bands in the spectra of mixed-spin ferropericlase the T-S fitting is less reliable), the added datapoints based on the study of Goncharov et al. [14] in Figure 4-5 suggest that Racah *B* reaches a minimum in the mixed-spin region and gradually increases towards the LS state. Our estimation of the Racah *B* parameter in the LS ferropericlase is very close to the Racah *B* which can be derived from the data of Goncharov et al. [14] (B = 511 cm^{-1} at 69 GPa). However, our estimate of Racah *B* for LS ferropericlase is significantly different from that of Keppler et al. [10], who reported 377 cm^{-1} at 60 GPa. We suppose that the reason for this apparent discrepancy is a

different fit of the T-S diagram. Although the assignment to the observed transitions in Keppler et al. [10] ($^1A_{1g} \rightarrow {}^1T_{1g}$, $^1A_{1g} \rightarrow {}^1T_{2g}$) is the same as in our dataset (**Figure 4-4 A**), the variation in Racah *B* is caused by the difference in the obtained $10Dq/B$ ratio. This is particularly important for the fit to two excited states whose energy separation is almost independent of $10Dq/B$ in the T-S diagram ($^1T_{1g}$ and $^1T_{2g}$ excited stated, which are the only two states probed by Keppler et al. [10]). For a two-peak fit, small deviations in the peak ratios might produce a significant shift in the estimated $10Dq/B$. The wider spectral range of our study enables us to observe three ligand field transitions, resulting in a much more reliable fitting of the T-S diagram. We note however, that we cannot completely rule out that the presence of a minor amount of Fe^{3+} did affect our fitting of the Fe^{2+} bands, which in turn would skew the derived Racah *B*.

A possible interpretation for the observed changes in the Racah *B* parameter might be found in the nature of the covalent bonding itself. Covalent bonding is based on the sharing of an electron pair between two neighbouring atoms. In Fe^{2+} in the HS state there are four unpaired electrons in total. The e_g sets of unpaired electrons (d_{z^2} and $d_{x^2-z^2}$ orbitals) are oriented along the x, y and z axes of the octahedron. Therefore, the atomic orbitals of the e_g electrons have a head-on overlap with the O^{2-} p_x, p_y and p_z orbitals populated by six $2p$ electrons (O^{2-} electronic configuration $1s^2 2s^2 2p^6$) to form bonding and anti-bonding σ molecular orbitals (**Figure 4-6**). We attribute the decrease in Racah *B* (**Figure 4-5**: **A**) with pressure in HS ferropericlase to a stronger overlap of the bonding σ orbitals facilitating constructive interference of the atomic orbitals and resulting in higher electron density along the Fe-O bond and stronger interelectronic repulsion. In LS ferropericlase, the electron density along the Fe-O direction is greatly reduced due to the vanishing electron population on the e_g level, suppressing the low-energy (and hence strongly stabilizing) σ bonds and decreasing the covalency by forming π bonds. As the strength of the covalent bonds is related to the orbital overlap [75], the formation of π bonds should cause a reduction of the Fe-O bond strength. Lateral overlap of the oxygen's *p* orbitals with the LS Fe^{2+} t_{2g} orbitals constitutes bonding (and non-bonding) π molecular orbitals, which are higher in energy than the bonding σ molecular orbitals. The occupation of non-bonding π orbitals explains the increase in the Racah *B* parameter, which indicates a less covalent nature of the Fe-O bond in the LS state. Further increase in pressure for LS Fe^{2+} leads to an increase in the Racah *B* parameter.

The relatively high degree of covalency preserved in the LS state can be explained by the formation of *p-d*-σ bonds. Here, σ bonds are formed between the unoccupied d_{z^2} and $d_{x^2-z^2}$ orbitals of LS Fe^{2+} and the electron pairs in the $2p$ orbitals of O^{2-}, which act as σ donors of electron density (**Figure 4-6**). Pressure-enhanced overlap of the O^{2-} $2p$ orbitals with the empty Fe^{2+} $3d$ (e_g) orbitals increases the probability of electron hopping between the orbitals. In any case, the chemical bond strength will largely be governed by the presence of π bonds between the t_{2g} (Fe^{2+}) and $2p$ (O^{2-}) orbitals. This is due to the expected low electron density on the hybridized orbitals by σ donation and their expected higher energy compared to π bonds between mutually occupied *p* and *d* orbitals. The change towards a less covalent Fe-O bond in LS ferropericlase is consistent with both the first-principles computations [76] and experimental electron density maps [77]. We note, that in the Earth's mantle the inferred change in Fe-O bonding will occur over a broader pressure range due to the effect of high temperature [78; 79].

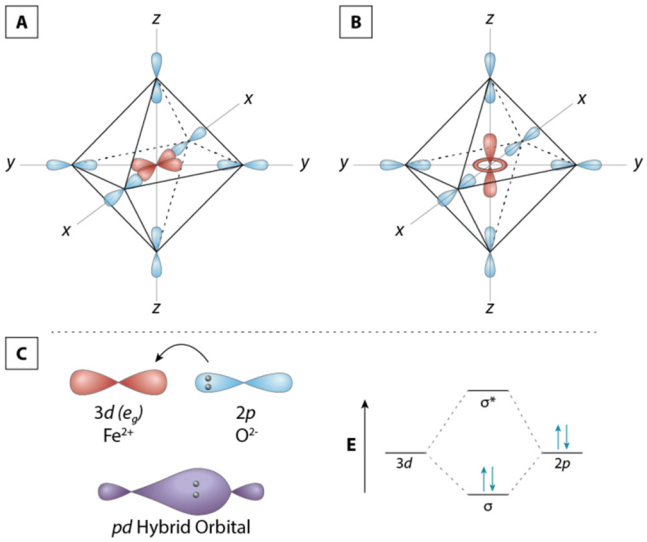

Figure 4-6 Geometrical orientation of the empty $d_{x^2-y^2}$ (red) (A) and d_{z^2} (red) (B) electronic orbitals of low-spin Fe^{2+} in octahedral configuration shown with respect to the and p_x, p_y, p_z orbitals of the O^{2-} ligands (blue). (C): Although the e_g orbitals of Fe^{2+} are unoccupied in the low-spin state, bonds can be formed due to geometrical orientation and σ donation from the ligand *p-d*-σ-orbitals, resulting in σ bonding and σ* anti-bonding molecular orbitals (right). As the σ bonding molecular orbitals are lower in energy than the σ* antibonding molecular orbitals, they will be filled first, satisfying the Hund's rules.

As shown by the optical spectroscopy data, the ligand field splitting energy (derived from the mean energy of the two ligand field transitions) increases with pressure in the HS state from ~10,800 cm^{-1} (ambient) to about ~12,700 cm^{-1} (30 GPa). The trend in $10Dq$ versus P for the HS state derived from the PFY-XAS data is very similar to the one based on our optical spectroscopy spectra. We note however, that similarly as for the Racah B parameter, a correction was applied to account for the d^7 configuration. By comparing $10Dq$ as reported by Burns [46] of Fe^{2+} (10,800 cm^{-1}) and Fe^{3+} (13,400 cm^{-1}) we approximate the increased *d-d* splitting due to the extra electron of 2,600 cm^{-1}. We then shifted the $10Dq$ from the PFY-XAS T-S fitting by adding 2,600 cm^{-1}. Across the spin transition, $10Dq$ decreases discontinuously and reaches values close to that at 1 atm. Further increase of pressure leads only to a moderate increase of $10Dq$ in the LS state (~22 cm^{-1}/GPa) (**Figure 4-5: B**). Siderite, for which a change in $10Dq$ across the spin transition has been documented, shows a different behaviour, where the change in the ligand field splitting energy is more sensitive to pressure (86 cm^{-1}/GPa [58], for HS) than *10Dq* in ferropericlase (52 cm^{-1}/GPa, for HS).

The extraction of Racah B for both HS and LS state allows us to calculate the spin-pairing energy (Π) using the following the equation [80] and assuming a Racah C/B ratio of approximately 4.5 [81; 67]:

$$\Pi = 2.5 \cdot B + 4 \cdot C \qquad \text{(Eq. 4.2)}$$

We show that the spin-pairing energy of Fe^{2+} in ferropericlase continuously decreases with pressure in the HS state (**Figure 4-7**). This is due to the increasing covalent character of the Fe-O bond where the Fe electrons are progressively shared with O. For the LS state we find that Π increases again. We note, that due to the uncertainty in the exact C/B ratio in ferropericlase, the error bars on Π are relatively large (±1,000 cm^{-1}). By comparing the spin-pairing energy together to the evolution of $10Dq$ we find that both the decrease of Π as well as the increase in $10Dq$ contribute to the onset of the spin transition in

ferropericlase. In full agreement with Hund's first rule, $\Pi > 10Dq$ in HS ferropericlase (at $P < \sim 40$ GPa) and $\Pi < 10Dq$ or $\Pi \sim 10Dq$ in LS ferropericlase. Surprisingly, from HS-to-LS $10Dq$ in ferropericlase decreases, whereas it increases in siderite (**Figure 4-7**), which underscores that $10Dq$ plays a primary role in triggering the spin transition in carbonates [58]. This observation also hints that the mechanisms of the spin transition in both phases are fundamentally different, likely due to the different intermediate range geometry of the Fe^{2+} site. As all edges of the octahedral iron site in ferropericlase are shared with other FeO_6 (or MgO_6) octahedra, each oxygen ligand and its electron density are shared between the six adjacent octahedra's cations. Hence, only a moderate increase in the ligand field splitting energy with pressure is to be expected for ferropericlase, which is also confirmed by our measurements (**Figure 4-5**: B) and explains faster increase in $10Dq/P$ in siderite than in ferropericlase. The sharing of electron density with the oxygen, with a higher number of adjacent cations when compared to iron bearing carbonates, contributes to the covalency in ferropericlase, consistent with the lower Racah B parameter of 530 cm^{-1} vs. 747 cm^{-1} in siderite [58] (both values for LS state). The influence of this difference in covalency is also expressed in the higher spin-pairing energy for siderite than in ferropericlase (**Figure 4-7**). In addition, the values of $10Dq$ are largely indistinguishable from Π in LS ferropericlase, which is probably why the pressure range of the spin transition in ferropericlase is broad (~ 20 GPa) compared to that in siderite (1-2 GPa [58; 82]).

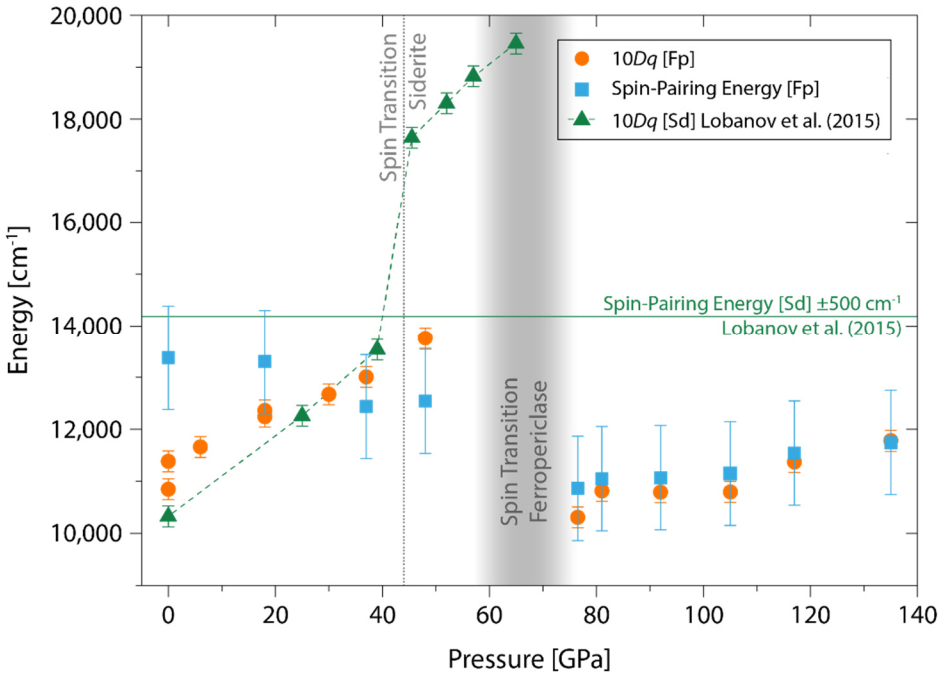

Figure 4-7 Comparison of spin-pairing energy (Π) and $10Dq$ in ferropericlase (Fp) and siderite (Sd). Spin-pairing energy is calculated using the formula $\Pi = 2.5*B + 4*C$ [80], assuming a fixed ratio of Racah $C/B = 4.5$. Data on siderite is based on Lobanov et al. [58]. We note that the spin-pairing energy of siderite is shown as a horizontal line because of the assumption of constant Racah parameters in siderite ($B = 747$ cm^{-1}, $C = 3{,}080$ cm^{-1}) [58].

Because our data derives from samples of different composition ($Fe_{0.25}$ vs $Fe_{0.13}$), we cannot fully rule out a compositional influence on the expected changes in $10Dq$ and Racah B. Further studies using compositionally identical samples, ideally analysed for iron distribution, are necessary to assess any potential effects of different iron contents also with respect to the interaction between nearest-neighbour Fe-sites. However, as

the comparison with lower Fe content ferropericlase ($(Mg_{0.94}Fe_{0.06})O$) [14] shows, neither band positions nor Racah *B* and $10Dq$ are considerably affected (**Figure 4-3**, **Figure 4-5**). We conclude that the moderate difference in iron content between the analysed HS (PFY-XAS) and LS (optical spectroscopy) datasets does not contribute significantly to the inferred changes in bonding and spin-pairing energies.

The here observed evolution of the Fe-O bond suggests that the spin crossover to LS Fe^{2+} tends to weaken the Fe-O bond. Below we examine how the change in Fe-O bond strength across the spin transition affects the physical properties of ferropericlase. The bulk modulus, for example, increases with pressure in the HS state but softens abruptly in the spin transition range due to the decrease in ferropericlase volume [3; 34; 76; 83-85]. Towards the LS end of the transition a hardening of the bulk modulus was observed, and for the full LS state the trend in bulk modulus is almost identical to the one of HS ferropericlase. [3; 34]. Therefore, the crossover to ionic-like bonding in LS ferropericlase does not show any clear effect on the bulk modulus. All previous studies [12; 17; 21] agree that the viscosity increases with pressure for HS ferropericlase. Similarly, there is a consensus that for the mixed spin state viscosity is reduced. However, the change of viscosity with depth (or pressure) in LS ferropericlase is controversial. Deng & Lee [21] found a reduction in the depth-viscosity derivative from HS to LS ferropericlase, whereas Marquardt & Miyagi [17] presented an increase in the pressure-derivative of viscosity. The model of Ammann et al. [12] predicts an almost pressure-independent viscosity for full LS ferropericlase, which is roughly similar to the results of Deng & Lee [21]. While it is possible that a reduction of the Fe-O bond strength can lower the increase in viscosity with pressure for LS ferropericlase, we were unable to reliably establish such a trend in the literature data.

The decreased strength of the Fe-O bond in LS inferred here may increase the diffusivity of Fe in ferropericlase. Previous studies found anomalies across the iron spin transition [12; 33; 86], especially Saha et al. [33] predicted increased diffusivity in the spin transition range. Towards the LS state diffusivity decreases [33], inconsistent with the expected decreased Fe-O bond strength. Therefore, the crossover to ionic-like Fe-O bonding found here has no significant effect on Fe diffusivity.

Many attempts have been made to estimate the influence of pressure, temperature and ultimately also the spin transition on the lattice thermal conductivity (k_{latt}) in ferropericlase [13; 19; 87; 88]. However, there is still an ongoing debate on the effect and magnitude of the spin transition on k_{latt}. While in the experimental studies there is a general consensus about an increase of k_{latt} with pressure, a reduction in the crossover-region and a further increase in the LS state, there are still many discrepancies in the theoretical models. Song et al. [13] found an increase in k_{latt} at the spin transition, whereas Wu [87] reports a decrease during the crossover and a lowering of the pressure dependence of k_{latt} of the LS state compared to the HS state. It is plausible, that the lowering of k_{latt} upon the spin transition can also be explained by a concurrent increase in electron delocalization. It has been shown, that the incorporation of group *IV-VI* elements in the rock salt structure can decrease k_{latt} due to resonant bonding and increased electron delocalization [89]. For (Mg,Fe)O ferropericlase this effect is very pronounced, as k_{latt} is significantly lower than in pure MgO [88]. The more ionic bonding in the LS state, might then explain the increasing k_{latt} towards the LS-end of the crossover region.

An increase in k_{latt} should be expected with a more pronounced electron localization as it is the case for ionic bonds [89].

4.4 Conclusions

Our work provides the first spectroscopic insights into the microscopic mechanisms responsible for the evolution of Fe-O bonding and spin-pairing energy in ferropericlase with pressure. Specifically, in the HS state the increase in pressure leads to a lower Racah *B* parameter implying a moderate pressure-related shift towards a more covalent Fe-O bonding in ferropericlase. The important microscopic mechanism in the spin transition region is the change from σ- to π-bonding and following population of higher energy molecular orbitals, leading to the expectation of lower bond-dissociation energies between Fe^{2+} and O^{2-}. Changes in the electron density distribution as a function of pressure and spin state result in changes in the covalency. For the LS state, a decreasing covalency is derived. As the bulk modulus seems unaffected by the variations in Fe-O bonding, the pressure-enhanced strength is more important for the transport properties than the changes in covalency. We conclude that the mechanism behind the spin transition in ferropericlase is the increase in the ligand field splitting energy concurrent with the decrease in the spin-pairing energy for HS Fe^{2+} (**Figure 4-7**). The findings on the evolution of the spin-pairing energy are also consistent with the changes in the covalency of the Fe-O bond (**Figure 4-8**).

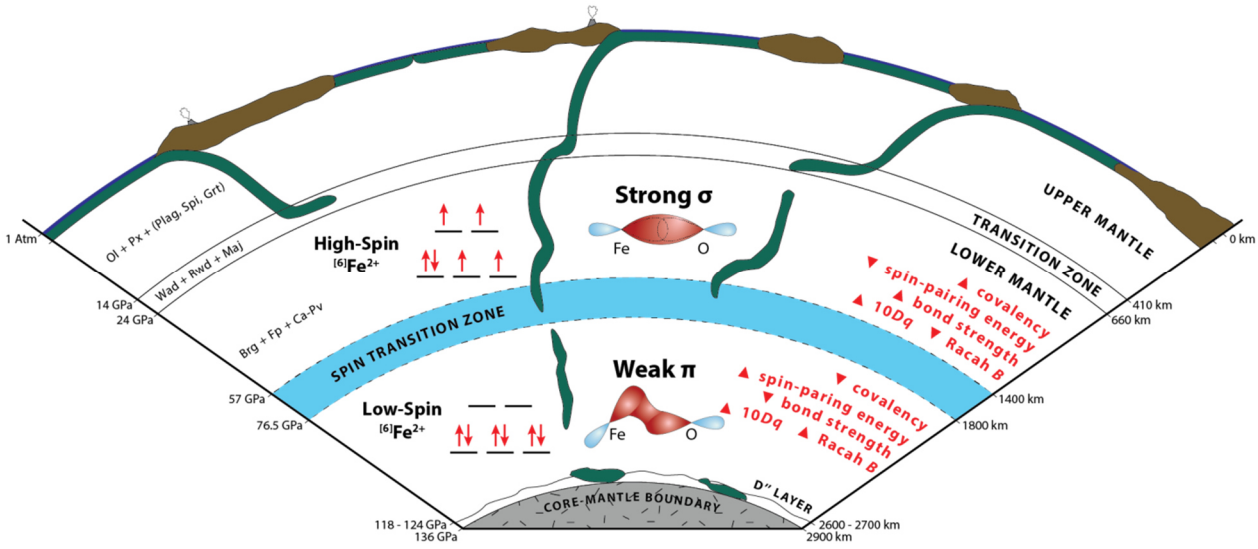

Figure 4-8 The electronic reconfiguration with the spin transition changes Fe-O bonding. Triangles depict a qualitative increase (▲) or decrease (▼) in *10Dq*, Racah *B*, spin-pairing energy (*Π*), and Fe-O bond strength. Whilst in the high-spin state σ bonds are formed between the oxygens 2*p* orbitals and the e_g level 3*d* electrons of Fe^{2+}, in the low-spin state a transition to π-dominant bonding takes place. Associated with the high-to-low-spin transition is a change in bond covalency. For the high-spin state an increasing covalency with pressure, due to increased overlap of the strong σ bonds, is inferred. In the low-spin state the trend towards higher ionicity is marked by the establishment of π bonds with reduced orbital overlap and a lowering of Fe-O bond strength. Please note, that the depicted pressure range for the spin transition is based on results of this study at ambient temperature. At the temperature conditions of the Earth's mantle a broader spin transition zone is expected [90].

4.5 References

[1] O'Neill, B. & Jeanloz, R. (1990): Experimental petrology of the lower mantle. *Geophys. Res. Lett., 17 (10)*, 1477–1480, doi: 10.1029/GL017i010p01477.

[2] Hazen, R.M. (1976): Effects of temperature and pressure on the cell dimension and X-ray temperature factors of periclase. *Am. Mineral., 61*, 266–271.

[3] Wentzcovitch, R.M.; Justo, J.F.; Wu, Z.; Da Silva, C.R. S. *et al.* (2009): Anomalous compressibility of ferropericlase throughout the iron spin cross-over. *Proc. Natl. Acad. Sci. U.S.A., 106 (21)*, 8447–8452, doi: 10.1073/pnas.0812150106.

[4] Solomatova, N.V.; Jackson, J.M.; Sturhahn, W.; Wicks, J.K. *et al.* (2016): Equation of state and spin crossover of (Mg,Fe)O at high pressure, with implications for explaining topographic relief at the core-mantle boundary. *Am. Mineral., 101 (5)*, 1084–1093, doi: 10.2138/am-2016-5510.

[5] Cohen, R.E.; Mazin, I.I.; Isaak, D.G. (1997): Magnetic collapse in transition metal oxides at high pressure: *Science, 275 (5300)*, 654–657, doi: 10.1126/science.275.5300.654.

[6] Lyubutin, I.S.; Struzhkin, V.V.; Mironovich, A.A.; Gavriliuk, A.G. *et al.* (2013): Quantum critical point and spin fluctuations in lower-mantle ferropericlase. *Proc. Natl. Acad. Sci. U.S.A., 110 (18)*, 7142–7147, doi: 10.1073/pnas.1304827110.

[7] Goto, T.; Ahrens, T.J.; Rossman, G.R.; Syono, Y. (1980): Absorption spectrum of shock-compressed Fe^{2+}-bearing MgO and the radiative conductivity of the lower mantle. *Phys. Earth Planet. Inter., 22 (3-4)*, 272–276, doi: 10.1016/0031-9201(80)90044-8.

[8] Goncharov, A.F.; Beck, P.; Struzhkin, V.V.; Haugen, B.D.; Jacobsen, S.D. (2009a): Thermal conductivity of lower-mantle minerals. *Phys. Earth Planet. Inter., 174 (1-4)*, 24–32, doi: 10.1016/j.pepi.2008.07.033.

[9] Badro, J.; Fiquet, G.; Guyot, F.; Rueff, J.-P. *et al.* (2003): Iron partitioning in Earth's mantle: toward a deep lower mantle discontinuity. *Science, 300 (5620)*, 789–791, doi: 10.1126/science.1081311.

[10] Keppler, H.; Kantor, I.; Dubrovinsky, L.S. (2007): Optical absorption spectra of ferropericlase to 84 GPa. *Am. Mineral., 92 (2-3)*, 433–436, doi: 10.2138/am.2007.2454.

[11] Lin, J.-F.; Mao, Z.; Jarrige, I.; Xiao, Y. *et al.* (2010): Resonant X-ray emission study of the lower-mantle ferropericlase at high pressures. *Am. Mineral., 95 (8-9)*, 1125–1131, doi: 10.2138/am.2010.3495.

[12] Ammann, M.W.; Brodholt, J.P.; Dobson, D.P. (2011): Ferrous iron diffusion in ferro-periclase across the spin transition. *Earth Planet. Sci. Lett., 302 (3-4)*, 393–402, doi: 10.1016/j.epsl.2010.12.031.

[13] Song, Y.; He, K.; Sun, J.; Ma, C. *et al.* (2019): Effects of iron spin transition on the electronic structure, thermal expansivity and lattice thermal conductivity of ferropericlase: a first principles study. *Sci. Rep., 9 (1)*, 4172, doi: 10.1038/s41598-019-40454-4.

[14] Goncharov, A.F.; Struzhkin, V.V.; Jacobsen, S.D. (2006b): Reduced radiative conductivity of low-spin (Mg,Fe)O in the lower mantle. *Science, 312 (5777)*, 1205–1208, doi: 10.1126/science.1125622.

[15] Lin, J.-F.; Weir, S.T.; Jackson, D.D.; Evans, W.J. *et al.* (2007): Electrical conductivity of the lower-mantle ferropericlase across the electronic spin transition. *Geophys. Res. Lett., 34 (16)*, doi: 10.1029/2007GL030523.

[16] Goncharov, A.F.; Lobanov, S.S.; Tan, X.; Hohensee, G.T. *et al.* (2015): Experimental study of thermal conductivity at high pressures. *Phys. Earth Planet. Inter., 247*, 11–16, doi: 10.1016/j.pepi.2015.02.004.

[17] Marquardt, H. & Miyagi, L. (2015): Slab stagnation in the shallow lower mantle linked to an increase in mantle viscosity. *Nat. Geosci., 8 (4)*, 311–314, doi: 10.1038/ngeo2393.

[18] Reali, R.; Jackson, J.M.; Van Orman, J.; Bower, D.J. *et al.* (2019): Modeling viscosity of (Mg,Fe)O at lowermost mantle conditions. *Phys. Earth Planet. Inter., 287*, 65–75, doi: 10.1016/j.pepi.2018.12.005.

[19] Ohta, K.; Yagi, T.; Hirose, K.; Ohishi, Y. (2017): Thermal conductivity of ferropericlase in the Earth's lower mantle. *Earth Planet. Sci. Lett., 465*, 29–37, doi: 10.1016/j.epsl.2017.02.030.

[20] Vilella, K.; Shim, S.-H.; Farnetani, C.G.; Badro, J. (2015): Spin state transition and partitioning of iron: Effects on mantle dynamics. *Earth Planet. Sci. Lett., 417*, 57–66, doi: 10.1016/j.epsl.2015.02.009.

[21] Deng, J. & Lee, K.K. M. (2017): Viscosity jump in the lower mantle inferred from melting curves of ferropericlase. *Nat. Commun., 8 (1)*, 1997, doi: 10.1038/s41467-017-02263-z.

[22] Lin, J.-F.; Struzhkin, V.V.; Jacobsen, S.D.; Hu, M.Y. *et al.* (2005): Spin transition of iron in magnesiowüstite in the Earth's lower mantle. *Nature, 436 (7049)*, 377–380, doi: 10.1038/nature03825.

[23] Lin, J.-F. & Tsuchiya, T. (2008): Spin transition of iron in the Earth's lower mantle. *Phys. Earth Planet. Inter., 170 (3-4)*, 248–259, doi: 10.1016/j.pepi.2008.01.005.

[24] Speziale, S.; Milner, A.; Lee, V.E.; Clark, S.M. *et al.* (2005): Iron spin transition in Earth's mantle. *Proc. Natl. Acad. Sci. U.S.A., 102 (50)*, 17918–17922, doi: 10.1073/pnas.0508919102.

[25] Hamada, M.; Kamada, S.; Ohtani, E.; Sakamaki, T. *et al.* (2021): Synchrotron Mössbauer spectroscopic and x-ray diffraction study of ferropericlase in the high-pressure range of the lower mantle region. *Phys. Rev. B, 103 (17)*, doi: 10.1103/PhysRevB.103.174108.

[26] Glazyrin, K.; Miyajima, N.; Smith, J.S.; Lee, K.K. M. (2016): Compression of a multiphase mantle assemblage. *J. Geophys. Res.: Solid Earth, 121 (5)*, 3377–3392, doi: 10.1002/2015JB012321.

[27] Lin, J.-F.; Speziale, S.; Mao, Z.; Marquardt, H. (2013): Effects of the electronic spin transitions of iron in lower mantle minerals. *Rev. Geophys., 51 (2)*, 244–275, doi: 10.1002/rog.20010.

[28] Ohta, K.; Hirose, K.; Onoda, S.; Shimizu, K. (2007): The effect of iron spin transition on electrical conductivity of (Mg,Fe)O magnesiowüstite. *Proc. Jpn. Acad. Ser. B Phys. Biol. Sci., 83 (3)*, 97–100, doi: 10.2183/pjab.83.97.

[29] Yang, J.; Tong, X.; Lin, J.-F.; Okuchi, T.; Tomioka, N. (2015): Elasticity of ferropericlase across the spin crossover in the Earth's lower mantle. *Sci. Rep., 5*, 17188, doi: 10.1038/srep17188.

[30] Marquardt, H.; Speziale, S.; Reichmann, H.J.; Frost, D.J.; Schilling, F.R. (2009): Single-crystal elasticity of $(Mg_{0.9}Fe_{0.1})O$ to 81 GPa. *Earth Planet. Sci. Lett., 287 (3-4)*, 345–352, doi: 10.1016/j.epsl.2009.08.017.

[31] Crowhurst, J.C.; Brown, J.M.; Goncharov, A.F.; Jacobsen, S.D. (2008): Elasticity of (Mg,Fe)O through the spin transition of iron in the lower mantle. *Science, 319 (5862)*, 451–453, doi: 10.1126/science.1149606.

[32] Wu, Z.; Justo, J.F.; Wentzcovitch, R.M. (2013): Elastic anomalies in a spin-crossover system: ferropericlase at lower mantle conditions. *Phys. Rev. Lett., 110 (22)*, 228501, doi: 10.1103/PhysRevLett.110.228501.

[33] Saha, S.; Bengtson, A.; Morgan, D. (2013): Effect of anomalous compressibility on Fe diffusion in ferropericlase throughout the spin crossover in the lower mantle. *Earth Planet. Sci. Lett., 362*, 1–5, doi: 10.1016/j.epsl.2012.11.032.

[34] Marquardt, H.; Buchen, J.; Mendez, A.S. J.; Kurnosov, A. *et al.* (2018): Elastic softening of $(Mg_{0.8}Fe_{0.2})O$ ferropericlase across the iron spin crossover measured at seismic frequencies. *Geophys. Res. Lett., 45 (14)*, 6862–6868, doi: 10.1029/2018GL077982.

[35] Wu, Z. & Wentzcovitch, R.M. (2014): Spin crossover in ferropericlase and velocity heterogeneities in the lower mantle. *Proc. Natl. Acad. Sci. U.S.A., 111 (29)*, 10468–10472, doi: 10.1073/pnas.1322427111.

[36] Mohn, C.E. & Trønnes, R.G. (2016): Iron spin state and site distribution in $FeAlO_3$-bearing bridgmanite. *Earth Planet. Sci. Lett., 440*, 178–186, doi: 10.1016/j.epsl.2016.02.010.

[37] Cammarata, A. & Rondinelli, J.M. (2012): Spin-assisted covalent bond mechanism in "charge-ordering" perovskite oxides. *Phys. Rev. B, 86 (19)*, doi: 10.1103/PhysRevB.86.195144.

[38] Chainani, A.; Yamamoto, A.; Matsunami, M.; Eguchi, R. *et al.* (2013): Quantifying covalency and metallicity in correlated compounds undergoing metal-insulator transitions. *Phys. Rev. B, 87 (4)*, doi: 10.1103/PhysRevB.87.045108.

[39] Thomann, H. (1987): A covalency model of ferroic phase transitions in perovskites. *Ferroelectrics, 73 (1)*, 183–199, doi: 10.1080/00150198708227917.

[40] Sun, Y.; Liao, H.; Wang, J.; Chen, B. *et al.* (2020): Covalency competition dominates the water oxidation structure–activity relationship on spinel oxides. *Nat. Catal., 3 (7)*, 554–563, doi: 10.1038/s41929-020-0465-6.

[41] Lobanov, S.S. & Speziale, S. (2019): Radiometric temperature measurements in nongray ferropericlase with pressure- spin- and temperature-dependent optical properties. *J. Geophys. Res.: Solid Earth, 124 (12)*, 12825–12836, doi: 10.1029/2019JB018668.

[42] Akahama, Y. & Kawamura, H. (2006): Pressure calibration of diamond anvil Raman gauge to 310 GPa. *J. Appl. Phys., 100 (4)*, 43516, doi: 10.1063/1.2335683.

[43] Uts, I.; Glazyrin, K.; Lee, K.K. M. (2013): Effect of laser annealing of pressure gradients in a diamond-anvil cell using common solid pressure media. *Rev. Sci. Instrum., 84 (10)*, 103904, doi: 10.1063/1.4821620.

[44] Dewaele, A.; Datchi, F.; Loubeyre, P.; Mezouar, M. (2008): High pressure–high temperature equations of state of neon and diamond. *Phys. Rev. B, 77 (9)*, doi: 10.1103/PhysRevB.77.094106.

[45] Ito, T.; Sekino, T.; Moriai, N.; Tokuda, T. (1981): Hydrogen adsorption on magnesium oxide powders. *J. Chem. Soc., Faraday Trans. 1, 77 (9)*, 2181, doi: 10.1039/F19817702181.

[46] Burns (1993): Mineralogical Applications of Crystal Field Theory. 2nd ed. Cambridge: Cambridge University Press, 5.

[47] Shankland, T.J. (1968): Pressure shift of absorption bands in MgO: Fe^{2+} and the dynamic Jahn-Teller effect. *J. Phys. Chem. Solids., 29*, 1907–1909.

[48] Mao, H.-K. (1973): Observations of optical absorption and electrical conductivity in magnesiowüstite at high pressure. *Yearb. Carnegie Inst. Washington, 72*, 554–557.

[49] Keppler, H. & Smyth, J.R. (2005): Optical and near infrared spectra of ringwoodite to 21.5 GPa. *Am. Mineral., 90 (7)*, 1209–1212, doi: 10.2138/am.2005.1908.

[50] Taran, M.N.; Koch-Müller, M.; Wirth, R.; Abs-Wurmbach, I. *et al.* (2009): Spectroscopic studies of synthetic and natural ringwoodite, γ-$(Mg, Fe)_2SiO_4$. *Phys. Chem. Minerals., 36 (4)*, 217–232, doi: 10.1007/s00269-008-0271-1.

[51] Lever (1984): Inorganic Electronic Spectroscopy. 2nd ed. Amsterdam: Elsevier, 33.

[52] Garvie, L.A. J. & Buseck, P.R. (1998): Ratios of ferrous to ferric iron from nanometre-sized areas in minerals. *Nature, 396 (6712)*, 667–670, doi: 10.1038/25334.

[53] Van Aken, P.A. & Liebscher, B. (2002): Quantification of ferrous/ferric ratios in minerals: new evaluation schemes of Fe L_{23} electron energy-loss near-edge spectra. *Phys. Chem. Minerals., 29 (3)*, 188–200, doi: 10.1007/s00269-001-0222-6.

[54] Smith, G. (1980): Evidence for optical absorption by Fe^{2+}-Fe^{3+} interactions in MgO:Fe. *Phys. Stat. Sol. A, 61 (2)*, K191-K195, doi: 10.1002/pssa.2210610267.

[55] Neri, F.; Saitta, G.; Chiofalo, S. (1987): A simple procedure to remove the interference fringes from optical spectra. *J. Phys. E: Sci. Instrum., 20*, 894–896.

[56] Kantor, I.; Dubrovinsky, L.S.; McCammon, C.A.; Steinle-Neumann, G. *et al.* (2009): Short-range order and Fe clustering in $Mg_{1-x}Fe_xO$ under high pressure. *Phys. Rev. B, 80 (1)*, doi: 10.1103/PhysRevB.80.014204.

[57] Lin, J.-F.; Gavriliuk, A.G.; Struzhkin, V.V.; Jacobsen, S.D. *et al.* (2006): Pressure-induced electronic spin transition of iron in magnesiowustite-(Mg,Fe)O. *Am. Mineral., 73 (11)*, 794, doi: 10.1103/PhysRevB.73.113107.

[58] Lobanov, S.S.; Goncharov, A.F.; Litasov, K.D. (2015): Optical properties of siderite ($FeCO_3$) across the spin transition. *Am. Mineral., 100 (5-6)*, 1059–1064, doi: 10.2138/am-2015-5053.

[59] Zhao, C.; Zhu, J.; Wei, X.; Zuhang, Y. *et al.* (2019): Abnormal electrical conductivity of siderite across the spin transition. *Proc. 2019 China Earth Sci. Jt. Acad. Conf.*

[60] Tanabe, Y. & Sugano, S. (1954): On the absorption spectra of complex ions I. *J. Phys. Soc. Jpn., 9 (5)*, 753–766, doi: 10.1143/JPSJ.9.753.

[61] Racah, G. (1942): Theory of complex spectra. II. *Phys. Rev., 62*, 438–462.

[62] Manning, P.G. (1970): Racah parameters and their relationship to lengths and covalencies of Mn^{2+}- and Fe^{3+}-oxygen bonds in silicates. *Can. Mineral., 10 (4)*, 677–688.

[63] Westre, T.E.; Kennepohl, P.; DeWitt, J.G.; Hedman, B. *et al.* (1997): A multiplet analysis of Fe K-edge 1s → 3d pre-edge features of iron complexes. *J. Am. Chem. Soc., 119 (27)*, 6297–6314, doi: 10.1021/ja964352a.

[64] Brik & Chong-Geng (2020): Theoretical Spectroscopy of Transition Metal and Rare Earth Ions. From Free State to Crystal Field. Singapore: Jenny Stanford Publishing.

[65] Cotton, F.A. (Ed.) (1962): Progress in Inorganic Chemistry. Hoboken: John Wiley & Sons.

[66] Andreici, E.L.; Gruia, A.S.; Avram, N.M. (2012): The parameters of the free ions Mn^{5+} and Fe^{6+}. *Phys. Scr.,, T149*, 14060, doi: 10.1088/0031-8949/2012/T149/014060.

[67] Sugano et al. (1970): Multiplets of Transition-Metal Ions in Crystals. Oxford: Elsevier Science, 33.

[68] Gao, F. & Zhang, S. (1997): Investigation of mechanism of nephelauxetic effect. *J. Phys. Chem. Solids., 58 (12)*, 1991–1994, doi: 10.1016/S0022-3697(96)00139-4.

[69] Sherman, D.M. (1991): The high-pressure electronic structure of magnesiowustite (Mg, Fe)O. *J. Geophys. Res., 96 (B9)*, 14299–14312, doi: 10.1029/91JB01202.

[70] Jørgensen, C.K. (1962): The nephelauxetic series. In: Cotton (Ed.): Progress in Inorganic Chemistry, 73–124.

[71] Du, M. (1992): Pressure dependence of spin-orbit coupling parameters of ruby. *Phys. Lett. A, 163 (4)*, 326–328, doi: 10.1016/0375-9601(92)91020-R.

[72] Abu-Eid, R.M. & Burns, R.G. (1976): The effect of pressure on the degree of covalency of the cation-oxygen bond in minerals. *Am. Mineral., 61 (5-6)*, 391–397.

[73] Zheng, W.-C.; Li, W.; Wu, S.-Y. (1999): Investigations of the pressure dependence of optical spectra for NiO crystal. *Phys. Stat. Sol. A, 173 (2)*, 437–440, doi: 10.1002/(SICI)1521-396X(199906)173:2<436::AID-PSSA437>3.0.CO;2-F.

[74] Drickamer & Frank (1973): Electronic Transitions and the High Pressure Chemistry and Physics of Solids. Dordrecht: Springer.

[75] Murrell, J.N. (1960): Construction of Hybrid Orbitals. *J. Chem. Phys., 32 (3)*, 767–770, doi: 10.1063/1.1730797.

[76] Tsuchiya, T.; Wentzcovitch, R.M.; Da Silva, C.R. S.; Gironcoli, S. de (2006): Spin transition in magnesiowüstite in Earth's lower mantle. *Phys. Rev. Lett., 96 (19)*, 198501, doi: 10.1103/PhysRevLett.96.198501.

[77] Diamond, M.R. (2020): Towards a deeper understanding of the iron spin transition. PhD thesis. University of California, Berkeley.

[78] Komabayashi, T.; Hirose, K.; Nagaya, Y.; Sugimura, E.; Ohishi, Y. (2010): High-temperature compression of ferropericlase and the effect of temperature on iron spin transition. *Earth Planet. Sci. Lett., 297 (3-4)*, 691–699, doi: 10.1016/j.epsl.2010.07.025.

[79] Lin, J.-F.; Vankó, G.; Jacobsen, S.D.; Iota, V. *et al.* (2007): Spin transition zone in Earth's lower mantle. *Science, 317 (5845)*, 1740–1743, doi: 10.1126/science.1144997.

[80] König, E. & Kremer, S. (1971): Exact spin-pairing energies at the crossovers in octahedral d^4, d^5, d^6, and d^7 transition metal complexes. *Theoret. chim. Acata, 23*, 12–20, doi: 10.1007/BF00530196.

[81] Gunasekaran, S. & Anbalagan, G. (2008): Optical absorption and EPR studies on some natural carbonate minerals. *Spectrochim Acta A Mol Biomol Spectrosc, 69 (2)*, 383–390, doi: 10.1016/j.saa.2007.04.010.

[82] Lavina, B.; Dera, P.; Downs, R.T.; Prakapenka, V.B. *et al.* (2009): Siderite at lower mantle conditions and the effects of the pressure-induced spin-pairing transition. *Geophys. Res. Lett., 36 (23)*, 789, doi: 10.1029/2009GL039652.

[83] Fei, Y.; Zhang, L.; Corgne, A.; Watson, H. *et al.* (2007): Spin transition and equations of state of (Mg, Fe)O solid solutions. *Geophys. Res. Lett., 34 (17)*, doi: 10.1029/2007GL030712.

[84] Glazyrin, K.; Sinmyo, R.; Bykova, E.; Bykov, M. *et al.* (2017): Critical behavior of $Mg_{1-x}Fe_xO$ at the pressure-induced iron spin-state crossover. *Phys. Rev. B, 95 (21)*, doi: 10.1103/PhysRevB.95.214412.

[85] Lin, J.-F.; Wenk, H.-R.; Voltolini, M.; Speziale, S. *et al.* (2009): Deformation of lower-mantle ferropericlase (Mg,Fe)O across the electronic spin transition. *Phys. Chem. Minerals., 36 (10)*, 585–592, doi: 10.1007/s00269-009-0303-5.

[86] Saha, S.; Bengtson, A.; Crispin, K.L.; Van Orman, J.A.; Morgan, D. (2011): Effects of spin transition on diffusion of Fe^{2+} in ferropericlase in Earth's lower mantle. *Phys. Rev. B, 84 (18)*, doi: 10.1103/PhysRevB.84.184102.

[87] Wu, Z. (2018): Thermal conductivity anomaly in spin-crossover ferropericlase under lower mantle conditions and implications for heat flow across the core-mantle boundary. *Am. Mineral., 103 (12)*, 1953–1958, doi: 10.2138/am-2018-6690.

[88] Hsieh, W.-P.; Deschamps, F.; Okuchi, T.; Lin, J.-F. (2018): Effects of iron on the lattice thermal conductivity of Earth's deep mantle and implications for mantle dynamics. *Proc. Natl. Acad. Sci. U.S.A., 115 (16)*, 4099–4104, doi: 10.1073/pnas.1718557115.

[89] Lee, S.; Esfarjani, K.; Luo, T.; Zhou, J. *et al.* (2014): Resonant bonding leads to low lattice thermal conductivity. *Nat. Commun., 5*, 3525, doi: 10.1038/ncomms4525.

[90] Holmström, E. & Stixrude, L. (2015): Spin crossover in ferropericlase from first-principles molecular dynamics. *Phys. Rev. Lett., 114 (11)*, 117202, doi: 10.1103/PhysRevLett.114.117202.

Chapter 5 Discussion

The primary objective of this thesis was to establish links between optical properties and physical material properties under high-pressure conditions. By focusing on common mantle minerals, this thesis aimed at deepening our understanding of their behavior under extreme conditions relevant to Earth and other planetary bodies. In particular, the research presented examines two optical properties: the refractive index and the optical absorption. Through the exploration of the Mg-Fe-O system's response to varying pressure, we gained new insights into fundamental material properties of periclase and ferropericlase, which are both key components in the construction of planetary bodies (McWilliams et al., 2012; Musella et al., 2019; Spaargaren et al., 2023).

5.1 High-pressure refractive index

5.1.1 MgO

In Chapter 2 I present analyses of the refractive index of MgO, which have been published in Schifferle et al. (2022). The study revealed new experimental insights on the refractive index of MgO up to pressure conditions of the core-mantle boundary. Specifically, we observed a decrease of the index at 600 nm by ~2.4% from ~1.7373 at 1 atm to ~1.696 (±0.017) at ~140 GPa. This dataset provides the first measurements of the refractive index of MgO in the VIS region, at pressures exceeding 30 GPa. To further investigate the physical properties of MgO, we conducted a single-effective oscillator analysis utilizing the refractive index dataset. We found that the band gap of MgO increases by ~1 eV, from 7.4 eV at 1 atm to ~8.4 (±0.6) eV at ~103 GPa. The unique capability of the DAC to function as a Fabry-Perot interferometer, allowed to extract the thickness of the pressurized sample based on an analysis of the interference pattern. Consequently, the refractive index data allowed to monitor diamond cupping and measure sample volume (V).

We found that the refractive index of MgO is consistent with the previously published data (Stephens and Malitson, 1952; Balzaretti and Da Jornada, 1990; Oganov et al., 2003; Stevens et al., 2006; Fratanduono et al., 2013) (see **Figure 2-2**). As MgO is commonly used in DAC experiments, either as a pressure transmitting medium (e.g., Pigott et al., 2015) or as a primary pressure scale (e.g., Zha et al., 2000), the refractive index of MgO (as published in Schifferle et al., 2022) will serve as a useful tool to characterize the thinning of sample assemblages in DAC with MgO as pressure medium. As recently pointed out by Lobanov and Geballe (2022), in-situ thickness determinations are essential for high-pressure thermal conductivity measurements (Lobanov and Geballe, 2022). Future studies of mantle and core thermal and electrical conductivities may use the now-available index of MgO to constrain sample thickness at high pressure without the need to rely on the assumption that sample thickness changes isotropically upon compression or decompression. As such, our data will contribute to establishing more reliable constraints on the heat and charge transfer in

deep planetary interiors. In addition, this work has already contributed to the refinement of sound velocities and elastic constants of MgO (Zhang et al., 2023).

The presented band gap data up to 103 GPa represents the first experimental constraint on the band gap of MgO. Although the postulated ratio of $E_0/1.5 \approx$ band gap by Wemple and DiDomenico (1971) is certainly not universal (e.g., 2 in Studenyak et al., 2020 or 1.4–1.9 in Shaaker et al., 2012), the proximity of the postulated band gap (7.39 eV) compared to the one from Whited and Walker (1969) (~7.8 V) supports the applicability of the used $E_0/1.5$ ratio. Our data is generally consistent with the increasing trend predicted by density functional theory (DFT) calculations (**Figure 2-6**), although DFT tentatively plots at lower energies. This discrepancy in absolute value is likely due to the tendency of DFT to underestimate the band gap (Winkler and Milman, 2014; Morales-García et al., 2017). Nevertheless, in the absence of direct band gap measurements at high-pressure conditions, the single-effective oscillator analysis after Wemple and DiDomenico (1971) presents a reasonable, semi-quantitative way to determine the optical band gap.

5.1.2 (Mg,Fe)O

Chapter 3 contains an analysis of the refractive index of ferropericlase, which has been submitted to *American Mineralogist*. This work presents the first in-situ experimental data on the optical refractive index and wavelength-dispersion of ferropericlase, and is presented together with an in-situ, thickness-based analysis of the optical absorption coefficient up to ~140 GPa at room temperature. Refractive index and absorption coefficient show an increase with pressure in the high-spin state (P < 50 GPa). Over the MS region, the index dispersion decreases by a factor of three, and the absorption coefficient deceases by ~30%. The refractive index at 600 nm is not significantly affected by the spin transition. The semi-quantitative estimation of the optical band gap (**Figure 3-5**) indicates its significant increase in the MS region. We interpret these anomalies as a reduction of small polaron transport between Fe-pairs of opposite spin, which may offer an explanation for the previously observed lower electrical conductivity of ferropericlase in the 50 to 70 GPa region (Lin et al., 2007b; Ohta et al., 2007).

As shown in **Figure 3-2**, the refractive index of (Mg,Fe)O at 600 nm increases with pressure and is not significantly altered by the expected spin transition. One of the runs (Fp13 100 run 3) was possibly influenced by small impurities that increased the apparent $R_{dia\text{-}smp}$, affecting the calculation of the refractive index. Nevertheless, extrapolations of the high-pressure data from Fp13 100 run 1 and Fp 24 100 run 1 to 1 atm are in excellent agreement with expectations from literature (Henning et al., 1995).

Compared to MgO, the index of (Mg,Fe)O is significantly higher, due to the relation between the refractive index and the electronic polarizability (via the dielectric constant: $\kappa = n^2$, which in turn is related to the polarizability via the electric displacement D and electric field strength E (Hynes, 2016)). The high refractive index of ferropericlase is a result of the higher polarizability of $^{[6]}Fe^{2+}$ compared to $^{[6]}Mg^{2+}$ (Shannon and Fischer, 2016). The addition of Fe to MgO apparently changes the sign of the pressure dependence of the refractive index from negative (MgO) to positive (ferropericlase) (**Figure 3-2**, **Figure 2-2**). We proposed

that the positive pressure dependence of the refractive index in ferropericlase is due to a high polarizability resulting from the presence of iron above the percolation limit (12%; Lorenz and Ziff, 1998) and associated with electron localization along hybridized t_{2g}-t_{2g} orbitals between adjacent Fe sites (Diamond et al., 2022). In the LS state, the reduction of electron density along the t_{2g}-t_{2g} joints (Diamond et al., 2022) may explain the near pressure-independent refractive index of ferropericlase, similar to MgO. This difference in orbital hybridization between ferropericlase and periclase could also explain the notable discrepancy between experimental data and the DFT results (pink and red lines in **Figure 3-2**). The computed models represent a low Fe concentration (3.2%), which is well below the percolation limit (Lorenz and Ziff, 1998). Consequently, the Fe-Fe interactions are either weak or absent, indicating that the refractive index of low-Fe ferropericlase decreases with pressure, similar to MgO.

We showed that the absorption coefficient of ferropericlase at 600 nm increases significantly with pressure in the high-spin state. Although the data in **Figure 3-3** reflects only a single-wavelength absorption coefficient, the in-situ thickness determination enabled scaling of previously published data to areas, where no direct thickness measurements have been reported (e.g., **Appendix Figure B 3**). At approximately 60 (±10) GPa, the absorption coefficient reaches its maximum, followed by a continuous decrease up to ~90 GPa. This change in trend was assigned to the spin transition in ferropericlase and is consistent with the expected onset of the spin transition at 13% iron content (Lin et al., 2006; Kantor et al., 2009; Glazyrin et al., 2016). Because one of the absorption bands of low-spin ferropericlase is located at ~600 nm ($^1A_{1g}$ to $^1T_{2g}$; see Schifferle and Lobanov, 2022) the absorption coefficient should increase at this wavelength. However, we observed a decrease in absorption coefficient at 600 nm across the spin transition. We proposed that the decrease in the absorption coefficient with the transition to the LS state is related to the previously reported blue-shift of the high-frequency absorption edge (Goncharov et al., 2006; Keppler et al., 2007; Schifferle and Lobanov, 2022). The plateau observed in the absorption coefficient at P > ~90 GPa implies that the tail of the high-frequency absorption edge no longer contributes to the absorption coefficient at 600 nm. Our results indicate a (room temperature) absorption coefficient that is up to 50% lower than previously reported (Lobanov et al., 2021). It is important to note that the effect of temperature on increasing opacity of ferropericlase is considerable (Lobanov et al., 2021). Therefore, bridgmanite remains the more transparent mineral in the lower mantle. Nevertheless, based on the absorption coefficients for ferropericlase presented in this study, future publications can calculate more accurate radiative conductivities for the lower mantle.

Previous studies reported a distinct decrease of the electrical conductivity of ferropericlase once the transition to the low-spin state is initiated (Lin et al., 2007b; Ohta et al., 2007; Yoshino et al., 2011). This reduction was previously assigned to a lowered small polaron mobility in LS ferropericlase (Lin et al., 2007b; Ohta et al., 2007). Although such an interpretation agrees with the low increase of electrical conductivity with pressure in Ohta et al. (2007), it does not explain the positive trend in conductivity with pressure at P > 80 GPa in Lin et al. (2007b), which is nearly identical to the one in full HS (between 20 and 50 GPa). Similar observations were also made by Liu et al. (2018) on the Fe^{3+} spin transition in $(Mg_{0.56}Fe_{0.53})(Si_{0.49}Fe_{0.51})O_3$

(bridgmanite), where in the MS region the electrical conductivity is reduced, but the effect of pressure on the electrical conductivity is nearly identical for full HS and full LS state. On the contrary, Ohta et al. (2010) reported a strong reduction in the MS region and a near pressure-independent electrical conductivity for full LS $(Mg_{0.9}Fe_{0.1})SiO_3$ bridgmanite. These full LS state discrepancies in both ferropericlase and bridgmanite call for a re-analysis of samples with identical compositions to resolve the effect of pressure on the electrical conductivity at these high-pressure conditions. The common feature in previous reports (Lin et al., 2007b; Ohta et al., 2007; Yoshino et al., 2011; Liu et al., 2018) is that there is a reduction of electrical conductivity in the presence of a MS composition. In Chapter 3, we present an alternative explanation for the observed reduction of the electrical conductivity. The single-effective oscillator analysis strongly indicates a significant increase of the optical band gap in MS ferropericlase (**Figure 3-5**). Although the band gap was not directly measured, the $E_0/3.8$ ratio increases up to a factor of 1.7 in the MS state and is then gradually restored to its base value up to ~100 GPa. This implies that a reduction of the small polaron mobility is particularly pronounced in the MS state, whereas small polaron mobility in full HS and full LS state remains comparable. Strong magnetic coupling between adjacent iron sites could represent a potential explanation for the observed changes in the mixed spin state, because it can relax spectroscopic selection rules and enhances the absorption coefficient and electron exchange between adjacent iron sites (Sherman and Waite, 1985, shown for Fe^{3+}). The relaxation of the selection rules, however, is only possible for HS-HS pairs. The spin transition-related magnetic collapse (Cohen et al., 1997) and consequently the obliteration of the magnetic selection rule relaxation is then consistent with the observed reduction of both the absorption coefficient (**Figure 3-3**) and the previously reported decrease of electrical conductivity (Lin et al., 2007b; Ohta et al., 2007; Yoshino et al., 2011). Nevertheless, it remains unclear why the relatively high wavelength-dispersion of the refractive index is restored in LS ferropericlase (**Figure 3-4**).

5.1.3 Limitations and outlook

The independence of the refractive index of diamond (n_{dia} = 2.418; Hynes, 2016) up to 140 GPa was a key assumption throughout Chapter 2 and Chapter 3. Although this assumption is supported by our own $\frac{d\rho}{dP}$ data on MgO (**Figure 2-4**), other authors suggested that n_{dia} might increase with pressure by ~2% (Katagiri et al., 2020) or decrease by up to 5% (Eremets et al., 1992; Morales-García et al., 2017) in the 0–140 GPa range. For MgO, such differences in n_{dia} would significantly affect its refractive index. However, within their 1σ uncertainty, Katagiri et al. (2020) could not rule out that the refractive index of diamond stays constant up to 140 GPa. DFT computations by Surh et al. (1992) suggested that the pressure dependence of the refractive index of diamond might either be positive or negative, depending on the principal strain direction. As the diamond tip deforms non-isotropically under pressure (i.e., complex diamond cupping; e.g., Merkel et al., 1999), the net effect could result in an essentially pressure-independent refractive index of diamond. Likewise, the reproducibility of the refractive index-based volume-density data of SiO_2 glass and H_2O (Zha et al., 2007; Lobanov et al., 2022) strongly supports a pressure-independent refractive index of diamond. Still, we could not completely rule out a significant change of n_{dia} with pressure (i.e., > ±1–2% up to

140 GPa). In that regard, I emphasize that the measured reflectances of the diamond-sample interface ($R_{dia\text{-}smp}$) are robust and reported in the manuscripts and this thesis (Appendix A for Chapter 2 and Appendix B for Chapter 3). These data will serve to re-evaluate the refractive indices of these materials, should this be needed when better knowledge on n_{dia} at high-pressure conditions becomes available.

In both studies on the refractive index, no pressure-transmitting medium was used. Instead, the sample was contained within a Re gasket, where stress conditions in the sample were determined by the mechanical strength of Re, which is considerably higher compared to a typical pressure-transmitting medium (e.g., Ar, Ne). Consequently, possible pressure and strain gradients could have been much higher compared to experiments that use a pressure transmitting medium. It is noted that within the error of the diamond anvil Raman gauge (5%, Akahama and Kawamura, 2006), no pressure gradients could be resolved. Given the reproducibility within 3% of the equation-of-state of MgO from Tange et al. (2009) (**Figure 2-4**), the agreement of modelled vs. experimental data (**Figure 2-2**), and the relatively small influence of P on n, we concluded that for MgO and (Mg,Fe)O the uniaxial stress conditions did not affect our results. However, future experiments should include measurements using pressure transmitting mediums, as this would allow to resolve the refractive index at pressures < 30 GPa.

As there are still uncertainties remaining, especially with regard to the index dispersion, future studies should particularly focus on the LS region and use additional sample compositions to further elucidate the cause of the high degree of refractive index dispersion. As most of the lower mantle at depths greater than ~1900 km is likely in MS state (Holmström and Stixrude, 2015), a broader variety of sample compositions might also serve to better constrain the maintained high polarizability of (Mg,Fe)O as well as the influence of magnetic coupling on the selection rules.

In high-pressure studies such as these, diamond cupping causes non-parallelism of the two diamond culets. Therefore, potential effects on the results have to be considered. Although the probe diameter is small (~5 μm in the focal plane), it is not possible to fully rule out an influence of diamond cupping. To this end, the usage of designer anvils with toroidal shape could potentially reduce the cupping (Dewaele et al., 2018) and improve the applicability of the single-effective oscillator analysis at extreme pressure conditions.

5.2 Chemical bonding in ferropericlase

In Chapter 4, the high-pressure optical properties of ferropericlase were used to analyze changes in the chemical bonding due to pressure and the spin transition. An examination of the chemical bonding is vitally important for the understanding of changes in chemical and physical material properties at extreme pressure conditions (Thomann, 1987; Cammarata and Rondinelli, 2012; Chainani et al., 2013; Mohn and Trønnes, 2016). We presented the first comprehensive analysis of the change in Fe-O bonding in ferropericlase, both with increasing pressure and across the spin transition. The usage of Tanabe-Sugano diagram fits (Tanabe and Sugano, 1954) allowed to analyze data from optical spectroscopy as well as to re-analyze previously published partial fluorescence yield X-ray absorption spectroscopy data (Lin et al., 2010). Furthermore, this

approach enabled us to extract ligand field splitting energy (10*Dq*) and Racah *B* parameter. The latter is a measure of the interelectronic repulsion and is considered a relative indicator of the covalency of a cation-anion bond within a crystal (Manning, 1970; Burns, 1993). In **Figure 4-5**, the Racah *B* parameter is plotted against pressure and compared to previous data of Keppler et al. (2007) and Goncharov et al. (2006). It is noted that the estimated Racah *B* parameter deviates significantly from the previously published data of Keppler et al. (2007). However, our data align perfectly with the Racah *B* parameter reported by Goncharov et al. (2006), as well as further datapoints extracted from their supporting materials. The discrepancy to the data of Keppler et al. (2007) may be attributed to the experimental uncertainties in peak position extraction. In contrast to Keppler et al. (2007), we analyzed a much broader spectral range, enabling a simultaneous three-peak-fit to the Tanabe-Sugano diagram (compared to the two in Keppler et al., 2007), which significantly reduces the influence of experimental uncertainty on the extracted Racah *B* value.

We showed that the Racah *B* parameter decreases with pressure in the HS state, indicating an increasing covalency of the Fe-O bond (consistent with previous data; Drickamer and Frank, 1973; Abu-Eid and Burns, 1976; Burns, 1993), whereas in the LS state the opposite trend was found. The change in covalency arises from the redistribution of electron density due to the spin transition, together with the shift from σ- to π-bonding, which affects overall interelectronic repulsion and potentially reduces the bond-dissociation energies between Fe and O. However, a comparison with pressure-related trends in other physical properties, such as bulk modulus (Wentzcovitch et al., 2009; Marquardt et al., 2018) or Fe diffusivity (Ammann et al., 2011; Saha et al., 2011; Saha et al., 2013), showed that the net effects of the bond strength reduction from HS to LS are minor and so far, no significant effect on other physical properties could be found.

By monitoring 10*Dq* and Racah *B* we concluded that the spin transition in ferropericlase can be attributed to both the increase in 10*Dq* and the decrease in Racah *B*. This is fundamentally different to the spin transition in siderite, which is governed by the steep increase in 10*Dq* (Lobanov et al., 2015) as depicted in **Figure 4-7**. This disparity results from the different crystal structure of the two minerals. Ferropericlase exhibits edge-shared octahedra, whereas siderite hosts corner-shared FeO_6 octahedra. The different structures cause variations in the sharing of electron density between Fe and O, ultimately resulting in a stronger effect of pressure on 10*Dq* in siderite compared to ferropericlase. This is also consistent with the higher Racah *B* parameter in siderite (Lobanov et al., 2015) compared to ferropericlase.

In Chapter 4 we showed how the optical properties at high pressure, specifically the absorbance, can be used to extract information on the response of chemical bonding to high-pressure conditions. However, it is noted that for achieving accurate results, an instrumental system optimized for wide-range measurements is required. This is particularly important when differences between electronic state energies are either small or their pressure shift is nearly identical. To this end, the (theoretical) ability to observe a higher number of electronic transitions can significantly improve the reliability of the fit.

5.3 Conclusion

The studies presented in this thesis significantly contribute to the deeper understanding of the optical properties of MgO and (Mg,Fe)O at high pressure. I extended the knowledge on the refractive index of the system Mg-Fe-O, and shed light on the evolution of chemical bonding under pressure conditions of the deep Earth. The experimental constraints on the evolution of the band gap for MgO and (Mg,Fe)O at mantle pressures were linked to their electrical conductivity and provided valuable insights into the physical properties of these important planetary building blocks (O'Neill and Jeanloz, 1990; McWilliams et al., 2012; Musella et al., 2019). Furthermore, my results contributed to the refinement of sound velocities and elastic constants (Zhang et al., 2023) and are of practical use to the high-pressure community, as the pressure dependence of the refractive index for MgO and (Mg,Fe)O allows for direct thickness estimation in DAC experiments (Lobanov and Geballe, 2022). The determination of optical properties, as demonstrated in this thesis, can be readily applied to other materials in order to deepen our knowledge of physical properties of geomaterials.

Chapter 6 References

Abu-Eid, R.M., & Burns, R.G. (1976): The effect of pressure on the degree of covalency of the cation-oxygen bond in minerals. *Am. Mineral.*, 61, 391–397.

Akahama, Y., & Kawamura, H. (2006): Pressure calibration of diamond anvil Raman gauge to 310 GPa. *J. Appl. Phys.*, 100, 43516, doi: 10.1063/1.2335683.

Alvaro, M., Angel, R.J. and Nestola, F. (2022): Inclusions in diamonds probe Earth's chemistry through deep time. *Commun. Chem.*, 5, 10, doi: 10.1038/s42004-022-00627-1.

Ammann, M.W., Brodholt, J.P. and Dobson, D.P. (2011): Ferrous iron diffusion in ferro-periclase across the spin transition. *Earth Planet. Sci. Lett.*, 302, 393–402, doi: 10.1016/j.epsl.2010.12.031.

Badro, J., Fiquet, G., Guyot, F. and Rueff, J.-P., et al. (2003): Iron partitioning in Earth's mantle: toward a deep lower mantle discontinuity. *Science*, 300, 789–791, doi: 10.1126/science.1081311.

Ballaran, T.B., Kurnosov, A., Glazyrin, K. and Frost, D.J., et al. (2012): Effect of chemistry on the compressibility of silicate perovskite in the lower mantle. *Earth Planet. Sci. Lett.*, 333-334, 181–190, doi: 10.1016/j.epsl.2012.03.029.

Balzaretti, N.M., & Da Jornada, J.A.H. (1990): Volume dependence of the electronic polarizability of magnesium oxide. *High Pressure Res.*, 2, 183–191, doi: 10.1080/08957959008201037.

Belonoshko, A.B., Arapan, S., Martonak, R. and Rosengren, A. (2010): MgO phase diagram from first principles in a wide pressure-temperature range. *Phys. Rev. B*, 81, doi: 10.1103/physrevb.81.054110.

Benedetti, L.R., & Loubeyre, P. (2004): Temperature gradients, wavelength-dependent emissivity, and accuracy of high and very-high temperatures measured in the laser-heated diamond cell. *High Pressure Res.*, 24, 423–445, doi: 10.1080/08957950412331331718.

Bengtson, A., Persson, K. and Morgan, D. (2008): Ab initio study of the composition dependence of the pressure-induced spin crossover in perovskite $(Mg_{1-x},Fe_x)SiO_3$. *Earth Planet. Sci. Lett.*, 265, 535–545, doi: 10.1016/j.epsl.2007.10.049.

Buchen, J., Marquardt, H., Speziale, S. and Kawazoe, T., et al. (2018): High-pressure single-crystal elasticity of wadsleyite and the seismic signature of water in the shallow transition zone. *Earth Planet. Sci. Lett.*, 498, 77–87, doi: 10.1016/j.epsl.2018.06.027.

Burns, R.G. (1993): Mineralogical Applications of Crystal Field Theory, Cambridge Topics in Mineral Physics and Chemistry, vol. 5, 2nd ed., 551 p., Cambridge University Press: Cambridge.

Cammarata, A., & Rondinelli, J.M. (2012): Spin-assisted covalent bond mechanism in "charge-ordering" perovskite oxides. *Phys. Rev. B*, 86, doi: 10.1103/PhysRevB.86.195144.

Catalli, K., Shim, S.-H., Dera, P. and Prakapenka, V.B., et al. (2011): Effects of the Fe^{3+} spin transition on the properties of aluminous perovskite — New insights for lower-mantle seismic heterogeneities. *Earth Planet. Sci. Lett.*, 310, 293–302, doi: 10.1016/j.epsl.2011.08.018.

Catalli, K., Shim, S.-H., Prakapenka, V.B. and Zhao, J., et al. (2010): Spin state of ferric iron in $MgSiO_3$ perovskite and its effect on elastic properties. *Earth Planet. Sci. Lett.*, 289, 68–75, doi: 10.1016/j.epsl.2009.10.029.

Cerantola, V., Bykova, E., Kupenko, I. and Merlini, M., et al. (2017): Stability of iron-bearing carbonates in the deep Earth's interior. *Nat. Commun.*, 8, 15960, doi: 10.1038/ncomms15960.

Chainani, A., Yamamoto, A., Matsunami, M. and Eguchi, R., et al. (2013): Quantifying covalency and metallicity in correlated compounds undergoing metal-insulator transitions. *Phys. Rev. B*, 87, doi: 10.1103/PhysRevB.87.045108.

Clark, S.P. (1957): Radiative transfer in the Earth's mantle. *Trans. AGU*, 38, 931, doi: 10.1029/TR038i006p00931.

Clarke, J.W., McDowell, R.C., Matzko, J.R., and Hearn, P.P., et al. (1986): The Kola superdeep drill hole: A detailed summary by Ye. A. Kozlovskiy. Open File Report 86-517.

Cohen, R.E., Mazin, I.I. and Isaak, D.G. (1997): Magnetic collapse in transition metal oxides at high pressure: Implications for the Earth. *Science*, 275, 654–657, doi: 10.1126/science.275.5300.654.

Coppari, F., Smith, R.F., Wang, J. and Millot, M., et al. (2021): Implications of the iron oxide phase transition on the interiors of rocky exoplanets. *Nat. Geosci.*, 14, 121–126, doi: 10.1038/s41561-020-00684-y.

Crowhurst, J.C., Brown, J.M., Goncharov, A.F. and Jacobsen, S.D. (2008): Elasticity of (Mg,Fe)O through the spin transition of iron in the lower mantle. *Science*, 319, 451–453, doi: 10.1126/science.1149606.

Deng, J., & Lee, K.K.M. (2017): Viscosity jump in the lower mantle inferred from melting curves of ferropericlase. *Nat. Commun.*, 8, 1997, doi: 10.1038/s41467-017-02263-z.

Dewaele, A., Loubeyre, P., Occelli, F. and Marie, O., et al. (2018): Toroidal diamond anvil cell for detailed measurements under extreme static pressures. *Nat. Commun.*, 9, 2913, doi: 10.1038/s41467-018-05294-2.

Diamond, M.R., Shen, G., Popov, D.Y. and Park, C., et al. (2022): Electron density changes across the pressure-induced iron spin transition. *Phys. Rev. Lett.*, 129, 25701, doi: 10.1103/PhysRevLett.129.025701.

Dorfman, S.M., Badro, J., Rueff, J.-P. and Chow, P., et al. (2015): Composition dependence of spin transition in (Mg,Fe)SiO_3 bridgmanite. *Am. Mineral.*, 100, 2246–2253, doi: 10.2138/am-2015-5190.

Drickamer, H.G., and Frank, C.W. (1973): Electronic Transitions and the High Pressure Chemistry and Physics of Solids, Studies in Chemical Physics, 220 p., Springer: Dordrecht.

Dubrovinsky, L., Dubrovinskaia, N., Bykova, E. and Bykov, M., et al. (2015): The most incompressible metal osmium at static pressures above 750 gigapascals. *Nature*, 525, 226–229, doi: 10.1038/nature14681.

Eremets, M.I., Struzhkin, V.V., Timofeev, J.A. and Trojan, I.A., et al. (1992): Refractive index of diamond under pressure. *High Pressure Res.*, 9, 347–350, doi: 10.1080/08957959208245659.

Fratanduono, D.E., Eggert, J.H., Akin, M.C. and Chau, R., et al. (2013): A novel approach to Hugoniot measurements utilizing transparent crystals. *J. Appl. Phys.*, 114, 43518, doi: 10.1063/1.4813871.

Fyfe, W. (1960): The possibility of *d*-electron coupling in olivine at high pressures. *Geochim. Cosmochim. Acta*, 19, 141–143, doi: 10.1016/0016-7037(60)90046-6.

Geballe, Z.M., Sime, N., Badro, J. and Van Keken, P.E., et al. (2020): Thermal conductivity near the bottom of the Earth's lower mantle: Measurements of pyrolite up to 120 GPa and 2500 K. *Earth Planet. Sci. Lett.*, 536, 116161, doi: 10.1016/j.epsl.2020.116161.

Glazyrin, K., Miyajima, N., Smith, J.S. and Lee, K.K.M. (2016): Compression of a multiphase mantle assemblage: Effects of undesirable stress and stress annealing on the iron spin state crossover in ferropericlase. *J. Geophys. Res.: Solid Earth*, 121, 3377–3392, doi: 10.1002/2015JB012321.

Goncharov, A.F., Beck, P., Struzhkin, V.V. and Haugen, B.D., et al. (2009): Thermal conductivity of lower-mantle minerals. *Phys. Earth Planet. Inter.*, 174, 24–32, doi: 10.1016/j.pepi.2008.07.033.

Goncharov, A.F., Lobanov, S.S., Tan, X. and Hohensee, G.T., et al. (2015): Experimental study of thermal conductivity at high pressures: Implications for the deep Earth's interior. *Phys. Earth Planet. Inter.*, 247, 11–16, doi: 10.1016/j.pepi.2015.02.004.

Goncharov, A.F., Struzhkin, V.V. and Jacobsen, S.D. (2006): Reduced radiative conductivity of low-spin (Mg,Fe)O in the lower mantle. *Science*, 312, 1205–1208, doi: 10.1126/science.1125622.

Goto, T., Ahrens, T.J., Rossman, G.R. and Syono, Y. (1980): Absorption spectrum of shock-compressed Fe^{2+}-bearing MgO and the radiative conductivity of the lower mantle. *Phys. Earth Planet. Inter.*, 22, 272–276, doi: 10.1016/0031-9201(80)90044-8.

Hamada, M., Kamada, S., Ohtani, E. and Sakamaki, T., et al. (2021): Synchrotron Mössbauer spectroscopic and x-ray diffraction study of ferropericlase in the high-pressure range of the lower mantle region. *Phys. Rev. B*, 103, doi: 10.1103/PhysRevB.103.174108.

Hazen, R.M. (1976): Effects of temperature and pressure on the cell dimension and X-ray temperature factors of periclase. *Am. Mineral.*, 61, 266–271.

Henning, T., Begemann, B., Mutschke, H. and Dorschner, J. (1995): Optical properties of oxide dust grains. *Astron. Astrophys. Suppl. Ser.*, 112, 143–149.

Higo, Y., Inoue, T., Li, B. and Irifune, T., et al. (2006): The effect of iron on the elastic properties of ringwoodite at high pressure. *Phys. Earth Planet. Inter.*, 159, 276–285, doi: 10.1016/j.pepi.2006.08.004.

Holmström, E., & Stixrude, L. (2015): Spin crossover in ferropericlase from first-principles molecular dynamics. *Phys. Rev. Lett.*, 114, 117202, doi: 10.1103/PhysRevLett.114.117202.

Hsieh, W.-P., Deschamps, F., Okuchi, T. and Lin, J.-F. (2018): Effects of iron on the lattice thermal conductivity of Earth's deep mantle and implications for mantle dynamics. *Proc. Natl. Acad. Sci. U.S.A.*, 115, 4099–4104, doi: 10.1073/pnas.1718557115.

Hsu, H., Blaha, P., Cococcioni, M. and Wentzcovitch, R.M. (2011a): Spin-state crossover and hyperfine interactions of ferric iron in $MgSiO_3$ perovskite. *Phys. Rev. Lett.*, 106, 118501, doi: 10.1103/PhysRevLett.106.118501.

Hsu, H., Umemoto, K., Cococcioni, M. and Wentzcovitch, R.M. (2011b): The Hubbard U correction for iron-bearing minerals: A discussion based on $(Mg,Fe)SiO_3$ perovskite. *Phys. Earth Planet. Inter.*, 185, 13–19, doi: 10.1016/j.pepi.2010.12.001.

Hynes, W.M. (2016): CRC Handbook of Chemistry and Physics, 97th ed., CRC Press: Boca Raton, London, New York.

Irifune, T., & Tsuchiya, T. (2015): Phase transitions and mineralogy of the lower mantle. In G. Schubert, Ed., Treatise on Geophysics, 2nd ed., 33–60, Elsevier, Oxford.

Justo, J.F., Morra, G. and Yuen, D.A. (2015): Viscosity undulations in the lower mantle: The dynamical role of iron spin transition. *Earth Planet. Sci. Lett.*, 421, 20–26, doi: 10.1016/j.epsl.2015.03.013.

Kantor, I., Dubrovinsky, L.S., McCammon, C.A. and Steinle-Neumann, G., et al. (2009): Short-range order and Fe clustering in $Mg_{1-x}Fe_xO$ under high pressure. *Phys. Rev. B*, 80, doi: 10.1103/PhysRevB.80.014204.

Katagiri, K., Ozaki, N., Miyanishi, K. and Kamimura, N., et al. (2020): Optical properties of shock-compressed diamond up to 550 GPa. *Phys. Rev. B*, 101, doi: 10.1103/PhysRevB.101.184106.

Keppler, H., Dubrovinsky, L.S., Narygina, O. and Kantor, I. (2008): Optical absorption and radiative thermal conductivity of silicate perovskite to 125 gigapascals. *Science*, 322, 1529–1532, doi: 10.1126/science.1164609.

Keppler, H., Kantor, I. and Dubrovinsky, L.S. (2007): Optical absorption spectra of ferropericlase to 84 GPa. *Am. Mineral.*, 92, 433–436, doi: 10.2138/am.2007.2454.

Konôpková, Z., McWilliams, R.S., Gómez-Pérez, N. and Goncharov, A.F. (2016): Direct measurement of thermal conductivity in solid iron at planetary core conditions. *Nature*, 534, 99–101, doi: 10.1038/nature18009.

Kupenko, I., McCammon, C., Sinmyo, R. and Cerantola, V., et al. (2015): Oxidation state of the lower mantle: In situ observations of the iron electronic configuration in bridgmanite at extreme conditions. *Earth Planet. Sci. Lett.*, 423, 78–86, doi: 10.1016/j.epsl.2015.04.027.

Lauterbach, S., McCammon, C.A., van Aken, P. and Langenhorst, F., et al. (2000): Mössbauer and ELNES spectroscopy of $(Mg,Fe)(Si,Al)O_3$ perovskite: a highly oxidised component of the lower mantle. *Contrib. Mineral. Petrol.*, 138, 17–26, doi: 10.1007/PL00007658.

Lin, J.-F., Gavriliuk, A.G., Struzhkin, V.V. and Jacobsen, S.D., et al. (2006): Pressure-induced electronic spin transition of iron in magnesiowustite-(Mg,Fe)O. *Am. Mineral.*, 73, 794, doi: 10.1103/PhysRevB.73.113107.

Lin, J.-F., Mao, Z., Jarrige, I. and Xiao, Y., et al. (2010): Resonant X-ray emission study of the lower-mantle ferropericlase at high pressures. *Am. Mineral.*, 95, 1125–1131, doi: 10.2138/am.2010.3495.

Lin, J.-F., Mao, Z., Yang, J. and Liu, J., et al. (2016): High-spin Fe^{2+} and Fe^{3+} in single-crystal aluminous bridgmanite in the lower mantle. *Geophys. Res. Lett.*, 43, 6952–6959, doi: 10.1002/2016GL069836.

Lin, J.-F., Speziale, S., Mao, Z. and Marquardt, H. (2013): Effects of the electronic spin transitions of iron in lower mantle minerals: Implications for deep mantle geophysics and geochemistry. *Rev. Geophys.*, 51, 244–275, doi: 10.1002/rog.20010.

Lin, J.-F., Struzhkin, V.V., Jacobsen, S.D. and Hu, M.Y., et al. (2005): Spin transition of iron in magnesiowüstite in the Earth's lower mantle. *Nature*, 436, 377–380, doi: 10.1038/nature03825.

Lin, J.-F., & Tsuchiya, T. (2008): Spin transition of iron in the Earth's lower mantle. *Phys. Earth Planet. Inter.*, 170, 248–259, doi: 10.1016/j.pepi.2008.01.005.

Lin, J.-F., Vankó, G., Jacobsen, S.D. and Iota, V., et al. (2007a): Spin transition zone in Earth's lower mantle. *Science*, 317, 1740–1743, doi: 10.1126/science.1144997.

Lin, J.-F., Weir, S.T., Jackson, D.D. and Evans, W.J., et al. (2007b): Electrical conductivity of the lower-mantle ferropericlase across the electronic spin transition. *Geophys. Res. Lett.*, 34, doi: 10.1029/2007GL030523.

Liu, J., Dorfman, S.M., Zhu, F. and Li, J., et al. (2018): Valence and spin states of iron are invisible in Earth's lower mantle. *Nat. Commun.*, 9, 1284, doi: 10.1038/s41467-018-03671-5.

Liu, Z.-J., Sun, X.-W., Zhang, C.-R. and Zhang, S.-J., et al. (2022): First-principles calculations of high-pressure physical properties anisotropy for magnesite. *Sci. Rep.*, 12, 3691, doi: 10.1038/s41598-022-07705-3.

Lobanov, S.S., & Geballe, Z.M. (2022): Non-isotropic contraction and expansion of samples in diamond anvil cells: Implications for thermal conductivity at the core-mantle boundary. *Geophys. Res. Lett.*, 49, e2022GL100379, doi: 10.1029/2022GL100379.

Lobanov, S.S., Goncharov, A.F. and Litasov, K.D. (2015): Optical properties of siderite ($FeCO_3$) across the spin transition: Crossover to iron-rich carbonates in the lower mantle. *Am. Mineral.*, 100, 1059–1064, doi: 10.2138/am-2015-5053.

Lobanov, S.S., Holtgrewe, N. and Goncharov, A.F. (2016): Reduced radiative conductivity of low spin FeO_6-octahedra in $FeCO_3$ at high pressure and temperature. *Earth Planet. Sci. Lett.*, 449, 20–25, doi: 10.1016/j.epsl.2016.05.028.

Lobanov, S.S., Holtgrewe, N., Ito, G. and Badro, J., et al. (2020): Blocked radiative heat transport in the hot pyrolitic lower mantle. *Earth Planet. Sci. Lett.*, 537, 116176, doi: 10.1016/j.epsl.2020.116176.

Lobanov, S.S., Holtgrewe, N., Lin, J.-F. and Goncharov, A.F. (2017a): Radiative conductivity and abundance of post-perovskite in the lowermost mantle. *Earth Planet. Sci. Lett.*, 479, 43–49, doi: 10.1016/j.epsl.2017.09.016.

Lobanov, S.S., Hsu, H., Lin, J.-F. and Yoshino, T., et al. (2017b): Optical signatures of low spin Fe^{3+} in NAL at high pressure. *J. Geophys. Res.: Solid Earth*, 122, 3565–3573, doi: 10.1002/2017JB014134.

Lobanov, S.S., Soubiran, F., Holtgrewe, N. and Badro, J., et al. (2021): Contrasting opacity of bridgmanite and ferropericlase in the lowermost mantle: Implications to radiative and electrical conductivity. *Earth Planet. Sci. Lett.*, 562, 116871, doi: 10.1016/j.epsl.2021.116871.

Lobanov, S.S., Speziale, S., Winkler, B. and Milman, V., et al. (2022): Electronic, structural, and mechanical properties of SiO_2 glass at high pressure inferred from its refractive index. *Phys. Rev. Lett.*, 128, 77403, doi: 10.1103/PhysRevLett.128.077403.

Lorenz, C.D., & Ziff, R.M. (1998): Precise determination of the bond percolation thresholds and finite-size scaling corrections for the sc, fcc, and bcc lattices. *Phys. Rev. E*, 57, 230–236, doi: 10.1103/PhysRevE.57.230.

Lyubutin, I.S., Struzhkin, V.V., Mironovich, A.A. and Gavriliuk, A.G., et al. (2013): Quantum critical point and spin fluctuations in lower-mantle ferropericlase. *Proc. Natl. Acad. Sci. U.S.A.*, 110, 7142–7147, doi: 10.1073/pnas.1304827110.

Manning, P.G. (1970): Racah parameters and their relationship to lengths and covalencies of Mn^{2+}- and Fe^{3+}-oxygen bonds in silicates. *Can. Mineral.*, 10, 677–688.

Mao, Z., Lin, J.-F., Yang, J. and Inoue, T., et al. (2015): Effects of the Fe^{3+} spin transition on the equation of state of bridgmanite. *Geophys. Res. Lett.*, 42, 4335–4342, doi: 10.1002/2015GL064400.

Marquardt, H., Buchen, J., Mendez, A.S.J. and Kurnosov, A., et al. (2018): Elastic softening of $(Mg_{0.8}Fe_{0.2})O$ ferropericlase across the iron spin crossover measured at seismic frequencies. *Geophys. Res. Lett.*, 45, 6862–6868, doi: 10.1029/2018GL077982.

Marquardt, H., & Miyagi, L. (2015): Slab stagnation in the shallow lower mantle linked to an increase in mantle viscosity. *Nat. Geosci.*, 8, 311–314, doi: 10.1038/ngeo2393.

Marquardt, H., Speziale, S., Reichmann, H.J. and Frost, D.J., et al. (2009): Single-crystal elasticity of $(Mg_{0.9}Fe_{0.1})O$ to 81 GPa. *Earth Planet. Sci. Lett.*, 287, 345–352, doi: 10.1016/j.epsl.2009.08.017.

McCammon, C. (1997): Perovskite as a possible sink for ferric iron in the lower mantle. *Nature*, 387, 694–696, doi: 10.1038/42685.

McCammon, C., Hutchison, M. and Harris, J. (1997): Ferric iron content of mineral inclusions in diamonds from São Luiz: A view into the lower mantle. *Science*, 278, 434–436, doi: 10.1126/science.278.5337.434.

McCammon, C., Kantor, I., Narygina, O. and Rouquette, J., et al. (2008): Stable intermediate-spin ferrous iron in lower-mantle perovskite. *Nat. Geosci.*, 1, 684–687, doi: 10.1038/ngeo309.

McCammon, C., Peyronneau, J. and Poirier, J.-P. (1998): Low ferric iron content of (Mg,Fe)O at high pressures and temperatures. *Geophys. Res. Lett.*, 25, 1589–1592, doi: 10.1029/98GL01178.

McDonough, W.F., & Sun, S. (1995): The composition of the Earth. *Chemical Geology*, 120, 223–253, doi: 10.1016/0009-2541(94)00140-4.

McWilliams, R.S., Spaulding, D.K., Eggert, J.H. and Celliers, P.M., et al. (2012): Phase transformations and metallization of magnesium oxide at high pressure and temperature. *Science*, 338, 1330–1333, doi: 10.1126/science.1229450.

Merkel, S., Hemley, R.J. and Mao, H.-K. (1999): Finite-element modeling of diamond deformation at multimegabar pressures. *Appl. Phys. Lett.*, 74, 656–658, doi: 10.1063/1.123031.

Mildren, R.P. (2013): Intrinsic optical properties of diamond. In R.P. Mildren and J.R. Rabeau, Eds., Optical Engineering of Diamond, 1–34, Wiley.

Mohn, C.E., & Trønnes, R.G. (2016): Iron spin state and site distribution in $FeAlO_3$-bearing bridgmanite. *Earth Planet. Sci. Lett.*, 440, 178–186, doi: 10.1016/j.epsl.2016.02.010.

Morales-García, Á., Valero, R. and Illas, F. (2017): An empirical, yet practical way to predict the band gap in solids by using density functional and structure calculations. *J. Phys. Chem. C*, 121, 18862–18866, doi: 10.1021/acs.jpcc.7b07421.

Mrosko, M., Koch-Müller, M., McCammon, C. and Rhede, D., et al. (2015): Water, iron, redox environment: effects on the wadsleyite–ringwoodite phase transition. *Contrib. Mineral. Petrol.*, 170, doi: 10.1007/s00410-015-1163-2.

Muir, J.M., & Brodholt, J.P. (2015): Elastic properties of ferropericlase at lower mantle conditions and its relevance to ULVZs. *Earth Planet. Sci. Lett.*, 417, 40–48, doi: 10.1016/j.epsl.2015.02.023.

Muir, J.M., & Brodholt, J.P. (2016): Ferrous iron partitioning in the lower mantle. *Phys. Earth Planet. Inter.*, 257, 12–17, doi: 10.1016/j.pepi.2016.05.008.

Murakami, M., Goncharov, A.F., Miyajima, N. and Yamazaki, D., et al. (2022): Radiative thermal conductivity of single-crystal bridgmanite at the core-mantle boundary with implications for thermal evolution of the Earth. *Earth Planet. Sci. Lett.*, 578, 117329, doi: 10.1016/j.epsl.2021.117329.

Musella, R., Mazevet, S. and Guyot, F. (2019): Physical properties of MgO at deep planetary conditions. *Phys. Rev. B*, 99, doi: 10.1103/PhysRevB.99.064110.

Nakatsuka, A., Fukui, H., Kamada, S. and Hirao, N., et al. (2021): Incorporation mechanism of Fe and Al into bridgmanite in a subducting mid-ocean ridge basalt and its crystal chemistry. *Sci. Rep.*, 11, 22839, doi: 10.1038/s41598-021-00403-6.

Oganov, A.R., Gillan, M.J. and Price, G.D. (2003): Ab initio lattice dynamics and structural stability of MgO. *J. Chem. Phys.*, 118, 10174–10182, doi: 10.1063/1.1570394.

Ohta, K., Hirose, K., Onoda, S. and Shimizu, K. (2007): The effect of iron spin transition on electrical conductivity of (Mg,Fe)O magnesiowüstite. *Proc. Jpn. Acad. Ser. B Phys. Biol. Sci.*, 83, 97–100, doi: 10.2183/pjab.83.97.

Ohta, K., Hirose, K., Shimizu, K. and Sata, N., et al. (2010): The electrical resistance measurements of (Mg,Fe)SiO3 perovskite at high pressures and implications for electronic spin transition of iron. *Phys. Earth Planet. Inter.*, 180, 154–158, doi: 10.1016/j.pepi.2009.11.002.

Ohta, K., Kuwayama, Y., Hirose, K. and Shimizu, K., et al. (2016): Experimental determination of the electrical resistivity of iron at Earth's core conditions. *Nature*, 534, 95–98, doi: 10.1038/nature17957.

Ohta, K., Yagi, T., Hirose, K. and Ohishi, Y. (2017): Thermal conductivity of ferropericlase in the Earth's lower mantle. *Earth Planet. Sci. Lett.*, 465, 29–37, doi: 10.1016/j.epsl.2017.02.030.

Okuda, Y., Ohta, K., Hasegawa, A. and Yagi, T., et al. (2020a): Thermal conductivity of Fe-bearing post-perovskite in the Earth's lowermost mantle. *Earth Planet. Sci. Lett.*, 547, 116466, doi: 10.1016/j.epsl.2020.116466.

Okuda, Y., Ohta, K., Sinmyo, R. and Hirose, K., et al. (2020b): Anomalous compressibility in (Fe,Al)-bearing bridgmanite: implications for the spin state of iron. *Phys. Chem. Minerals.*, 47, doi: 10.1007/s00269-020-01109-3.

O'Neill, B., & Jeanloz, R. (1990): Experimental petrology of the lower mantle: a natural peridotite taken to 54 GPa. *Geophys. Res. Lett.*, 17, 1477–1480, doi: 10.1029/GL017i010p01477.

Otsuka, K., & Karato, S. (2015): The influence of ferric iron and hydrogen on Fe–Mg interdiffusion in ferropericlase ((Mg,Fe)O) in the lower mantle. *Phys. Chem. Minerals.*, 42, 261–273, doi: 10.1007/s00269-014-0717-6.

Pamato, M.G., Nestola, F., Novella, D. and Smyth, J.R., et al. (2019): The high-pressure structural evolution of olivine along the forsterite–fayalite join. *Minerals*, 9, 790, doi: 10.3390/min9120790.

Pigott, J.S., Ditmer, D.A., Fischer, R.A. and Reaman, D.M., et al. (2015): High-pressure, high-temperature equations of state using nanofabricated controlled-geometry Ni/SiO_2/Ni double hot-plate samples. *Geophys. Res. Lett.*, 42, doi: 10.1002/2015GL066577.

Potapkin, V., McCammon, C., Glazyrin, K. and Kantor, A., et al. (2013): Effect of iron oxidation state on the electrical conductivity of the Earth's lower mantle. *Nat. Commun.*, 4, doi: 10.1038/ncomms2436.

Prescher, C., Langenhorst, F., Dubrovinsky, L.S. and Prakapenka, V.B., et al. (2014): The effect of Fe spin crossovers on its partitioning behavior and oxidation state in a pyrolitic Earth's lower mantle system. *Earth Planet. Sci. Lett.*, 399, 86–91, doi: 10.1016/j.epsl.2014.05.011.

Reali, R., Jackson, J.M., Van Orman, J. and Bower, D.J., et al. (2019): Modeling viscosity of (Mg,Fe)O at lowermost mantle conditions. *Phys. Earth Planet. Inter.*, 287, 65–75, doi: 10.1016/j.pepi.2018.12.005.

Saha, S., Bengtson, A., Crispin, K.L. and Van Orman, J.A., et al. (2011): Effects of spin transition on diffusion of Fe^{2+} in ferropericlase in Earth's lower mantle. *Phys. Rev. B*, 84, doi: 10.1103/PhysRevB.84.184102.

Saha, S., Bengtson, A. and Morgan, D. (2013): Effect of anomalous compressibility on Fe diffusion in ferropericlase throughout the spin crossover in the lower mantle. *Earth Planet. Sci. Lett.*, 362, 1–5, doi: 10.1016/j.epsl.2012.11.032.

Schifferle, L., & Lobanov, S.S. (2022): Evolution of chemical bonding and spin-pairing energy in ferropericlase across its spin transition. *ACS Earth Space Chem.*, 6, 788–799, doi: 10.1021/acsearthspacechem.2c00014.

Schifferle, L., Speziale, S. and Lobanov, S.S. (2022): High-pressure evolution of the refractive index of MgO up to 140 GPa. *J. Appl. Phys.*, 132, 125903, doi: 10.1063/5.0106626.

Shaaker, H.S., Hussain, W.A. and Badra, H.A. (2012): Determination of the optical constants and optical limiting of doped malachite green thin films by the spray method. *Adv. Appl. Sci. Res. (Advances in Applied Science Research)*, 3, 2940–2946.

Shand, M.A. (2010): The chemistry and technology of magnesia, 266 p., Wiley-Interscience: Hoboken, N.J.

Shannon, R.D., & Fischer, R.X. (2016): Empirical electronic polarizabilities of ions for the prediction and interpretation of refractive indices: Oxides and oxysalts. *Am. Mineral.*, 101, 2288–2300, doi: 10.2138/am-2016-5730.

Shephard, G.E., Houser, C., Hernlund, J.W. and Valencia-Cardona, J.J., et al. (2021): Seismological expression of the iron spin crossover in ferropericlase in the Earth's lower mantle. *Nat. Commun.*, 12, 5905, doi: 10.1038/s41467-021-26115-z.

Sherman, D.M., & Waite, T.D. (1985): Electronic spectra of Fe^{3+} oxides and oxide hydroxides in the near IR to near UV. *Am. Mineral.*, 70, 1262–1269.

Solomatova, N.V., Jackson, J.M., Sturhahn, W. and Wicks, J.K., et al. (2016): Equation of state and spin crossover of (Mg,Fe)O at high pressure, with implications for explaining topographic relief at the core-mantle boundary. *Am. Mineral.*, 101, 1084–1093, doi: 10.2138/am-2016-5510.

Song, Y., He, K., Sun, J. and Ma, C., et al. (2019): Effects of iron spin transition on the electronic structure, thermal expansivity and lattice thermal conductivity of ferropericlase: a first principles study. *Sci. Rep.*, 9, 4172, doi: 10.1038/s41598-019-40454-4.

Soubiran, F., & Militzer, B. (2020): Anharmonicity and phase diagram of magnesium oxide in the megabar regime. *Phys. Rev. Lett.*, 125, 175701, doi: 10.1103/PhysRevLett.125.175701.

Spaargaren, R.J., Wang, H.S., Mojzsis, S.J. and Ballmer, M.D., et al. (2023): Plausible constraints on the range of bulk terrestrial exoplanet compositions in the solar neighborhood. *ApJ*, 948, 53, doi: 10.3847/1538-4357/acac7d.

Speziale, S., Milner, A., Lee, V.E. and Clark, S.M., et al. (2005): Iron spin transition in Earth's mantle. *Proc. Natl. Acad. Sci. U.S.A.*, 102, 17918–17922, doi: 10.1073/pnas.0508919102.

Stephens, R.E., & Malitson, I.H. (1952): Index of refraction of magnesium oxide. *J. Res. Natl. Bur. Stand.*, 49, 249–252, doi: 10.6028/jres.049.025.

Stevens, G.D., Veeser, L.R., Rigg, P.A. and Hixson, R.S. (2006): Suitability of magnesium oxide as a VISAR window. In M.D. Furnish, M. Elert, T.P. Russel and C.T. White, Eds., AIP conference proceedings 2272 A. Shock compression of condensed matter 2019: Proceedings of the conference of the American Physical Society topical group on shock compression of condensed matter, Baltimore, Maryland (USA), AIP, 1353–1356.

Studenyak, I.P., Bereznyuk, S.M., Pop, M.M. and Studenyak, V.I., et al. (2020): Influence of cation substitution on optical constants of $(Cu_{1-x}Ag_x)_7SiS_5I$ mixed crystals. *SPQEO*, 23, 186–192, doi: 10.15407/spqeo23.02.186.

Surh, M.P., Louie, S.G. and Cohen, M.L. (1992): Band gaps of diamond under anisotropic stress. *Phys. Rev. B Condens. Matter*, 45, 8239–8247, doi: 10.1103/PhysRevB.45.8239.

Tanabe, Y., & Sugano, S. (1954): On the absorption spectra of complex ions I. *J. Phys. Soc. Jpn.*, 9, 753–766, doi: 10.1143/JPSJ.9.753.

Tange, Y., Nishihara, Y. and Tsuchiya, T. (2009): Unified analyses for *P-V-T* equation of state of MgO: A solution for pressure-scale problems in high *P-T* experiments. *J. Geophys. Res.*, 114, B03208, doi: 10.1029/2008JB005813.

Thomann, H. (1987): A covalency model of ferroic phase transitions in perovskites. *Ferroelectrics*, 73, 183–199, doi: 10.1080/00150198708227917.

Tsuchiya, T., Wentzcovitch, R.M., Da Silva, C.R.S. and Gironcoli, S. de (2006): Spin transition in magnesiowüstite in Earth's lower mantle. *Phys. Rev. Lett.*, 96, 198501, doi: 10.1103/PhysRevLett.96.198501.

Vilella, K., Shim, S.-H., Farnetani, C.G. and Badro, J. (2015): Spin state transition and partitioning of iron: Effects on mantle dynamics. *Earth Planet. Sci. Lett.*, 417, 57–66, doi: 10.1016/j.epsl.2015.02.009.

Weir, C.E., Lippincott, E.R., Van Valkenburg, A. and Bunting, E.N. (1959): Infrared studies in the 1- to 15-micron region to 30,000 atmospheres. *J. Res. Natl. Bur. Stand. A Phys. Chem.*, 63A, 55–62, doi: 10.6028/jres.063A.003.

Wemple, S.H., & DiDomenico, M. (1971): Behavior of the electronic dielectric constant in covalent and ionic materials. *Phys. Rev. B*, 3, 1338–1351, doi: 10.1103/PhysRevB.3.1338.

Wentzcovitch, R.M., Justo, J.F., Wu, Z. and Da Silva, C.R.S., et al. (2009): Anomalous compressibility of ferropericlase throughout the iron spin cross-over. *Proc. Natl. Acad. Sci. U.S.A.*, 106, 8447–8452, doi: 10.1073/pnas.0812150106.

Whited, R.C., & Walker, W.C. (1969): Exciton spectra of CaO and MgO. *Phys. Rev. Lett.*, 22, 1428–1430, doi: 10.1103/PhysRevLett.22.1428.

Williams, Q., & Knittle, E. (1990): Structural and electronic properties of Fe_2SiO_4-fayalite at ultrahigh pressures: Amorphization and gap closure. *J. Geophys. Res.*, 95, 21549–21563.

Wilson, I.O. (1981): Magnesium oxide as a high-temperature insulant. *IEE Proc. A Phys. Sci. Meas. Instrum. Manage. Educ. Rev. UK*, 128, 159, doi: 10.1049/ip-a-1.1981.0026.

Winkler, B., & Milman, V. (2014): Density functional theory based calculations for high pressure research. *Z. Kristallogr. - Cryst. Mater.*, 229, doi: 10.1515/zkri-2013-1650.

Wu, Z., Justo, J.F. and Wentzcovitch, R.M. (2013): Elastic anomalies in a spin-crossover system: ferropericlase at lower mantle conditions. *Phys. Rev. Lett.*, 110, 228501, doi: 10.1103/PhysRevLett.110.228501.

Xu, S., Lin, J.-F. and Morgan, D. (2017): Iron partitioning between ferropericlase and bridgmanite in the Earth's lower mantle. *J. Geophys. Res.: Solid Earth*, 122, 1074–1087, doi: 10.1002/2016JB013543.

Yamazaki, D., & Karato, S. (2001): Some mineral physics constraints on the rheology and geothermal structure of Earth's lower mantle. *Am. Mineral.*, 86, 385–391, doi: 10.2138/am-2001-0401.

Yamazaki, D., Yoshino, T., Matsuzaki, T. and Katsura, T., et al. (2009): Texture of (Mg,Fe)SiO_3 perovskite and ferro-periclase aggregate: Implications for rheology of the lower mantle. *Phys. Earth Planet. Inter.*, 174, 138–144, doi: 10.1016/j.pepi.2008.11.002.

Yang, J., Tong, X., Lin, J.-F. and Okuchi, T., et al. (2015): Elasticity of ferropericlase across the spin crossover in the Earth's lower mantle. *Sci. Rep.*, 5, 17188, doi: 10.1038/srep17188.

Yoshino, T., Ito, E., Katsura, T. and Yamazaki, D., et al. (2011): Effect of iron content on electrical conductivity of ferropericlase with implications for the spin transition pressure. *J. Geophys. Res.*, 116, doi: 10.1029/2010JB007801.

Zha, C.S., Mao, H. and Hemley, R.J. (2000): Elasticity of MgO and a primary pressure scale to 55 GPa. *Proc. Natl. Acad. Sci. U.S.A.*, 97, 13494–13499, doi: 10.1073/pnas.240466697.

Zha, C.-S., Hemley, R.J., Gramsch, S.A. and Mao, H.-K., et al. (2007): Optical study of H_2O ice to 120 GPa: Dielectric function, molecular polarizability, and equation of state. *J. Chem. Phys.*, 126, 74506, doi: 10.1063/1.2463773.

Zhang, X., Li, C., Xu, F. and Zhang, J., et al. (2023): Sound Velocity Anisotropy and Single-Crystal Elastic Moduli of MgO to 43 GPa. *J. Geophys. Res.: Solid Earth*, 128, doi: 10.1029/2022JB026311.

Zhu, F., Liu, J., Lai, X. and Xiao, Y., et al. (2020): Synthesis, elasticity, and spin state of an intermediate $MgSiO_3$-$FeAlO_3$ bridgmanite: Implications for iron in Earth's lower mantle. *J. Geophys. Res.: Solid Earth*, 125, doi: 10.1029/2020JB019964.

Zhu, Q., Oganov, A.R. and Lyakhov, A.O. (2013): Novel stable compounds in the Mg-O system under high pressure. *PCCP*, 15, 7696–7700, doi: 10.1039/C3CP50678A.

Appendix A Supplementary materials Chapter 2

Appendix Table A 1 Reflectivity of the diamond-MgO interface ($R_{dia\text{-}smp}$) measured in this work and the resulting refractive index of MgO inferred using the Fresnel equation for perpendicularly incident light under the assumption of n_{dia} = 2.418. The values in parentheses are the estimated relative uncertainties on the parameters. The symbols CP and DP indicate compression and decompression path, respectively.

Run # Culet-size Pressure path	Pressure [GPa] (~±5 %)	$R_{dia\text{-}smp}$ (~±5 %)	Refractive Index, n_{MgO} (under the assumption of n_{dia} = 2.418) (~±1 %)
1 100µm (CP)	26.6	0.02761	1.729
1 100µm (CP)	26.6	0.02936	1.711
1 100µm (CP)	28.7	0.02819	1.723
1 100µm (CP)	43.8	0.03043	1.700
1 100 µm (CP)	44.2	0.02807	1.724
1 100 µm (CP)	55.3	0.02942	1.710
1 100 µm (CP)	56.3	0.02952	1.709
1 100 µm (CP)	68	0.03089	1.695
1 100 µm (CP)	68	0.03292	1.675
1 100 µm (CP)	85.4	0.0315	1.689
1 100 µm (CP)	87	0.03124	1.692
1 100 µm (CP)	103.6	0.03114	1.693
1 100 µm (CP)	103.6	0.03151	1.689
1 100 µm (CP)	116	0.03047	1.699
1 100 µm (CP)	116	0.0313	1.691
1 100 µm (CP)	124	0.02974	1.707
1 100 µm (CP)	124	0.0309	1.695
1 100 µm (CP)	139	0.03045	1.700
1 100 µm (CP)	139	0.03121	1.692
--	--	--	--
1 100 µm (DC)	99	0.03102	1.694
1 100 µm (DC)	60	0.02939	1.710
1 100 µm (DC)	37.3	0.02821	1.723
--	--	--	--
2 400 µm (CP)	21.8	0.02947	1.709
2 400 µm (CP)	32.5	0.03063	1.698
2 400 µm (CP)	36	0.03018	1.702
--	--	--	--
2 400 µm (DC)	36	0.0307	1.697
2 400 µm (DC)	36	0.0334	1.671
2 400 µm (DC)	30	0.02957	1.708
2 400 µm (DC)	30	0.03093	1.710
--	--	--	--
3 100 µm (CP)	25.1	0.0269	1.734
3 100 µm (CP)	34.8	0.02761	1.727
3 100 µm (CP)	42.3	0.02707	1.729
3 100 µm (CP)	49.5	0.0289	1.713
3 100 µm (CP)	57.9	0.02867	1.715

Run # Culet-size Pressure path	Pressure [GPa] (~±5 %)	$R_{dia\text{-}smp}$ (~±5 %)	Refractive Index, n_{MgO} (under the assumption of n_{dia} = 2.418) (~±1 %)
3 100 μm (CP)	63.2	0.02821	1.720
3 100 μm (CP)	75.1	0.02755	1.727
3 100 μm (CP)	87.3	0.02875	1.715
3 100 μm (CP)	95.9	0.02844	1.718
3 100 μm (CP)	103.7	0.02921	1.710
3 100 μm (CP)	108.5	0.02957	1.706
--	--	--	--
4 100 μm (CP)	24.89	0.02833	1.719
4 100 μm (CP)	34.5	0.02881	1.714
4 100 μm (CP)	47.1	0.02858	1.716
4 100 μm (CP)	56.5	0.0295	1.707
4 100 μm (CP)	65.2	0.03058	1.696
4 100 μm (CP)	76.5	0.02892	1.713
4 100 μm (CP)	84.3	0.03049	1.697
4 100 μm (CP)	94.4	0.02843	1.718
4 100 μm (CP)	103.5	0.02956	1.706

Appendix B Supplementary materials Chapter 3

Appendix B-1 Reflectivity measurements

As illustrated in **Figure 3-1** (main text), we measure reflections from several different interfaces as well as the intensity of light passing through the diamond anvil cell (DAC) to obtain the quantities that are necessary to solve Eq. 3.1 to 3.3 (main text, chapter 3.2.2). The initial probe intensity in air (I_{air}) was obtained as the amount of light reflected from a reference mirror with 99% reflectivity (I_{mirror}):

$$I_{air} = I_{mirror} / 0.99$$

Measuring the intensity of light reflected from the diamond-air interface we obtain its reflectivity:

$$R_{dia-air} = \frac{I_{dia-air}}{I_{air}}$$

Then, $I_0 = I_{air}(1 - R_{dia-air})$, $I_1 = I_0 R_{dia-smp}$, and $I_2 = I_0 \cdot \left(1 - R_{dia-smp}\right)^2 T^2 R_{dia-smp}$, where $R_{dia\text{-}smp}$ is the reflectivity of the diamond-sample interface and T is the sample transmission. Because samples in DACs are thin (~10 μm), the measured intensity of light reflected from the sample ($I_{dia\text{-}smp}$) always contains contributions from the upstream and downstream diamond-sample interfaces. Coming the above we can write:

$$\frac{I_1 + I_2}{I_0} = R_{dia-smp} + T^2({R_{dia-smp}}^3 - 2{R_{dia-smp}}^2 + R_{dia-smp})$$

Higher order reflections from the diamond-sample interface are not considered in the analysis because their contribution to the measured intensity ratio is negligible [1]. Finally, sample transmission is expressed as:

$$\frac{I_T}{I_{noDAC}} = T({R_{dia-smp}}^2 - 2R_{dia-smp} + 1)(1 - R_{dia-air})^2 ,$$

where I_T and I_{noDAC} are measured in transmission as graphically defined in **Figure 3-1**.

Appendix B-2 Diamond-ferropericlase interface reflectivity values

As discussed in the main text and in Schifferle et al. [2], we assumed a pressure independent refractive index of diamond. If in the future more precise estimations of the high-pressure index of diamond become available, data provided in **Appendix Table B 1** allows to recalculate the refractive index of ferropericlase as well as its absorption coefficient.

Appendix Table B 1 Diamond-sample interface reflectivity ($R_{dia\text{-}smp}$), sample refractive index at λ = 600 nm (n_{smp}), sample transmission (T, not normalized for sample thickness) and apparent thickness (OP, i.e., optical path; real thickness = OP/n_{smp}) as measured in this work, relying on the Fresnel equation for perpendicularly incident light for the assumption n_{dia} = 2.418 and pressure independence of n_{dia}. The values in parentheses are the estimated relative uncertainties on the parameters. Abbreviations: CP = compression, DC = decompression.

Sample	Run#, culet size, pressure path	Pressure [GPa] (±5%)	$R_{dia\text{-}smp}$ (±5%)	n_{smp} (for n_{dia} = constant = 2.418) (±1%)	T (±3%)	OP [μm] (err. <1%)
Fp13	100_1, CP	19.8	-	-	0.526	17.967
		20.9	-	-	0.526	17.911
		24.6	-	-	0.469	17.796
		29.2	-	-	0.402	17.412
		33.9	0.02071	1.810	0.356	17.134
		42.9	0.01975	1.822	0.279	16.491
		48.6	0.01941	1.827	0.229	16.122
		52.8	0.01902	1.832	0.197	15.685
		56.6	0.01944	1.826	0.194	15.092
		63.8	0.01812	1.844	0.217	14.463
		67.2	0.01917	1.830	0.237	13.990
		68.3	0.01918	1.830	0.250	13.849
		70.5	0.01701	1.860	0.268	13.641
		81.5	0.01922	1.829	0.334	13.220
		92.2	0.01871	1.836	0.383	12.861
		96.9	0.0178	1.849	0.376	12.664
		103.5	0.01748	1.853	0.399	12.516
		106.2	0.01862	1.837	0.391	12.539
		111.8	0.01851	1.839	0.406	12.443
		119	0.0184	1.840	0.405	12.342
		129.5	0.01854	1.838	0.415	12.285
		138.4	0.01857	1.838	0.401	12.231
Fp13	100_1, DC	100.4	0.01898	1.832	0.407	12.422
		84.7	0.01946	1.826	0.426	11.906
		75.1	0.01953	1.825	0.403	11.556
		68.6	0.02095	1.807	0.368	11.171
		57	0.02063	1.811	0.344	10.802
		38.6	0.02089	1.807	0.438	9.775
		25.3	-	-	0.569	9.225
		16	-	-	0.647	8.950
		9.9	-	-	0.698	8.921
		7.8	-	-	0.729	8.984
Fp13	100_2, CP	18.7	-	-	0.518	18.676
		26.3	-	-	0.383	18.161
Fp13	100_3, CP	16.9	-	-	0.480	21.537
		19.8		-	0.445	21.216
		23	-	-	0.399	20.898
		28.1	-	-	0.346	19.985
		35	0.02034	1.814	0.264	18.679
		38.2	0.02025	1.816	0.237	18.136
		43.6	0.0201	1.817	0.221	16.789
		50.3	0.01992	1.820	0.195	15.769
		54.9	0.0198	1.821	0.183	14.999
		62.1	0.01961	1.824	0.205	14.267
		69.3	0.01942	1.827	0.258	13.640

Sample	Run#, culet size, pres-sure path	Pressure [GPa] (±5%)	$R_{dia\text{-}smp}$ (±5%)	n_{smp} (for n_{dia} = constant = 2.418) (±1%)	T (±3%)	OP [µm] (err. <1%)
		76.2	0.01923	1.829	0.307	13.276
		82.8	0.01906	1.831	0.341	12.887
		86.9	0.01895	1.833	0.366	12.868
		89.7	0.01888	1.834	0.385	12.751
		100.3	0.01861	1.838	0.391	12.417
		109.1	0.01838	1.841	0.403	12.601
Fp13	300_1, CP	34.8	0.01984	1.821	0.064	37.384
Fp24	100_1, CP	24.8	0.01864	1.837	0	-
		31.1	0.01816	1.844	0	-
		40.8	0.01777	1.849	0	-
		48.9	0.01766	1.851	0	-
		58.4	0.01721	1.857	0	-
		61.5	0.01716	1.858	0	-
		66.6	0.01756	1.852	0	-
		73.9	0.01752	1.853	0	-
		88.6	0.01716	1.858	0	-
		99.5	0.01697	1.861	0	-
		105	0.01651	1.867	0	-
Fp24	100_1, DC	94.1	0.01682	1.863	0	-
		77.7	0.0172	1.857	0	-
		65.7	0.01704	1.860	0	-
		55.2	0.01644	1.868	0	-
		50.7	0.01665	1.865	0	-
		45.4	0.01689	1.862	0	-
		38.8	0.01725	1.857	0	-
		31.6	0.01757	1.852	0	-
		28.2	0.01758	1.852	0	-
		21.9	0.01744	1.854	0.005	10.218
		19.1	0.0178	1.849	0.014	10.544
		14.3	0.01783	1.848	0.027	10.561
		11.04	0.01766	1.851	0.039	10.478
		8.7	0.01777	1.849	0.053	10.442
		5.5	0.01877	1.835	0.075	10.416

Appendix B-3 Compositional dependence of ferropericlase refractive index

Ambient pressure measurements of Henning et al. [3] allow an estimation of the refractive index n(600 nm) of our Fp13 and Fp24 samples. A 2nd order polynomial fit to their data (lowest reported Fe content therein, $(Mg_{0.60}Fe_{0.40})O$) yields $n(x_{Fe}) = 4.675 \cdot 10^{-5}(\pm 9.444 \cdot 10^{-5}) \cdot {x_{Fe}}^2 + 0.0024\ (\pm 0.0133) \cdot x_{Fe} + 1.751\ (\pm 0.428)$ at 600 nm. As shown in **Appendix Figure B 1** (dotted line), our experimental data fit a 2nd order polynomial trend well. A revised fit of the compositional dependence of the refractive index to the iron content is shown by the solid trendline in **Appendix Figure B 1**: $n(X_{Fe}) = 4.286{\cdot}10^{-5}(\pm 2.144{\cdot}10^{-5}){\cdot}{X_{Fe}}^2 + 0.003(\pm 0.002){\cdot}X_{Fe} + 1.739(\pm 0.047)$.

While there are still unanswered questions on the low-pressure behavior of $n(600\ nm)$, our high-pressure data is suitable for first in-situ thickness measurements and the calculation of absorption coefficients. To reduce the influence of experimental uncertainties, for the calculation of the absorption coefficient, we derive a near-linear relationship of the refractive index n(600 nm) of ferropericlase with pressure. For Fp13 we find $n_{Fp13} = 3.535 \cdot 10^{-4}(\pm 7.022 \cdot 10^{-5}) \cdot P + 1.802(\pm 0.006)$ and $n_{Fp24} = 2.042 \cdot 10^{-4}(\pm 3.920 \cdot 10^{-5}) \cdot P + 1.844(\pm 0.002)$ (*P* is expressed in GPa; both fits including only data where *P* > 30 GPa).

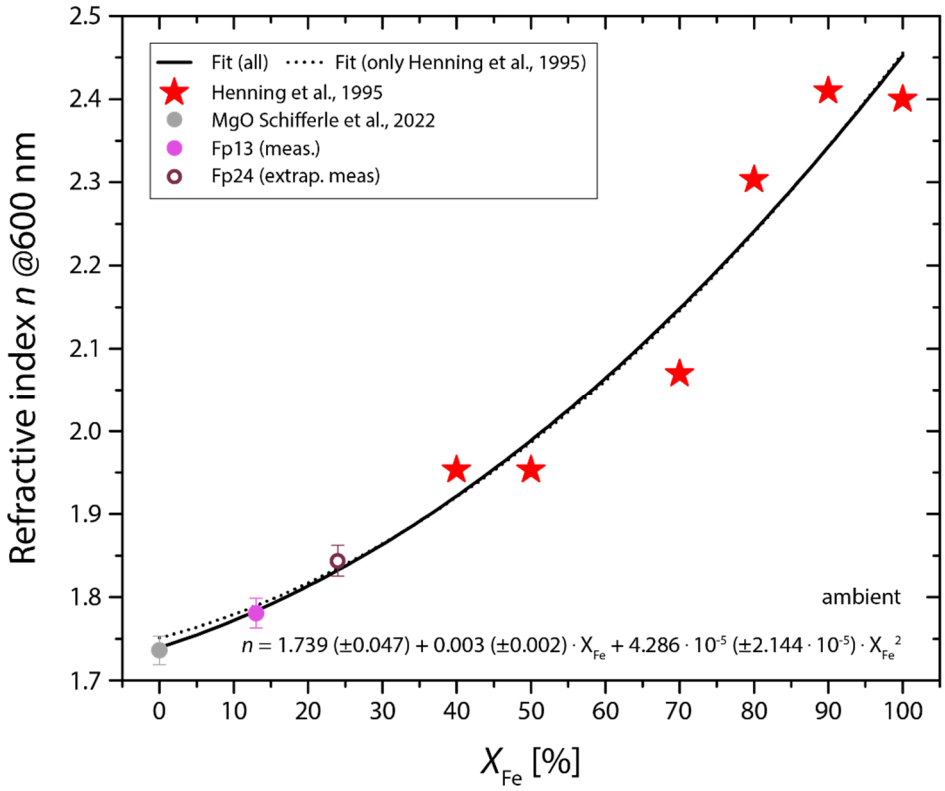

Appendix Figure B 1 Dependence of the ambient pressure refractive index on the iron content, based on this work (Fp13, Fp24), data of Henning et al. [3] ((Mg,Fe)O) and Schifferle et al. [2] (MgO). Solid trendline and equation represent all datasets shown, dotted line uses only data reported by Henning et al. [3].

Appendix B-4 High-pressure sample geometry and absorption coefficient

Our setup for refractive index measurements is not designed for broad-band spectral measurements (max. ~400-900 nm). Those, however, are necessary for the use in radiative conductivity calculations (e.g. Goncharov et al. [4]) Therefore, we used our α(600 nm) for Fp13 (main text, **Figure 3-3**), to derive a wide-range absorption coefficient from previously published absorbance data of Schifferle & Lobanov [5] (**Appendix Figure B 3**, **A**), which was performed on a piece of the exact same Fp13 crystal. This was done by multiplying the absorbance data of Schifferle & Lobanov [5] by a scalar, derived as $\frac{\alpha(600\ nm)}{A(600\ nm)}$. In the mixed-spin region, a reduction of the absorption coefficient in the range λ < 600 nm is observed. Towards the full low-spin state, the sample's UV-transparency is highly increased. The wavelength-dependent absorption

coefficient (α(λ)) is directly related to the imaginary part of the refractive index (ϰ): $\kappa = (\lambda \cdot \alpha(\lambda))/(4 \cdot \pi)$. Hence, the observed trends in ϰ are similar as for α (**Appendix Figure B 3**, **B**). Especially for λ < 600 nm, ϰ in the full-low spin state is vastly different from high-spin or mixed-spin. High ϰ for λ > 1000 nm observed for 81 and 105 GPa is probably related to instrumental errors for these two pressure points.

By analyzing the fringe pattern from the center and periphery of the sample, we constrain the thinning of the sample area on compression and decompression for Fp13 100 run 3 to a maximum pressure of ~109 GPa (**Appendix Figure B 2**). The observed thinning is far more pronounced than the isotropic compression/expansion, where $\frac{d}{d_0} = \left(\frac{V}{V_0}\right)^{1/3}$, with V and V_0 as the high-pressure and 1 atm unit cell volume and d and d_0 the according thicknesses, from the EoS would suggest [6–8] (i.e., samples are up to 50% thinner on compression than expected from the EOS). See also Lobanov & Geballe [9] for a thorough discussion. For the calculation of our thickness, we used the linear pressure dependence of the refractive index in Fp13. We find a decreasing thickness of the sample down to ~90 GPa. It is noted that the relative difference of thickness in center and periphery increases from 0.7% at ~17 GPa to 3.6% at ~109 GPa, which we assign to the diamond cupping at high pressure [10; 11]. Based on a 2nd order polynomial fit (dashed line in **Appendix Figure B 2**) we estimate sample thickness at 1 atm of ~14.54 μm. The 1 atm (theoretical) thickness is then used to calculate relative thinning of the sample. From 1 atm to ~109 GPa we find a thinning by ~50%.

On decompression, we observe further thinning of the sample, down to ~65% (from 1 atm). This is accompanied by substantial radial growth of the sample area. At P < 10 GPa we observe an increase of sample thickness, which was also confirmed by a FIB cross-section through the center of the decompressed sample (main Text, **Figure 3-1 D**). Similar compression/decompression thinning has been observed previously [9; 12; 13].

The decrease of diamond culets' cupping in decompression leads to large radial strain in the sample and a push-down effect at the culet center which causes the reduction of sample thickness (**Appendix Figure B 4**, **A**). Such a process is consistent with the decreasing in edge-center thickness difference (**Appendix Figure B 2**). The irregular outline of the sample (**Figure 3-1 D**, main text) is likely a product of heterogeneous radial strain gradients (**Appendix Figure B 4**, **B**). As visible in the cross-section, displacement is less dominant at the interface to the diamond culet, creating an overlap of gasket material over the sample. Please note, this is only a decompression feature. Walls of the DAC sample chamber stay visibly vertical on compression, as is also indicated by sharp edges of x-ray transmission data of previous studies [14–16]. We propose, on decompression high friction at the diamond-sample and at the diamond-gasket interfaces results in a non-uniform relative displacement field as illustrated in **Appendix Figure B 4**, **B**. Thickness increase observed at low pressure could reflect the final elastic rebound of the sample.

Although our transmission measurements on Fp24 are limited, **Figure 3-3** (main text) shows that the absorption coefficient of ferropericlase is strongly non-linear and dominated by the iron content (factor of ~13 difference at 10 GPa between Fp13 and Fp24). Similar conclusions were also drawn by Deng et al. [17]. Unfortunately, the absorption mechanisms caused by the iron-iron interactions are difficult for DFT to

consider. Hence, experiments are inevitable to assess the composition, pressure, and wavelength-dependence of the absorption coefficient.

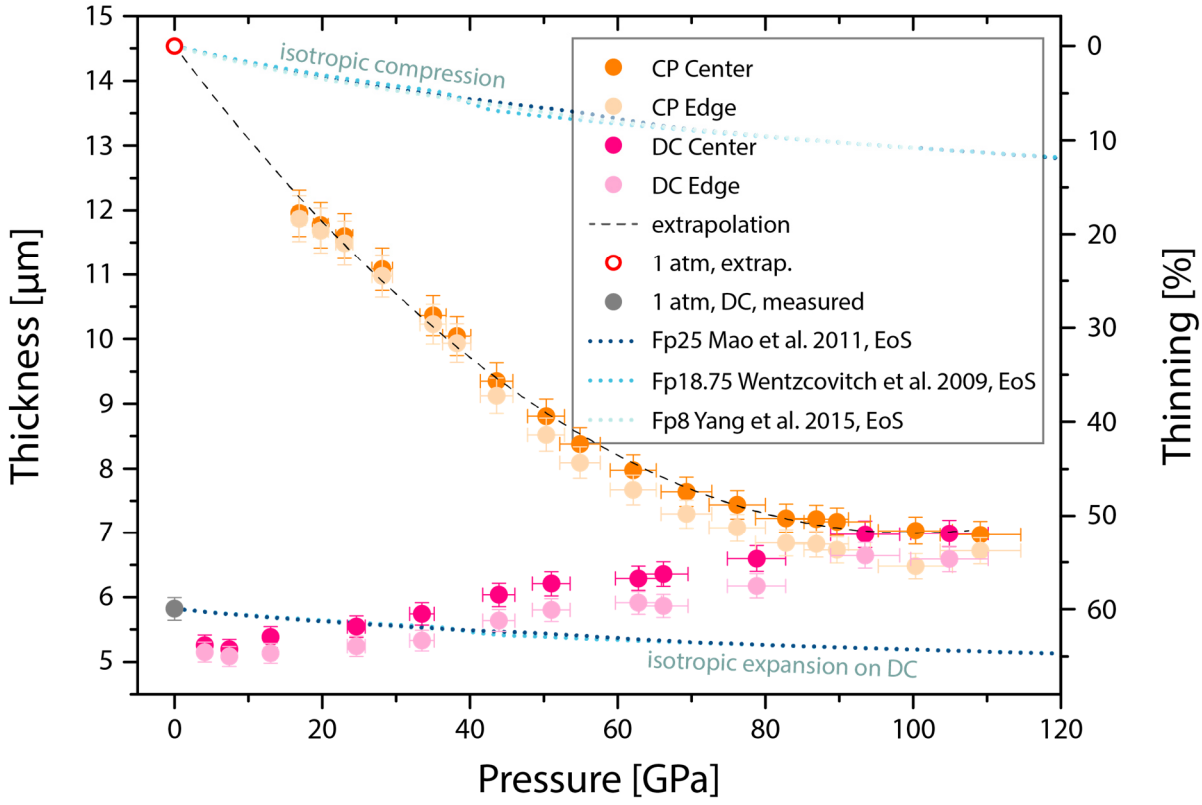

Appendix Figure B 2 Sample thickness on compression and decompression of Fp13 100 run 3. Dashed line is a 2nd order polynomial fit to the compression data and is used to extrapolate thickness at 1 atm (empty red circle). Grey circle marks the measured thickness of the decompressed sample center from a FIB cross section. CP = compression, DC = decompression. Dotted lines show a theoretical isotropic compression/expansion based on the isothermal equation of state (EoS) for Fp25 [6], Fp18.75 [7] and Fp8 [8].

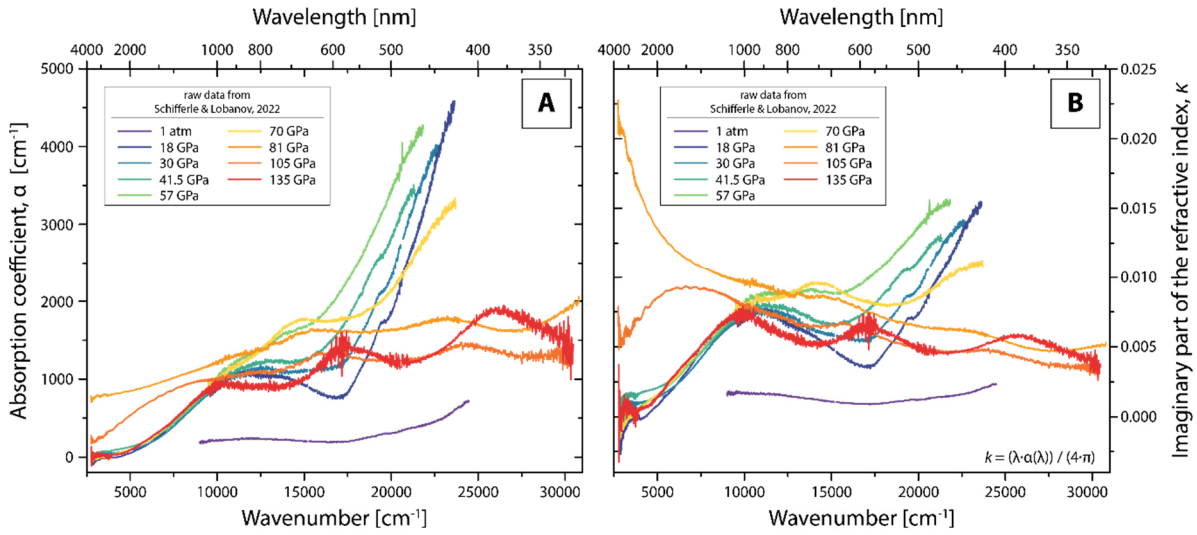

Appendix Figure B 3 Absorption coefficient (α) (**A**) and imaginary part of the refractive index (ϰ) for Fp13 (**B**), based on absorption data of Schifferle & Lobanov [5].

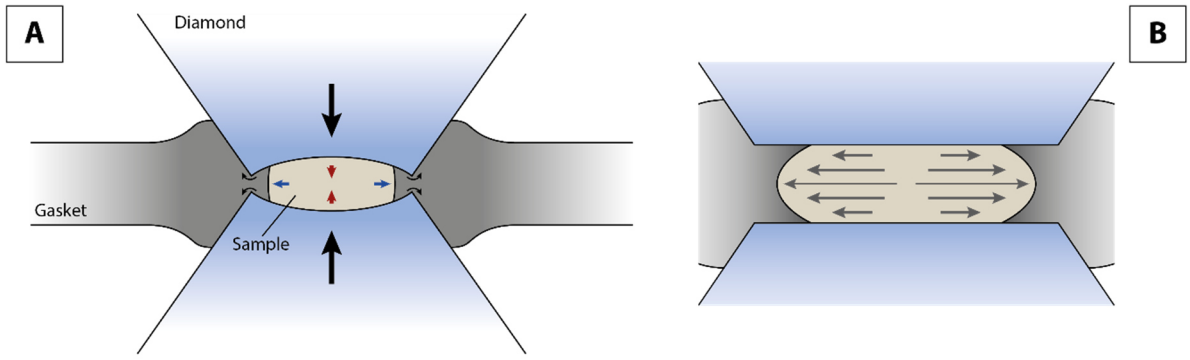

Appendix Figure B 4 A: Geometry change of cupped diamonds and sample on decompression. Black arrows represent diamond movement, blue arrows indicate enlargement for the sample, red arrows shrinking of the sample. **B**: Schematic displacement field of the sample..

Appendix B-5 References

[1] Lobanov, S.S.; Speziale, S.; Winkler, B.; Milman, V. *et al.* (2022): Electronic, structural, and mechanical properties of SiO_2 glass at high pressure inferred from its refractive index. *Phys. Rev. Lett., 128 (7)*, 77403, doi: 10.1103/PhysRevLett.128.077403.

[2] Schifferle, L.; Speziale, S.; Lobanov, S.S. (2022): High-pressure evolution of the refractive index of MgO up to 140 GPa. *J. Appl. Phys., 132 (12)*, 125903, doi: 10.1063/5.0106626.

[3] (1995):Henning, T.; Begemann, B.; Mutschke, H.; Dorschner, J. Optical properties of oxide dust grains. *Astron. Astrophys. Suppl. Ser., 112*, 143–149.

[4] Goncharov, A.F.; Beck, P.; Struzhkin, V.V.; Haugen, B.D.; Jacobsen, S.D. (2009): Thermal conductivity of lower-mantle minerals. *Phys. Earth Planet. Inter., 174 (1-4)*, 24–32, doi: 10.1016/j.pepi.2008.07.033.

[5] Schifferle, L. & Lobanov, S.S. (2022): Evolution of chemical bonding and spin-pairing energy in ferropericlase across its spin transition. *ACS Earth Space Chem., 6 (3)*, 788–799, doi: 10.1021/acsearthspacechem.2c00014.

[6] Mao, Z.; Lin, J.-F.; Liu, J.; Prakapenka, V.B. (2011): Thermal equation of state of lower-mantle ferropericlase across the spin crossover. *Geophys. Res. Lett., 38 (23)*, L23308, doi: 10.1029/2011GL049915.

[7] Wentzcovitch, R.M.; Justo, J.F.; Wu, Z.; Da Silva, C.R. S. *et al.* (2009): Anomalous compressibility of ferropericlase throughout the iron spin cross-over. *Proc. Natl. Acad. Sci. U.S.A., 106 (21)*, 8447–8452, doi: 10.1073/pnas.0812150106.

[8] Yang, J.; Tong, X.; Lin, J.-F.; Okuchi, T.; Tomioka, N. (2015): Elasticity of ferropericlase across the spin crossover in the Earth's lower mantle. *Sci. Rep., 5*, 17188, doi: 10.1038/srep17188.

[9] Lobanov, S.S. & Geballe, Z.M. (2022): Non-isotropic contraction and expansion of samples in diamond anvil cells. *Geophys. Res. Lett., 49 (19)*, e2022GL100379, doi: 10.1029/2022GL100379.

[10] Li, B.; Ji, C.; Yang, W.; Wang, J. *et al.* (2018): Diamond anvil cell behavior up to 4 Mbar. *Proc. Natl. Acad. Sci. U.S.A., 115 (8)*, 1713–1717, doi: 10.1073/pnas.1721425115.

[11] Mao, H.-K. & Mao, W.L. (2007): Theory and practice – diamond-anvil cells and probes for high P–T mineral physics studies. In: Price & Schubert (Eds.): Treatise on Geophysics. Volume 2: Mineral Physics 2, 231–267.

[12] Dewaele, A.; Eggert, J.H.; Loubeyre, P.; Le Toullec, R. (2003): Measurement of refractive index and equation of state in dense He, H_2, H_2O, and Ne under high pressure in a diamond anvil cell. *Phys. Rev. B Condens. Matter, 67 (9)*, doi: 10.1103/PhysRevB.67.094112.

[13] Kalkan, B.; Sonneville, C.; Martinet, C.; Champagnon, B. *et al.* (2012): Hysteretically reversible phase transition in a molecular glass. *J. Chem. Phys., 137 (22)*, 224503, doi: 10.1063/1.4769794.

[14] Dewaele, A.; Loubeyre, P.; Occelli, F.; Marie, O.; Mezouar, M. (2018): Toroidal diamond anvil cell for detailed measurements under extreme static pressures. *Nat. Commun., 9 (1)*, 2913, doi: 10.1038/s41467-018-05294-2.

[15] Dong, W.; Glazyrin, K.; Khandarkhaeva, S.; Fedotenko, T. *et al.* (2021): $Fe_{0.79}Si_{0.07}B_{0.14}$ metallic glass gaskets for high-pressure research beyond 1 Mbar.

[16] Lamichhane, A.; Kumar, R.; Ahart, M.; Salke, N.P. *et al.* (2021): X-ray diffraction and equation of state of the C-S-H room-temperature superconductor. *J. Chem. Phys., 155 (11)*, 114703, doi: 10.1063/5.0064750.

[17] Deng, J.; Du, Z.; Benedetti, L.R.; Lee, K.K. M. (2017): The influence of wavelength-dependent absorption and temperature gradients on temperature determination in laser-heated diamond-anvil cells. *J. Appl. Phys., 121 (2)*, 25901, doi: 10.1063/1.4973344.